論文 / 著書情報
Article / Book Information

題目(和文)	機能性素子の開発に向けたレーザー照射による分相ホウケイ酸塩ガラスおよびシリカガラスのナノーマイクロ構造制御
Title(English)	Nano micrometer size structural modification through laser absorption in borosilicate and silica glasses for functional device fabrication
著者(和文)	富田夏奈
Author(English)	Kana Tomita
出典(和文)	学位:博士(学術), 学位授与機関:東京工業大学, 報告番号:甲第12472号, 授与年月日:2023年3月26日, 学位の種別:課程博士, 審査員:矢野 哲司,松下 伸広,須佐 匡裕,林 幸,岸 哲生,比田井 洋史
Citation(English)	Degree:Doctor (Academic), Conferring organization: Tokyo Institute of Technology, Report number:甲第12472号, Conferred date:2023/3/26, Degree Type:Course doctor, Examiner:,,,,,
学位種別(和文)	博士論文
Type(English)	Doctoral Thesis

Nano-micrometer size structural modification through laser absorption in borosilicate and silica glasses for functional device fabrication

February 10, 2023
Final version

School of Materials and Chemical Technology
Department of Materials Science and Engineering

Kana Tomita

機能性素子の開発に向けたレーザー照射による分相ホウケイ酸塩ガラスおよびシリカガラスのナノーマイクロ構造制御

Nano-micrometer size structural modification through laser absorption in borosilicate and silica glasses for functional device fabrication

Contents

1 Introduction 6
1.1 Glass material 6
1.1.1 Glass network 6
1.1.2 Silica glass synthesis 7
1.1.3 Porous silica glass fabrication through phase separation in borosilicate glass 7
1.2 Laser processing on glass 9
1.2.1 High energy density generation by laser 9
1.2.2 The photon absorptions in glass 11
1.3 Glass device fabrication with laser processing 14
1.3.1 Nanoscale structural modification of glass by CW laser partial heating 14
1.3.2 3D micromachining on silica glass by combination of femtosecond laser irradiation and wet etching 16
1.4 Focus of this study 18
1.5 Objective 18
2 Space selective porous/non-porous design on silicate glass substrate by CW laser 19
2.1 Introduction 19
2.2 Experimental 21
2.2.1 Synthesis 21
2.2.2 Optical absorption spectroscopy 21
2.2.3 Thermal analysis 22
2.2.4 Laser scanning on glass plate 22
2.2.5 Post processing for porous structure formation 22
2.2.6 Evaluation of porous structure 23
2.3 Results 23
2.3.1 Optical absorption behavior at room temperature after fabrication 23
2.3.2 Thermal properties 24
2.3.3 Glass plate appearance after laser irradiation 26
2.3.4 Laser induced modification at glass surface 29
2.3.5 Laser induced modification inside the glass plate 33
2.4 Discussion 36
2.4.1 The selection of glass composition 36
2.4.2 Absorption behavior with different doped ions species 37

2.5 Summary 39
3 Evaluation on phase miscibility in borosilicate glass probed by Ni^{2+} ion 40
3.1 Introduction 40
3.2 Experimental 40
3.2.1 Sample synthesis 40
3.2.2 Room temperature measurements on water quenched glasses 41
3.2.3 High temperature in-situ XAFS measurement 41
3.3 Results 43
3.3.1 Phase immiscibility evaluation of water-quenched glass by SEM images 43
3.3.2 Optical absorption of water quenched glass after heat treatment 46
3.3.3 RT-XAFS spectra of water-quenched glasses 51
3.3.4 Ni-K edge XAFS measurement in borosilicate glass and melt 54
3.3.5 Ni-K edge XAFS measurement in laser irradiated NBS glass plate 60
3.4 Discussion 62
3.4.1 Homogeneity of phase separating NBS glass and Ni^{2+} environment 62
3.4.2 Ni^{2+} coordination analysis 62
3.4.3 Ni^{2+} as structural probe in phase separated glass 64
3.4.4 Thermal effect on Ni^{2+} ion local environment 65
3.5 Summary 68
4 Time resolved in-situ observation of dynamic transition behavior of phase miscibility during heat treatment 69
4.1 Introduction 69
4.2 Experimental 69
4.2.1 Sample preparation 69
4.2.2 High temperature in-situ SAXS measurement. 69
4.3 Results 72
4.3.1 Immiscibility of water-quenched glasses with varying compositions 72
4.3.2 Effect of Ni^{2+} and Cu^{2+} ion on temperature dependence of immiscibility change in NBS glass observed by high temperature in-situ SAXS measurement.. 74
4.3.3 Time-resolved observation of phase separation behavior during heating up to miscible temperature 78
4.3.4 Time-resolved observation of phase separation behavior during cooling down from miscible temperature 81
4.4 Discussion 84
4.4.1 Effect of additive transition metal ion on phase separation 84

4.4.2 Homogenization behavior during heating process of glass with various initial immiscibility 85
4.4.3 Phase separation development in cooling process from miscible melt 87
4.5 Summary 90
5 Computer simulation on spatial distribution of thermal history and phase separation in glass substrate by laser heating 91
5.1 Introduction 91
5.2 Theory 91
5.2.1 Heat transfer and laser absorption in a glass substrate 91
5.2.2 Radiation model in thin transparent media 93
5.3 Experimental 94
5.3.1 Apparent Laser absorbance measurement 94
5.3.2 Thermal history calculation by finite element method 94
5.4 Result 98
5.4.1 Apparent laser absorbance measurement 98
5.4.2 Temperature calculation in laser absorbing media 100
5.4.3 The thermal history distribution at porous/ non-porous boundary 105
5.5 Discussion 112
5.5.1 Validity consideration on material properties in calculation 112
5.5.2 Mechanism of porous/ non-porous clear boundary by laser irradiation 114
5.5.3 The dominance of heat generated by respective source 115
5.6 Summary 117
6 3D micro processing and microstructure control of silica glass by femtosecond laser irradiation 118
6.1 Introduction 118
6.1.1 Vibrational damping function on silica glass cantilever by Acoustic Black Hole structure 118
6.1.2 Theory of Acoustic Black Hole effect 119
6.2 Experimental 121
6.2.1 Cantilever fabrication 121
6.2.2 Vibration tests 122
6.2.3 Static properties observation of the cantilever after processing 122
6.3 Results 123
6.3.1 Glass cantilever fabrication 123
6.3.2 Vibration test on cantilever 124
6.3.3 Chemical properties of the surface after processing 127

6.4 Discussion..... 130
6.4.1 Structural modification distribution in glass after fs laser exposure..... 130
6.4.2 Modification effect on dynamic behavior of glass cantilever 130
6.4.3 Possibility of femtosecond laser processing on glass..... 133
6.5 Summary..... 134
7 Nano-micrometer size structural control by laser irradiation on glass 135
7.1 Possibility of functional designing in monolithic glass substrate 135
7.2 Spatial distribution of laser effect in surroundings of focal spot..... 137
7.3 The effect of thermal history on glass structure 137
8 Conclusion 140
9 Reference 142
Acknowledgements 158

1 Introduction

1.1 Glass material

1.1.1 Glass network

Glass is a solid obtained by supercooling a melt without crystallization. By rapid quenching a liquid, glass keeps random structure like melt. In addition, glass shows specific thermal characteristic called “glass transition”: When the solid glass is heated from room temperature, second derivative thermodynamic properties suddenly change at glass transition temperature Tg. The glass transition temperature is not fixed for each glass composition, contrary to first-order phase transition temperature in equilibrium state. It depends on how the configuration of glass network structure is frozen, so Tg varies with melting and cooling condition. The variation of Tg can amount to hundreds of degrees[1].

The oxide glass consists of 3-dimensional network formed by network former oxide (SiO_2, B_2O_3, P_2O_5, GeO_2, …) forming polyhedral or plane polygon surrounded by oxygen. Network modifier cations (Alkali, alkali earth, transition metals…) exist in between those polyhedral and change the connectivity of network. Glass network is extensive (continuous), but lacking periodicity (random). The number of oxygens bonded to the respective cations is typical for each atom, and such a connectivity and configuration (bonding angle/length) of those network strongly affects fundamental characteristics such as density[2], thermal expansion rate[3][4], thermal conductivity[5], electric conductivity[6], and so on.

Such a network structure strongly depends on composition, temperature[7][8], and pressure. The network connectivity of silicate glass is characterized by distribution of structural unit Q^n, where n is the number of bridging oxygen in SiO_4 tetrahedra ($n \leqq 4$). The distribution of Q^n shows the equilibrium $2Q^3 \leftrightarrow Q^2 + Q^4$, with equilibrium shifts toward right side as temperature increases [9][10]. On the other hand, borate glass also has temperature-dependent equilibrium $BO_4^- \rightarrow BO_3 + O_{NBO}^-$, where NBO represents non bridging oxygen. The equilibrium shift toward right hand side as temperature increases. In both silicate and borate oxide glasses, amount and kind of network modifier also affect glass properties by changing network connectivity besides temperature [11][12].

The glass structure at room temperature strongly depends on thermal history before the structural modification stop below Tg [13]. When the glass melt is cooled down without crystallization, firstly glass is supercooled under melting temperature. The

supercooled liquid has extremely high viscosity, and it will take very long time to approach equilibrium, but still the glass network gradually keeps moving to follow equilibrium, where this phenomenon is so-called relaxation. In order to control the glass properties, the glass structure at high temperature is important as well as how the structural change proceeds under transient temperature.

1.1.2 Silica glass synthesis

The oxide glass has several characteristics which cannot be achieved by other materials. Its high optical transparency with high chemical and thermal resistance enables various applications. Silica glass has outstanding characteristics even compared to other oxide glass systems. Silica glass with high purity over 99.5% or more has excessive high thermal and chemical resistance, wide optical window and high purity. On the other hand of high stability, fabrication and modification of silica glass require specific methods compared to other oxide glasses containing additive components to lower its melting temperature. Usually, silica glass is fabricated by melting quartz and silica containing minerals in an electric furnace or oxyhydrogen flame or deposited from $SiCl_4$ and oxygen gas in plasma generated by radio frequency heating. Such high-purity silica is used in optical components, semiconductor devices, and sample cells used in spectroscopy.

In some practical usages, purity of silica glass is not required to fulfill 99% such as experimental glassware, heat-resistant glass. Silica glass with purity around 96% can easily be fabricated by spontaneous phase separation of borosilicate glass into silica-rich phase and alkali borate-rich phase. There are two different types of phase separation: spinodal (interconnected) and binodal (droplet). In the case of spinodal phase separation, phases are interconnected so borate-rich phase can easily be washed away by acid leaching through inside of the bulk glass. After acid leaching, nano porous silica glass can be obtained. By heating such a glass above 800°C, the porous structure is lost by sintering effect and bulk silica glass with high purity can be produced[14]. Contrary, binodal phase consists of precipitated droplet in continuous base, and the droplet consists of minor component of either silica-rich or borate-rich composition. When silica is main component in borosilicate glass, borate-rich droplet precipitate in silica rich-continuous phase. So the phase separated glass shows similar properties (viscosity[15], refractive index[16], chemical durability[17]) to those of silica glass.

1.1.3 Porous silica glass fabrication through phase separation in borosilicate glass

Phase separation is the nature of the glasses with certain composition in metastable

condition [18]. Low alkali containing borosilicate glass like Na_2O-B_2O_3-SiO_2 glass separates into two different interconnected glass phases in nano scale under heat treatment; SiO_2-rich phase and B_2O_3-rich phase. Acid leaching after heat treatment washes away only soluble B2O3 rich phase, and nano porous structure consisting of 96 % SiO_2 is obtained [19][20]

Morphology after phase separation depends on its initial composition and heat treatment temperature [21][22]. The phase separation occurs in case there are two different metastable compositions when mixing two different components, as illustrated in Figure 1.1. When the free energy curve (dependent on T: temperature and x: composition ratio) at initial glass composition gives $\frac{\partial^2 \Delta G}{\partial x^2} < 0$, two phases show interconnected structure called "spinodal separation" driven by amplification of concentration fluctuation[23][24]. On the other hand, when $\frac{\partial^2 \Delta G}{\partial x^2} > 0$, glass would show one phase precipitated in droplet form in continuous another phase, so-called "binodal separation", which is driven by nucleation growth [25][22]. Actual phase development depends on both the thermodynamic driving force and the kinetics diffusion. Both of these factors are strongly dependent on temperature, with opposite tendency: at low-temperature, thermodynamic driving force is larger than at high temperature but the viscosity is too high to proceed phase separation. In this way the maximum rate of phase separation is expected to be found in middle temperature range[26]. Phase separation starts with chemical segregation together with emerging interface for phase formation, and phase development proceeds until it reaches asymptotic equilibrium[27][25]. The time dependence of phase development at respective temperatures had been investigated using various observation methods. The dominant diffusion factor in phase separation can be approximated from time dependence of specific surface area decay [27][28]. The time dependence of phase development had been observed either by quenching the heat-treated glass specimen, or directly measuring during heating. The former method enables us to use various measurement techniques such as refractive index[16], viscosity[29][30], Atomic Force Microscope (AFM) [25], Scanning Electron Microscope (SEM) [31], BET analysis on isothermal nitrogen adsorption measurement [27], and so on. For the latter, in-situ measurement during heating is available butlimited method such as light or Small-Angle X-ray Scattering measurement[28][32].

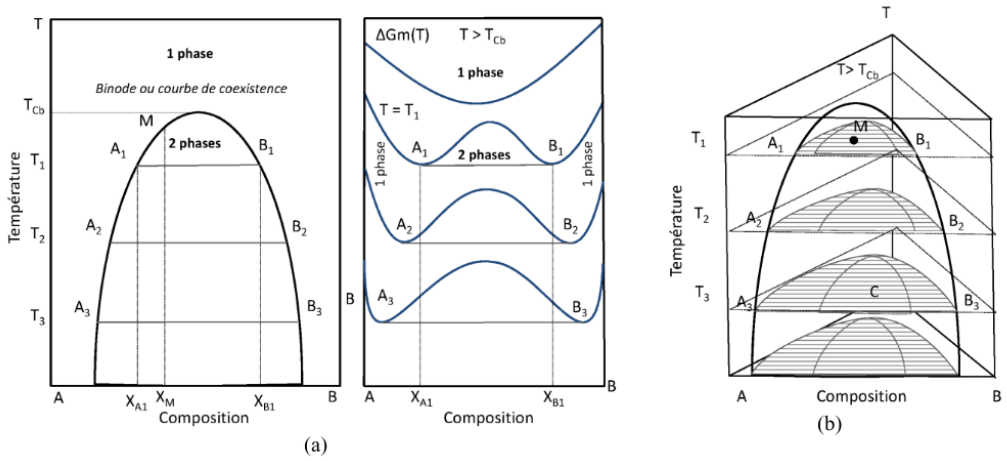

Figure 1.1 Composition and temperature dependence of phase separation in binary system. When the glass with certain composition is exposed under temperature located inside the illustrated dome in (a), glass shows immiscibility to give two different compositions A and B spotted on the dome line. In case of ternary system, it can approximated as binary phase separation by fixing one component which has small effect on phase separation behavior, indicated as "C" in (b) [33]

1.2 Laser processing on glass

1.2.1 High energy density generation by laser

The photon energy absorption in materials can affect their characteristics of absorbing material through physical and chemical reactions. Light, or electromagnetic waves conduct numbers of photons depending on their frequency. Laser is able to emit high energy density due to coherent properties: high directionality, spectral purity, and intensity.

Laser is the common technology used in various fields in society as lighting on stage, light source of projection, sensing and measurement. In material processing using laser enables designing of structure in high dimension. The important laser parameters to induce the changes in materials are wavelength, oscillation method, output power, exposure time, optical system to focus the light, and so on. There are numerous variations in exposure of laser lights, so one has to optimize the parameters based on objective material processing.

The choice of laser oscillation is the most effective to determine the types of induced phenomena in material. There are laser oscillation methods: continuous wave (CW) and

short pulse laser. The power density of short pulse laser can be 5 orders of magnitude higher than CW laser. With several hundred of 10^{-15} (femto) second pulse oscillation, the monochromatic light with several Giga-Watt energy density of peak value can be generated. Each oscillation method has its own distinctive characteristics, so they are used in different occasions depending on objective and requirement of laser processing.

CW laser requires simple optical system, consisting of incident laser light source, collimator, and objective lens. Scanning of CW-laser on material provides continuous modification lines in an irradiated material. Laser energy is deposited continuously heat to be accumulated at focal point with its diffusion to the surrounding. CW laser irradiation is suitable for heating process in large area. On the other hands, pulse laser is emitted in short period of time by inserting shutter, optical switch, or modulator in optical system. Compared to CW laser, pulsed laser provides highly densified energy as a flashlight. So, the modification spot in exposed material would form structural patterns depends on repetition rate and pulse duration. When the pulse duration becomes in femtosecond order, power density reaches high intensity enough to observe multiphoton absorption. In this time scale, the effect of thermal diffusion is negligibly small, and the temperature increase will occur in very limited space at focal point. Energy deposition with short pulse laser enables spot modification in high precision.

The laser processing on material had been developed since late 1960s, when the high-power CW-CO_2 laser and YAG laser started to be supplied in commercial. In the beginning, the laser oscillation was unstable, and the spot size was large, due to diffraction limit depending on wavelength of the laser. For improvement on precise processing, laser with shorter wavelength with high output power had been developed such as excimer laser which emits ultraviolet rays.

The use of laser in material processing had been developed in commercial use in the field of metalworking. Metals such as Ni, Cr and Al absorbs YAG laser (λ=1064 nm) efficiently and have good thermal conductivity[34]. The laser processing provides advantage in welding and drilling, which requires the heating of the material up to melting temperature and let the liquid melt to flow and remove from focal point. The heat affects the surrounding of laser irradiated surface. The heat conduction to surrounding space should be avoided, since phase transformation or crystallization might occur and affects the strength of the material. Phase transition on the metal surface by laser heating and cooling causes hardening of the metal plate.

Femtosecond pulse laser exposure causes various physical changes which can never be achieved by CW laser irradiation. The energy density is up to 10 TW/cm^2, which means that the photon flux has high electric field to remove the valence electron in atom.

The research on material processing started in early 1990s, using the stable material which cannot be modified by previous CW lasers, such as diamond, ceramics, and glass. Due to highly complexed alignment of optical system and its high cost, commercial use became popular in 2000s, after the further technological development for stable, low-cost laser emission. The versatile use of the femtosecond laser is expected to enhance quality of micro to nano processing of semiconductor, glass, optical components, and even protein analysis and medical applications.

By adapting laser processing suitable for the material properties, further functionalization of the material is possible. With advances in laser technology, the material processing using laser is still developing along. Attosecond laser, first demonstrated in 2001[35], is now being developed to supply stable, continuous output[36]. When attosecond laser exposure is applied on silica glass, the insulating-to-conducting state transition is reported to be found in. enhancing electron conductivity from $\sigma\alpha\text{-}SiO_2<10\text{-}18\ \Omega^{-1}m^{-1}$ up to $\sigma_{eff}\ (\omega L)\approx 5\ \Omega\text{-}1m^{-1}$, where ω is carrier angular frequency of the optical field) [37]. On the other hand, improvement of output power and the aperture size have been significantly enhanced in recent year. It is important to understand the phenomena and mechanism of structural modification in material, in order to discover a new value in material processing with new method[38].

1.2.2 The photon absorptions in glass

The glass is apparently transparent in visible light region, because it has the fundamental absorption edges in UV and IR regions, which reflect atomic bonding inside the glass.

Absorption of UV light is due to defect in Si-O bonding. The defect merely exists in silica glass after fabrication, but it increases when the glass is exposed under strong electromagnetic field such as lasers[39] or X-ray. The point defect absorbs light in near infrared to vacuum UV range, even some of the defects absorb visible light so called “color center”[40]. **Figure 1.2** shows the list of defects and its absorption energy, with corresponding laser with the wavelength in same region[41]. The absorption of UV light and X-rays in glass is serious problem for optical window of X-ray or neutron experiments set-ups [42].

As noted in the left side of **Figure 1.2**, excimer laser wavelength (KrF: 248 nm, ArF: 193 nm, F_2: 157 nm) matches the strong absorption bands due to several defects such as non-bridging oxygen (≡Si-O˙), divalent Si/ O vacancy (SiODCII), and peroxy radicals (≡Si-O-O˙). The excimer laser has highest spatial resolution, with its shortest laser wavelength in existing laser. Excimer lasers are used for photolithography, and silica

glass substrate is used as a mask of photoresist. For such a purpose, the defect in silica glass which may absorb the UV light must be eliminated [43].

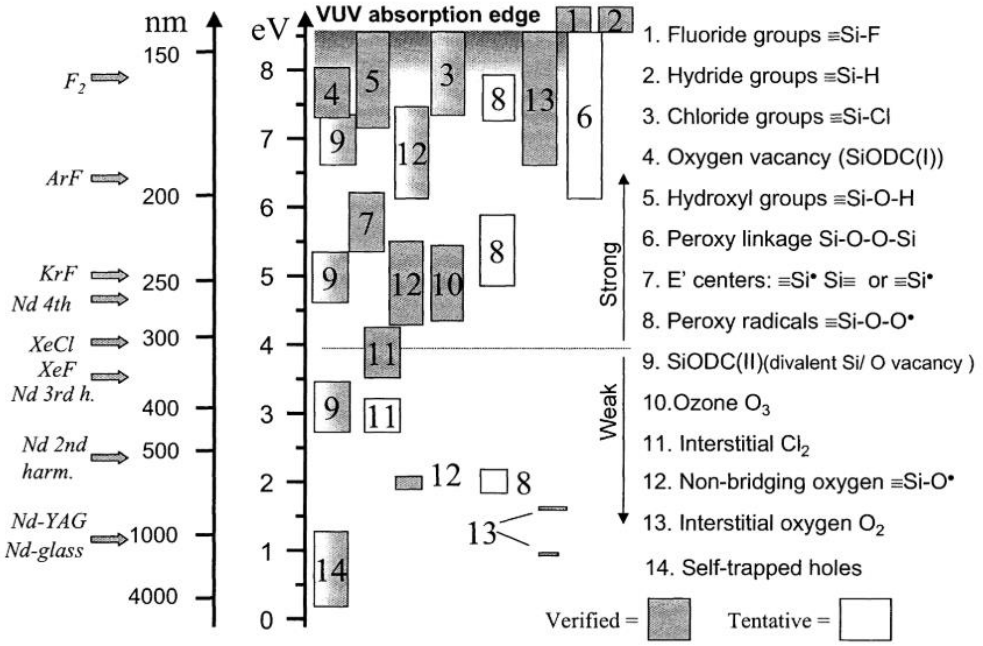

Figure 1.2 Energy dependence of emission from respective laser and absorption in silica defects [41]**.**

The absorption bands in IR region are mainly due to resonant vibration of Si-O bonding in various dynamic modes [44]. Those absorption behavior reflect bonding length, angle, and species of network formers, which are affected by temperature[2], pressure[45], and even water content inside the glass [46][47]. Changes in bonding is often directly correlated to macroscopic material properties such as density, Young's modulus, refractive index[48], and so on. The absorption band of CO_2 laser is located at λ=10.6 μm, where the Si-O-B bonding absorbs. SiO_2 glass have very weak absorption tail at λ=10.6 μm, though it absorbs CO_2 laser especially when the temperature increased. The shoulder of Si-O absorption band shift toward 12 μm [49]. Taking advantage of relatively large spot size and high output power, so CO_2 laser was used for surface modification in large area such as polishing and marking on silica glass[50][51].

In visible-near IR wavelength region, most of silicate glasses are colorless but doping of transition metal (TM) ions etc. induces color because they act as color center in glass. In detail, TM ion doped in a glass absorbs light due to d-d electric transitions in visible-

near infrared wavelength region[53]. The d-orbitals have strong interaction with ligand and emission probability is generally low, and non-radiative relaxation process is major in the ground state. Therefore, heat generation can be controlled by changing the amount of additive TM ion.

Laser is beneficial to excite TM ion using selected d-d transition by wavelength of light. Taking advantage of the local heat generation around laser focal point, phase transformation can be introduced in glass. For example, laser heating using doped TM ions in monolithic glass has been used to draw crystalline lines on glass [12][54][55]. In this way, we can expect partial heat treatment and modification of glass substrate by TM ion doping and laser irradiation. Comparison with CO_2 laser is shown in **Figure 1.3**.

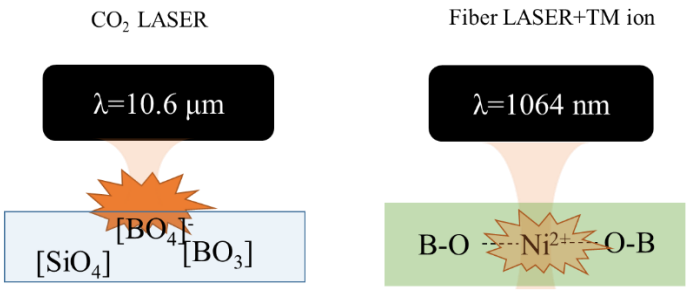

Figure 1.3 Schematic illustration of laser absorption behavior of glass. CO_2 laser is absorbed by Si-O and B-O bonding, which is most common component of the commercial glass. Most of the laser light is absorbed at the surface (left). Laser with NIR wavelength is mostly transmitted by silicate and borosilicate glass, but additive transition metal (TM) ion absorbs visible to NIR light by d-d transition.

Combination of the laser irradiation and absorption enables various physical and chemical modification in glass. When a photon is absorbed by specific elements or bonding in the glass, the absorbed energy mostly transferred to heat. The generated heat at laser focal point diffuses to surrounding volume and increase the temperature at larger area than laser spot size. These are the resonant absorption of light by elements in glass. Multiphoton absorption can be induced by laser irradiation to cause modification of glass. The probability of multiphoton absorption is very low at the photon density of CW laser. However, if a number of photons are given to the glass for a short period of time, multiphoton absorption occurs with high probability. In this case, the utilized photon does not have large $h\nu$ comparable to the transition of bandgap. The sum of the energies of the multiple photons satisfy the band gap energy.

Multiphoton absorption does not always require coherence and can be described by simple rate equations. As long as the population densities of the involved lower states of transitions are sufficiently high, further absorption to higher state will occur [56]. As it is non-linear interaction, the absorbance of *N*-photon absorption is proportional to I^N, where *I* is intensity of the laser field. The wavelength dependence is less significant.

Multiphoton absorption can be achieved with high-power CW laser with short wavelength, or short pulse laser with wavelengths lower than the band gap. It is suitable for processing transparent materials that do not have absorption bands in the visible region. The reported structural change in fused silica shows smooth refractive index change[57], micro voids[58], and birefringent zone which may introduced by either laser-induced stress or formation of self-ordered nanograting of subwavelength periodicity perpendicular to the laser light polarization [59]. The permanent, highly localized modification depends on exposure repetition rate, pulse duration, intensity, and even polarization[60].

1.3 Glass device fabrication with laser processing

Laser irradiation has great benefit to allow us spatial design and fabrication of complex structure integrated in glass monolithically. With selected glass composition and laser parameters, functional glass had been developed in various applications such as optical devices[57], microfluidics [61][62], high resolution 3D micro-structuring [63][64], and surface treatment[65][66]. Laser irradiation induces physical and/or chemical changes in the glass structure. Understanding their critical mechanisms in atomistic level gives significant keys for finding better irradiation condition and development of further advanced processing on glass.

1.3.1 Nanoscale structural modification of glass by CW laser partial heating

"**Laser heating**" is one of the fundamental processes to realize high temperature treatment above glass transition temperature in local region without total deformation of glass sample. Glass is frozen-in certain metastable condition determined by previous thermal history. Laser heating moves the glass towards another condition by giving rapid and drastic temperature changes around a focal point of the laser. Crystallization by laser heating has been well examined and crystalline phase control has been realized and various functionalities have been reported[67][54][68].

The porous silica has nanoscale empty volume inside the glass substrate. By partitioning the porous glass substrate, fluidics pathway with large area can be easily fabricated, as illustrated in **Figure 1.4**. The formation of partitioning requires partial

closure of porous structure. However, densification of porous structure for pore closure will cause excessive shrink of volume. On the other hand, partial homogeneous region in phase separated borosilicate glass will turn to closed-pore region in porous glass after acid leaching. Laser heating process to control phase separation of glass has not been investigated, and detailed progress and mechanism are still unclear.

Microfluidics fabrication using glass plate had been developed extensively by laser processing. Microfluidics, or microreactor is hand-on-chip technology which contains chemical flow inside the plate[69]. The chemical flow in microreactor is suitable for in-situ observation such as microscopy or Raman measurement. Also, temperature and flow control are much easier in microreactor due to its large specific surface area, which may also enhance reaction efficiency. High transparency and chemical and thermal resistance make a silica glass favorable for microreactor material. Although silica glass, the laser processing to crave the fluidics inside the glass substrate requires high cost including high power exposure using femtosecond pulse laser and longer irradiation time for the reactor with larger area (numbering up). Microfluidics made of porous glass plate is expected to have higher specific surface area and cheaper processing cost. For porous fluidics, laser irradiation is used for partitioning, and larger fluidics area can be obtained with shorter irradiation time than making hollow fluidics by laser irradiation, as illustrated in Figure 1.4. Therefore it is important to establish the

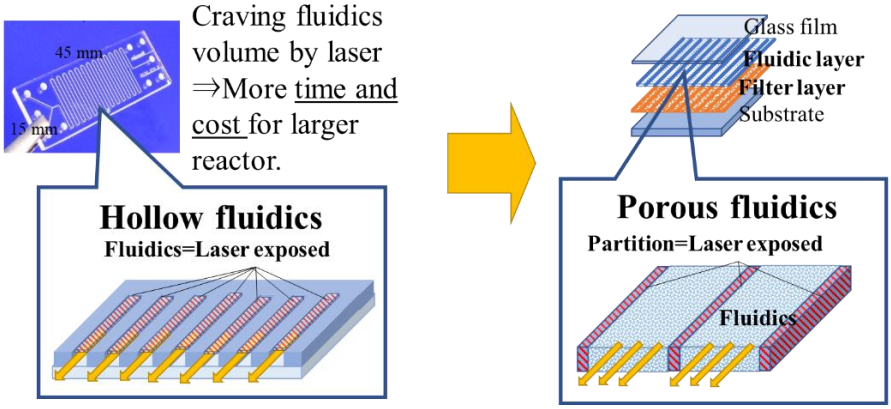

Figure 1.4 Schematics of microreactor fabrication process by laser irradiation on glass substrate.

1.3.2 3D micromachining on silica glass by combination of femtosecond laser irradiation and wet etching

Laser irradiated fused silica shows various modification nonlinearly depends on laser intensity and pulse duration[70][59], triggered by multiphoton absorption[71][72]. Band gap of fused silica is about 8.9~9.3 eV, which is larger than energy capable of obtaining from continuous or long pulse light beam[73][74]. But femtosecond pulse beam excites multiple electrons before heat transfer to surroundings by electron-phonon energy transfer. This consequence of light absorption enables transparent materials to be modified inside the material, with small heat-affected zone around focal point[75][76].

After femtosecond laser irradiation, physical and chemical changes in highly localized area remain in fused silica. Visible textures such as nano gratings[59][77], bubbles with crystals[78][79], micro voids[80], and so many distinctive changes[81] remain after irradiation. On the other hand, there are invisible changes such as refractive index[57][82], stress and strain [83], and mechanical properties such as thermal expansion coefficient[84], Young's modulus[85][86] and density[87][88]. The local volume change is primitive cause of various modifications[89]. The entire profile of local volume change is observable when modified property is measurable. Though it is difficult to see detailed gradation of material properties after writing complex design inside the material.

Many applications of fused silica processing using femtosecond laser have been investigated in past decades[90]. 3D micro processing of fused silica is one of the unique fabrication processing which cannot be realized in other method, as the schematic of processing flow illustrated in **Figure 1.5**. When femtosecond laser is irradiated to fused silica in particular condition, point defects are generated[39]. These defects change chemical durability significantly. Compared to non-irradiated fused silica, laser irradiated zone has more than 100 times faster etching rate[91][92]. Since femtosecond laser irradiation only affect localized focal point inside the glass, direct writing of hollow channel is possible after etching[93]. Complex monolithic micro structure made of fused silica can be obtained with 2 steps fabrication process[62]. This technique enables fabrication of micro-scale complex structures without any additive material and boundary. Taking advantage of transparency and high chemical durability of silica, 3D micro structures fabrication process are mainly used in the field of bio micro devices[94][61], MEMS[95][96], and even as a 3D printing plat form for fused silica[63].

During the process, etching seems to wash away all laser irradiated area. But surface

of laser irradiated area has slightly different texture and properties compared to normal fused silica without processing. Laser irradiation effect is significantly high at center of focal point, so surrounding, which has twice deeper effect zone than focal point[97][76], were not focused in the past researches. Though it is important to evaluate how material changed after processing, because volume fraction of modified material in microstructures is significantly larger compared to macroscale objects. Femtosecond laser machining is becoming more familiar both in laboratory and industry[98][90], it is necessary to understand material properties change and how those affect to both static and dynamic behavior.

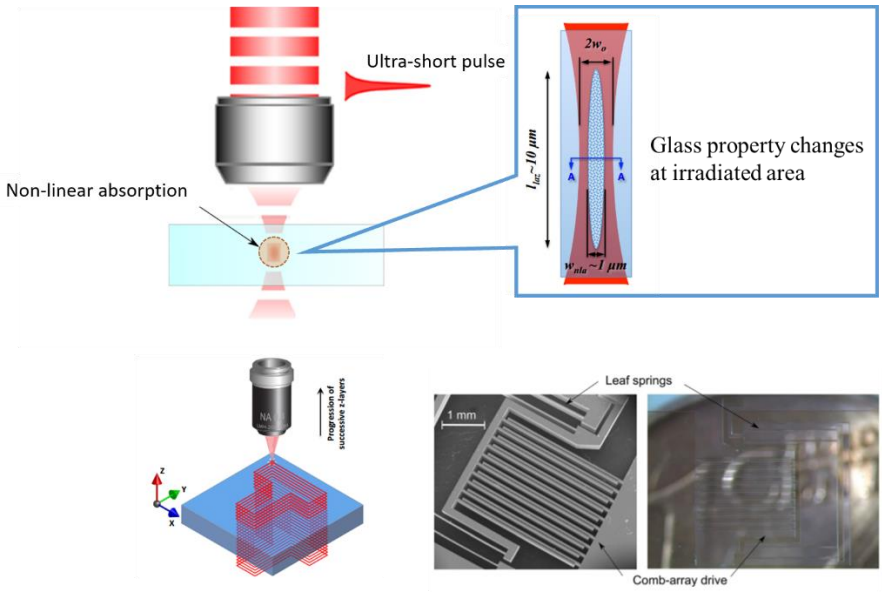

Figure 1.5 Schematics showing 3D micro-processing of silica glass using femtosecond laser irradiation and acid leaching. [62] **The laser exposed volume shows lower chemical durability.**

1.4 Focus of this study

This study gave focus on the nano-micrometer size structural modification of glass materials using laser processing. When the light with high power density from laser is absorbed in the glass, the physical and chemical reaction occurs at exposed volume and causes structural modification. By selecting the combination of glass composition and laser irradiation method, various structural control at exposed area could be expected. In order to realize desirable nano-microstructure implementation on a glass substrate, understanding of interaction between laser light and glass material is necessary.

Control of nano-micro structural change by laser irradiation including spatial distribution of the modification is important to design monolithic integrated devices. Miscible/immiscible phase transformation of glass is chosen to be controlled using local rapid heating and cooling by CW laser to develop microreactor device in borosilicate glass. The chemical and physical reaction during laser heating was estimated by high temperature in-situ spectral measurement on glass and melt.

Also, the effect of defect formation on the dynamic functionality of glass is given focus to be controlled using multi-photon absorption of femto-second pulse laser to develop micrometer size vibration device of silica glass implementing Acoustic Black Hole effect.

1.5 Objective

The objective of this research is to understand the mechanism of nano-microstructural modification via laser absorption in glass. High energy density exposure in localized time and space by laser irradiation would transform the glass structure into unique metastable state and results in permanent modification at room temperature. The laser-absorbed energy diffusion at surrounding of the focal point and response of the glass structure to those given energy were investigated.

In order to control the local glass nano-microstructure by laser processing, modification mechanism should be clarified and investigated through structural analysis by spectroscopy and physical reaction estimation by calculation using finite element method. Two different approaches with different laser oscillation method were focused on this study for purpose of monolithic glass device designing: Heat introduction borosilicate phase separated glass substrate by CW laser and defect formation in silica glass substrate by femtosecond pulse laser. Through understanding respective topic, the possibility of laser processing on glass material by nano-micro structural modification had been discussed.

2 Space selective porous/non-porous design on silicate glass substrate by CW laser

2.1 Introduction

In this section, non-porous region was introduced to porous silica glass substrate by single laser scanning as illustrated in **Figure 2.1**. Since porous glass has ability to pass through the fluids and gas, the partition made of non-porous region would enable fabrication of monolithic porous silica microreactor with large fluidics area by simple process. Monolithic porous/non-porous designed silica glass substrate would realize highly transparent, chemical and thermal resistant microreactor with large specific surface area. In order to realize the glass substrate with porous/non-porous area designed on the same plane, CW laser heating was used to partially modify the glass structure.

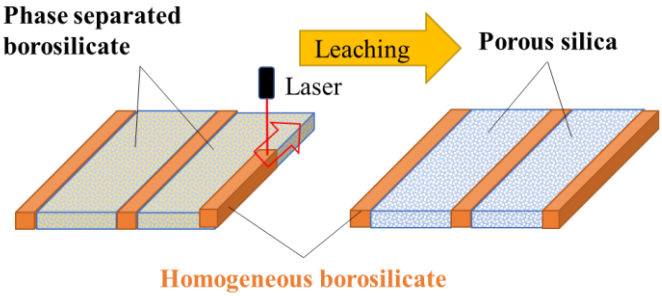

Figure 2.1 Schematic illustration of porous/ non-porous designed glass substrate fabrication process. In phase separated region, borate rich phase including additive transition metal ion is washed away by acid leaching.

Na_2O-B_2O_3-SiO_2 (NBS, or sodium borosilicate) glass turns into nano porous silica glass, taking advantage of spontaneous phase separation and acid leaching[99]. Borosilicate glass with low alkali content separates into SiO_2 rich phase and B_2O_3 rich phase interconnected in nanoscale, so called spinodal phase separation. By acid leaching, B_2O_3 rich phase can be washed away and SiO_2 rich phase remains as porous silica. The size, specific surface area, and pore size depends on morphology and composition of the immiscible nano phases in borosilicate glass[14]. Those characteristics of phase separation strongly depends on the thermal history of heat treatment including temperature and time. As shown in **Figure 2.2**, below miscible temperature there are two distinctive compositions where Gibbs free energy ΔG is minimized. With certain diffusivity of chemical component, glass start to show these metastable compositions by

separating into different nano phases. The phase separation develops faster in higher temperature due to lower viscosity, though the contrast of chemical composition between two phases become less significant at higher temperature. The porous glass consists of 96% silica can be obtained from borosilicate glass heat treated under 500~600°C for few hours[100]. On the other hand, it can be assumed that the mixture will take place in very short time above miscible temperature, due to its low viscosity. Considering that the laser light has high power density, homogenization of phase separated glass by laser heating appears to be suitable for designing porous/non-porous region on the glass substrate.

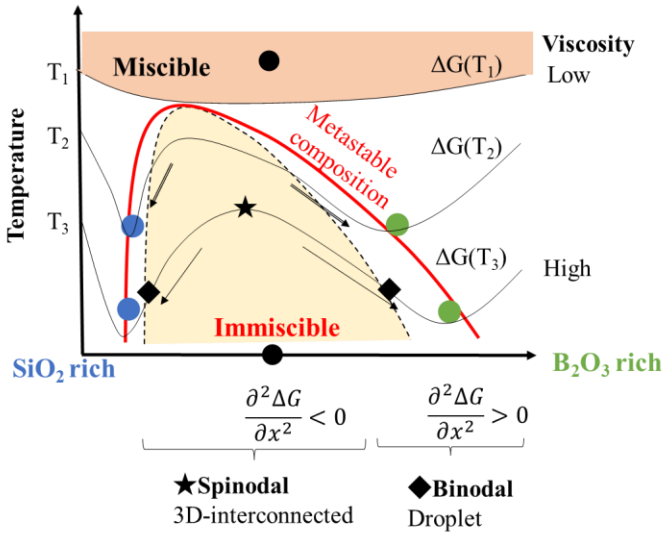

Figure 2.2 Composition and temperature dependence of Gibbs free energy. When the composition of the glass show high Gibbs energy as marked with ★, phase separation proceeds to minimize the Gibbs energy by turning into two different composition marked with ●.

For fabrication of the porous/non-porous designed glass substrate, the homogeneous region is required to be penetrated from top to bottom surface to show function as a partition, as explained in **Figure 1.4**. It also requires clear boundary between porous and non-porous volume to avoid uneven distribution of the flow inside porous fluidics. The formation of partition inside porous silica glass had been tried with combination of contour made of femtosecond laser affected volume with height of 10 to 100 μm and surface densification by CO_2 laser [101]. This partition showed certain permittivity against water through interstitial between laser-drawn lines. In order to fabricate partition with enough quality, homogenized volume should have continuous and uniform volume.

Although, homogenization process of phase separated glass in high temperature has

not been focused and detailed mechanism is not clear. Even more, CO_2 laser heating is difficult to penetrate through the modified volume through substrate and femtosecond laser focal spot is too small to form uniform volume. Homogenization of phase separated borosilicate glass by single laser scan had never been realized previously.

In this chapter, phase separated NBS glass substrate were partially homogenized by laser heating using transition metal ion as a heat source. With few additive transition metal ions which absorbs laser with NIR wavelength, the glass matrix transmits the laser and moderate temperature increase would be possible by heat emitted from d-d transition. As a laser absorbing heat source, NiO or CuO was added to absorb continuous-wave laser with λ=1064 nm. Laser was irradiated on phase separated borosilicate glass plate with various scanning speed. By acid leaching the laser irradiated glass sample, porous /non-porous region was expected to be formed through top to bottom surface of the porous glass substrate.

2.2 Experimental

2.2.1 Synthesis

Glasses with composition $6.8Na_2O$-$31.1B_2O_3$-$62.1SiO_2$ (in molar ratio, $R=Na_2O/B_2O_3=0.22$, $K=SiO_2/B_2O_3=2$) containing x=0.2, 0.4, 0.8, and 1.0 mol% NiO (NBS-xNiO) and x=0.2, 0.4, 0.8 mol% CuO (NBS-xCu) were fabricated with conventional melt-quenching method. Reagent grade materials (FUJIFILM Wako Pure Chemical Co.) were wet-mixed using ethanol. After drying, powders were melted in a platinum crucible at 1000°C for 1 hour and then in 1550°C for 2 hours. For achieving higher glass homogeneity, the quenched bulk glasses were crushed and melted again at 1550°C for 2 hours 1-2 times. After melting, the glasses were finally poured into a pre-heated glassy-carbon mold. These glasses were immediately put into the furnace at 450°C and cooled to room temperature at -1 K/min (Hereafter named As-melt sample; AM). Annealing temperature was set lower than phase separation growing temperature. The obtained bulk glasses were sliced into plate with the thickness of 0.5~0.8 mm and polished.

2.2.2 Optical absorption spectroscopy

The optical absorption spectra were collected at room temperature with UV-Visible spectrometer (V-570, Jasco) with resolution of 2 nm. The thickness of the samples was about 2 - 3 mm for the glasses heat-treated at different temperatures followed by water quenching. The spectra were normalized by sample thickness to obtain absorption coefficient. The target composition for laser processing were decided based on the absorption behavior and apparent transparency of the fabricated glass.

2.2.3 Thermal analysis

The differential thermal analysis of powdered NBS glasses. Thermomechanical analysis (TMA) was conducted on the rectangular sample with a compressive stress of 49 mN by TMA8310 (Rigaku) at rate of 5°C/min on heating from room temperature to melting point of respective glass. For NBS-0.8NiO, TMA was measured for 6 different points cut put of melt-quenched glass block in order to confirm the homogeneity.

2.2.4 Laser scanning on glass plate

For laser irradiation test, high-power continuous-wave (CW) Yb fiber laser with a wavelength of 1064 nm was irradiated on **PS** glass sample (before leaching) with an objective lens of 5X (NA: 0.13, spot size: 10.8~16.3 μm). Irradiation power was fixed at 4.3 W, 5.7 W, and 7.2 W and scanning speed was changed; 1.0 mm/s, 0.5 mm/s and 0.1 mm/s. Scanning position was controlled by 2-axis (XY) stepping motor stage. The focal point was set at the surface of the glass plate. The glass was pre-heated at 100°C. Laser was scanned along X-axis direction in **Figure 2.3**, and laser incident was done along with Z-axis direction. More than 10 lines were drawn in parallel, with 300~500 μm spacing between the lines.

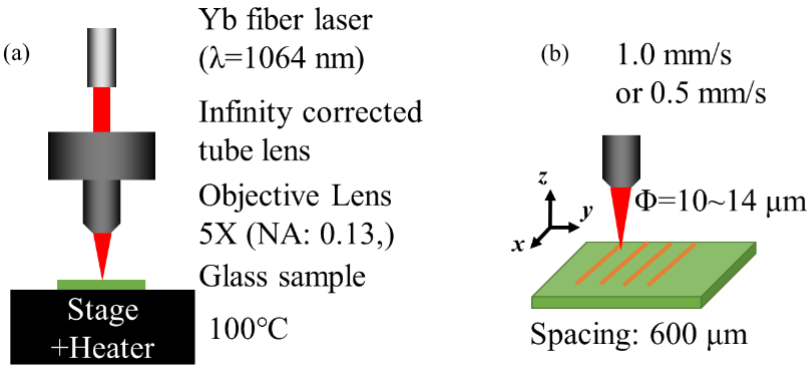

Figure 2.3 (a) Optical system set up for laser irradiation (b) Schematic figure showing laser scanning procedure

2.2.5 Post processing for porous structure formation

Both laser-irradiated and non-irradiated glass pieces were leached in the 95% H_2SO_4 at 98 ℃ for 3 days to remove B_2O_3-rich phase. The glass samples were put in 1.3% KOH for an hour to remove silica-gel layer covering pore surface. After taking out from leaching bath, glass pieces were put into ethanol for a day to remove leaching liquid inside porous structure.

2.2.6 Evaluation of porous structure

The porous structure of leached glass piece was evaluated by N_2 gas adsorption test (Belsorp 28, Bel Japan Inc.) for obtaining pore properties. Before BET measurement, the sample was crushed into powder and dried under vacuum at 100 ℃ for 24 hours.

For checking the amount of residual NiO after leaching, X-ray fluorescence (XRF, M4 TORNADO, Bruker) with spot size=25 μm was used to analyze 8~20 points each on the sample surface. Measurement spot was set at a random point with similar appearance within 0.25 mm^2.

2.3 Results

2.3.1 Optical absorption behavior at room temperature after fabrication

Figure 2.4 shows UV-vis-NIR absorption spectra of **NBS-*x*NiO** and **NBS-*x*CuO** glass and (b) appearance of each **AM** (as-melt) glass after slicing into 1.5~2 mm. The coloration of glass pieces with NiO showed various colorations due to drastic absorption coefficient change in visible region. That color center is originated from d-d transition of Ni^{2+} ion surrounded by ligand oxygen. NBS-0.2NiO showed the most significant absorption band at 420 nm, but absorption at 1064 nm was unobservable. For *x*=0.5-1.0 in NBS-*x*NiO glasses, several absorption bands were observed at UV-vis-NIR region until 1700 nm, with the highest absorption at 420 nm. Although, the intensity was not proportional to the NiO concentration, and the base line was different among compositions. The apparent absorbance was independent of NiO concentration at λ=1064 nm, which is same as laser wavelength, without considering the scattering effect. As shown in **Figure 2.4** (b), the transparency was lost above *x*=1.0. **NBS-4.0NiO** showed opaque appearance due to strong phase separation development during melt-quenching process. Considering the purpose of homogenization by laser heating, NBS-0.8NiO was selected as the target composition for laser processing.

The right side in **Figure 2.4** shows the result of NBS-*x*CuO glasses. The intensity of the most significant absorption band at 780 nm was proportional to the CuO concentration. NBS-0.4CuO was chosen as the laser processing glass composition since the glass composition had shown similar absorption coefficient as NBS-0.8NiO.

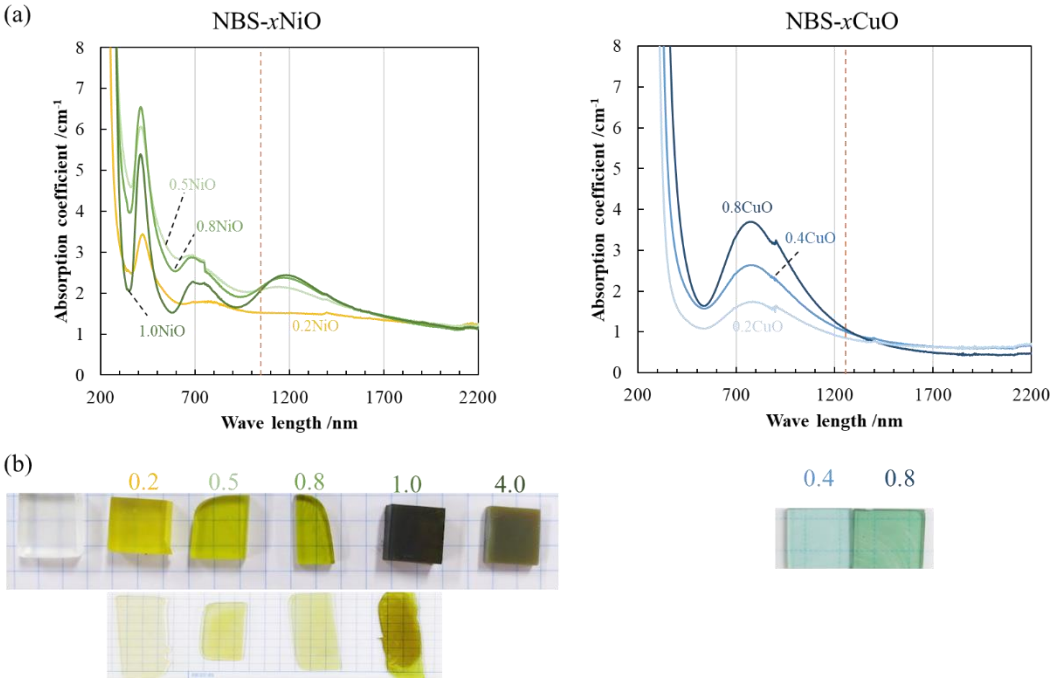

Figure 2.4 (a) UV-vis-NIR absorption spectra and (b)appearance of NiO and CuO containing NBS glasses.

2.3.2 Thermal properties

The DTA curve of the NBS glasses are shown in **Figure 2.5**, in which the glass transition (Tg) could be assigned. The Tg of each glass samples are shown in **Table 2.1**. The crystallization of NBS could not be found in all the NBS glasses. The effect of crystallization is neglected in the later analysis. The melting point was difficult to define with gradual decrease of heat absorption. TMA curve was plotted **Figure 2.4** (b). The coefficient of thermal expansion (CTE) at 100-400°C was calculated from TMA curve and shown in **Table 2.1**. The results were compared with NBS glass without additional TM ion. The T_g increased when 0.8 mol% of NiO was added to NBS glass by 17.5°C. Increase of T_g was less significant with NBS-0.4CuO by 5.6°C. Contrary, CTE decreased by addition of TM ion, at most 11 % reduced from NBS glass.

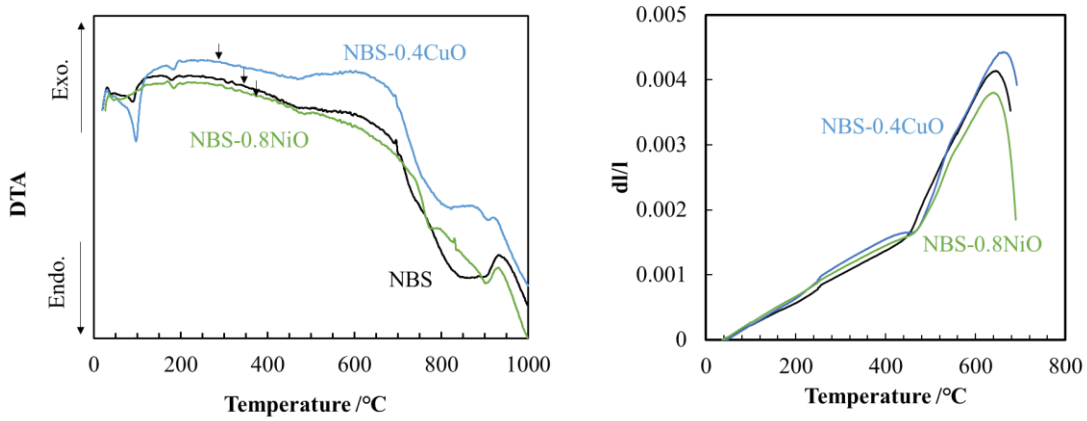

Figure 2.5 (a) UV-vis-NIR absorption spectra and (b)appearance of NiO and CuO containing NBS glasses.

Table 2.1 Glass transition temperature Tg obtained from DTA and TMA measurement. Coefficient of thermal expansion (CTE) was obtained from line slope at the range of 100~400°C.

	Tg (DTA)	**Tg (TMA)**	**CTE $*10^{-6}$/K (100~400°C)**
NBS-0.8NiO	370°C	473.5 (±1.3)	3.48 (±0.08)
NBS-0.4CuO	310°C	461.6 (±1.7)	3.67 (±0.09)
NBS	350°C	456.0 (±2.1)	3.92 (±0.17)

2.3.3 Glass plate appearance after laser irradiation

Figure 2.6 shows the comparison between CO_2 laser and Yb-fiber laser irradiated sample on the NiO-containing phase separated glass plates. The cross section of laser irradiated glass was observed by optical microscope after acid leaching. The numbers in left top of each photo shows proportion of residual NiO after leaching at irradiated line center surface: all the NiO would be washed away when the glass is phase separated due to selective distribution of TM ion in borate rich phase, and 100% of NiO (Ni^{2+}) will remain when the silica rich and borate rich phase are miscible (homogeneous). In any laser irradiation condition shown in **Figure 2.6** shows certain amount of residual Ni^{2+} ion, indicating homogenization due to laser exposure. The amount of residual Ni^{2+} was higher in Yb-fiber laser irradiated glass compared to CO_2 laser irradiated.

The laser penetrated depth is the most significant difference among different lasers used for irradiation. The irradiation with CO_2 laser gives observable modification at most 100 μm below the surface. When the exposed energy is relatively high with high laser power and slow scanning speed, the glass surface was ablated at the center surface. Contrary, the glass modification after Yb-fiber laser irradiation had deep penetration depth more than 300 μm below the top surface. By preparing thin glass plate (<~800 μm, depends on irradiation condition), the partial glass modification from top to bottom surface was possible. The slight ablation could be observed at the surface when exposed energy was high, still the apparent glass modification penetrated well. For the purpose of porous/non-porous designing for microreactor, consistent modification of glass plate from top to bottom surface is necessary. In this paper, we focus on laser irradiation using Yb-fiber laser.

Figure 2.7 shows the typical sample appearance of laser irradiated NBS-0.8NiO and NBS-0.4CuO glass plates before and after acid leaching. In both samples, the glass turned from colored-transparent to opaque by acid leaching, which indicates the removal of B_2O_3 rich phase with color-center TM ions. The color due to presence of TM ion was remaining selectively at laser irradiated area. The partial homogenization of phase separated borosilicate glass could apparently achieved with additive TM ions (Ni^{2+} and Cu^{2+}) as a heat source for laser absorption. The porous structure characterizations are shown in **Table 2.2**. The porous silica has average pore diameter of 6~10 nm soon after acid leaching, and 30~40 nm after silica gel removal by KOH treatment. Most of the porous characterization merely showed difference among different additive TM ion in either As-melt and 580°C-4 hour treated samples.

(a)

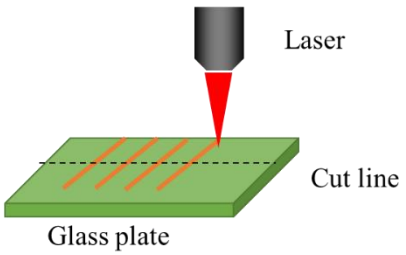

(b)

	CO_2 laser (λ=10.6 μm)		Yb-fiber laser (λ=1064 nm)	
	0.66 W	1.2 W	4.3 W	5.7 W
0.5 mm/s Cross section 100 μm		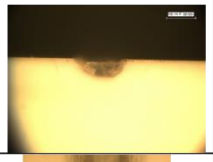	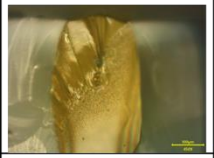	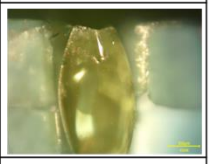
Top surface		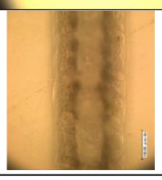	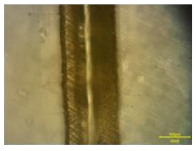	
0.1 mm/s Cross section	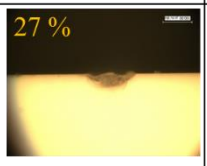	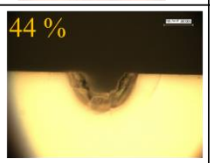	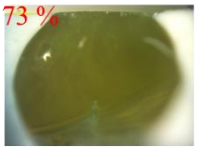	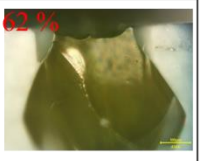
Top surface	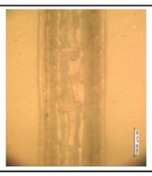	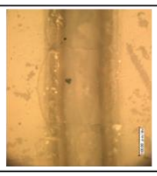	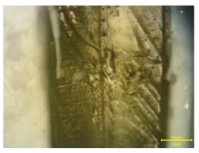	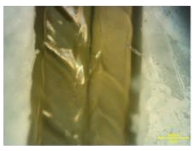

Figure 2.6(a) Schematic showing laser scan direction and cut line for cross section observation. (b) The cross-section image of laser irradiated glass plate with CO_2 laser (left 2 columns) and Yb-fiber laser (right 2 columns).

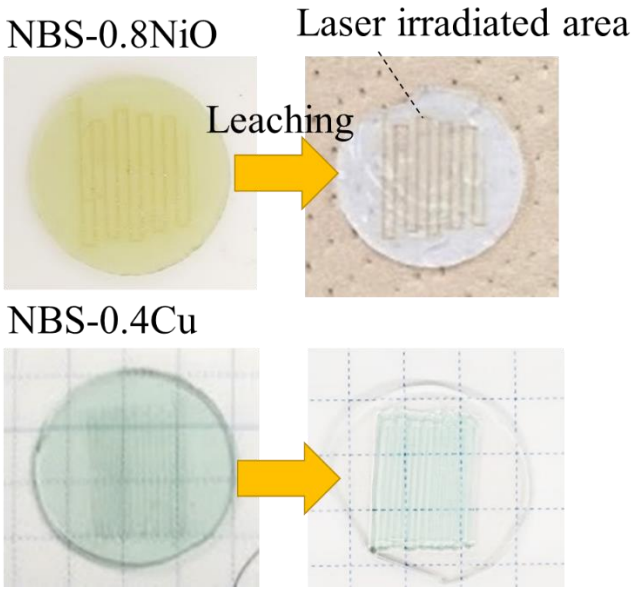

Figure 2.7 Before and after leaching of laser irradiated glass plates (Φ=7 mm) with 5.7 W,1 mm/s, pre-heating at 100℃.

Table 2.2 The porous structure characterization by BET analysis

Initial condition and leaching process	**As-melt (AM) →H_2SO_4**		**AM→580℃ 4h →H_2SO_4**		**AM→H_2SO_4 →KOH**
Composition	**NBS-0.8NiO**	**NBS-0.4CuO**	**NBS-0.8NiO**	**NBS-0.4CuO**	**NBS-0.8NiO**
N_2 adsorption volume [cm^3/g]	**23.205**	**22.866**	**26.249**	**26.827**	**6.256**
Specific surface area [m^2/g]	**101.00**	**99.525**	**114.25**	**116.76**	**27.23**
Total pore volume [cm^3/g]	**0.1675**	**0.1676**	**0.1827**	**0.2025**	**0.1872**
Average pore size [nm]	**6.6355**	**6.7375**	**6.3973**	**6.9359**	**27.50**

2.3.4 Laser induced modification at glass surface

The glass modification by laser irradiation would give various results depend on how the laser was irradiated. Firstly, the pre-heating temperature of the glass plate during laser irradiation was considered as shown in **Figure 2.8.** The glass plates tend to show cracks and collapsed without pre-heating. We assumed that the fracture was caused by residual stress dur to partial volume expansion by laser heating. The major cracks could be avoided by heating the glass plate above 100°C. Although the bubbles were found inside the laser exposed volume when the pre-heating temperature was above 200°C. In order to avoid secondary damage starting from those bubbles, the pre-heating temperature was set as 100°C in the following experiments.

Further details of laser heating mechanism were considered by focusing on dependence of laser output power and scan speed. Firstly, the laser modification effect at surface was analyzed by microscopic images and residual TM ion distribution observed by XRF. **Figure 2.9** shows the sample appearance of laser irradiated samples before (a) and after (b) acid leaching. magnified image of laser irradiated lines are shown below overview photo, e is shown, with concentration profile measured across the lines are plotted in (b). For **NBS-0.8 NiO**, slight color change was observed from green to brown at laser exposed area. The color change was significant with 7.2 W, especially the one with slower scanning speed. Although as shown in **Table 2.3**, the residual amount of Ni^{2+} ion at laser irradiated area decrease when the laser irradiation power is too strong, or scan speed is slow. On the other hand, NBS-0.4CuO showed less coloration change at laser irradiated area. Though after acid leaching, the residual Cu^{2+} ions were observed selectively at laser irradiated area. The amount of residual Cu^{2+} was higher with lower irradiation power. **Table 2.4** shows the line widths of laser irradiated area obtained from spatial distribution of residual TM ions. The apparent line width was matched to TM ion remaining width in **Table 2.5** within ±20%, where intrinsic error due to XRF plot resolution (±25μm) was from 3 to 20 %. The consistence of the results indicates that the apparent laser modification shows the certain degree of homogenization on phase separated glass. Though the concentration on residual TM ions was decaying with distance from focal point. Compared to the size of laser spot size (10~13 μm), the modified line width was 20 to 100 times wider. The heat generated by laser absorption seems to be diffused to the surrounding and induced the modification in wide area. The wider modified width by higher laser power indicates the further heat diffusion by higher input energy.

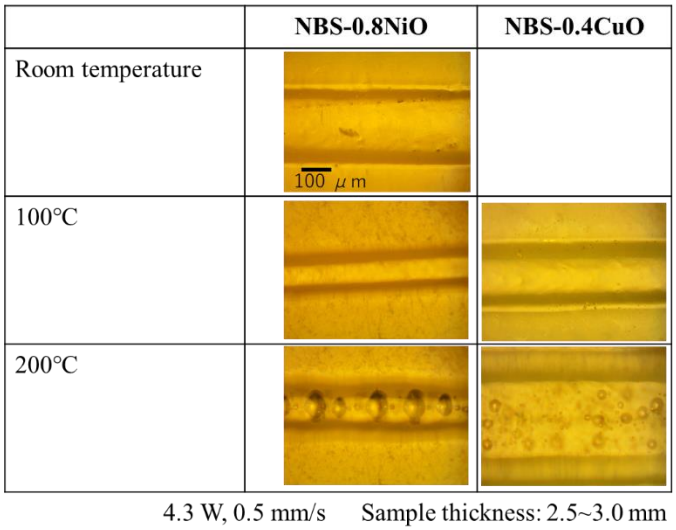

Figure 2.8The appearance of laser irradiated lines with different pre-heating temperature.

Table 2.3 The maximum amount of residual TM ion at laser irradiated lines compared to glass plate before leaching.

Residual TM ion (%)	NBS-0.8NiO			NBS-0.4CuO		
	4.3 W	5.7 W	7.2 W	4.3 W	5.7 W	7.2 W
1.0 mm/s	95	110	92	89.5	99	81.2
0.5 mm/s	100	95	72	103	77.5	73.8
0.1 mm/s	73	62	47	-	-	-

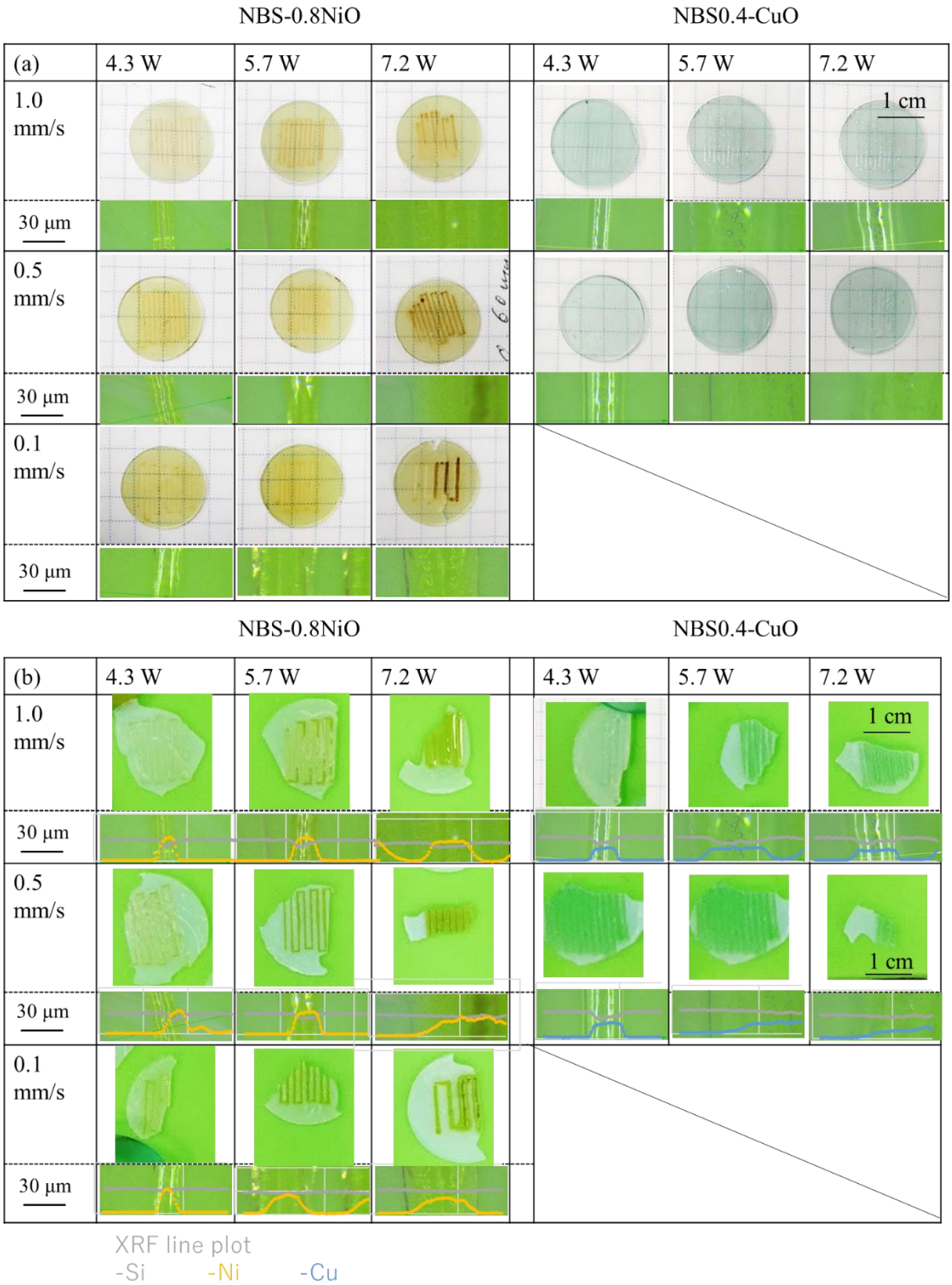

Figure 2.9 Laser irradiated samples with laser power and scan speed as parameters (a) before and (b) after acid leaching. The bottom row at each parameter shows the XRF

Table 2.4 The line width of laser irradiated lines analyzed from residual TM ion existing area.

1.0 mm/s	NBS-0.8NiO			NBS-0.4CuO		
	4.3 W	5.7 W	7.2 W	4.3 W	5.7 W	7.2 W
A. Ni^{2+} existing line width (μm)	258.68	318.42	716.43	358.7	883.51	678.42
B. Ni^{2+} existing more than 80% (μm)	119.39	159.2	358.21	239.12	622.47	438.98
Cut off region width *A-B* (μm)	139.29	159.22	358.22	119.58	261.04	239.44

0.5mm/s	NBS-0.8NiO			NBS-0.4CuO		
	4.3 W	5.7 W	7.2 W	4.3 W	5.7 W	7.2 W
A. Ni^{2+} existing line width (μm)	562.49	398.02	1591.08	441.75	1445.74	1638.44
B. Ni^{2+} existing more than 80% (μm)	120.54	218.91	59.7	341.43	843.9	199.8
Cut off region width *A-B* (μm)	441.95	179.11	1531.38	100.32	601.84	1438.64

0.1mm/s	NBS-0.8NiO		
	4.3 W	5.7 W	7.2 W
A. Ni^{2+} existing line width (μm)	299.26	656.72	795.7
B. Ni^{2+} existing more than 80% (μm)	119.71	79.6	0
Cut off region width *A-B* (μm)	179.55	577.12	795.7

Table 2.5 The apparent line width measured from optical microscope images.

Apparent line width (μm)	NBS-0.8NiO			NBS-0.4CuO		
	4.3 W	5.7 W	7.2 W	4.3 W	5.7 W	7.2 W
1.0 mm/s	219	315	662	315	963	528
0.5 mm/s	286	489	741	437	1600	1588
0.1 mm/s	413	625	796	-	-	-

2.3.5 Laser induced modification inside the glass plate

The laser modification inside the glass plate was observed by optical microscope and SEM on the cross-section vertical to laser scanned lines. **Figure 2.10** shows the laser irradiated NBS-0.8NiO with different laser power and scan speed. The top view and cross section the laser irradiated lines are shown in the table. SEM images were observed at boundary where the color contrast due to phase with /without TM ion. The clear boundary between porous/ non-porous region was obtained with 4.3W - 1.0 mm/s and 4.3 W - 0.5 mm/s. The Laser modified volume was reaching from top surface to the bottom using glass plate thickness of 400~600 μm. The modification along with z-axis (laser incident) direction was observed in detail as shown in Figure 8.2 (a)~(c). (a) 4.3W - 1.0 mm/s had clear boundary from top to bottom. (b) 4.3 W - 0.5 mm/s also showed clear boundary at top surface, but the porous structure gradually closed as the depth from the top surface get deeper. In order to obtain partially homogenized borosilicate region in porous glass substrate through top to bottom surface, laser scanning with 4.3 W – 1.0 mm/s with sample thickness of ~400 μm, or 4.3W – 0.5 mm/s with sample thickness less than 300 μm appeared to be suitable.

Contrary, the slow laser scan speed (4.3 W – 0.1 mm/s) lost the clear boundary around homogeneous region, with gradual appearance of porous structure as getting apart from the irradiation center. Both 4.3 W and 5.7 W showed laser irradiated cross section with widest homogeneous width at the middle point of the sample along laser incident direction. **Figure 2.11 (c)** shows distribution of nanoscale structure along horizontal direction (y-axis) against laser incident. When the overview of cross section was observed by SEM, the darkness volume containing Ni^{2+} ion was straight along z-axis direction, and the homogeneous region was surrounded by porous structure (1) with different silica volume compared to non-exposed area (2). Optical microscopic image could not distinguish homogeneous and porous region (1), showing Ni^{2+} coloration in both areas. The irradiated structure with same scan speed and different laser power (5.7 W – 0.1 mm/s) showed similar nanostructure distribution, with slight ablation at the top surface of glass plate.

When the laser power was increased up to 7.2 W – 1.0 mm/s, the width of laser irradiated area turned more than 6 times wider than the line irradiated with 4.3 W. The cross-section images showed more significant volume growth in horizontal (y-axis) direction inside the glass plate. The irradiated line with 7.2 W – 0.5 mm/s was wider than the interval between the lines and the homogeneous volumes sticked to each other, with 20~80 μm bubbles at 100 μm away from surroundings of laser irradiation center.

Figure 2.12 shows the results of laser irradiation on phase separated **NBS-0.4CuO** glass plates. The clear boundary between porous/ non-porous region was found with 4.3W- 0.5 mm/s. Contrary to NBS-0.8NiO, the irradiation with 4.3W – 1.0 mm/s on **NBS-0.4CuO** did not show clear boundary. The irradiation effect with 5.7 W was also significantly different between two different compositions. **NBS-0.4 CuO** showed 550 μm width by 5.7 W-1.0 mm/s, which is 3.5 times wider than the result of **NBS-0.8NiO**. Similarly, 5.7 W-0.5 mm/s and 7.2 W-1.0 mm/s showed much wider irradiated line on NBS0.4CuO than NBS-0.8NiO, though all the lines did not have clear boundary between porous/ non-porous structure.

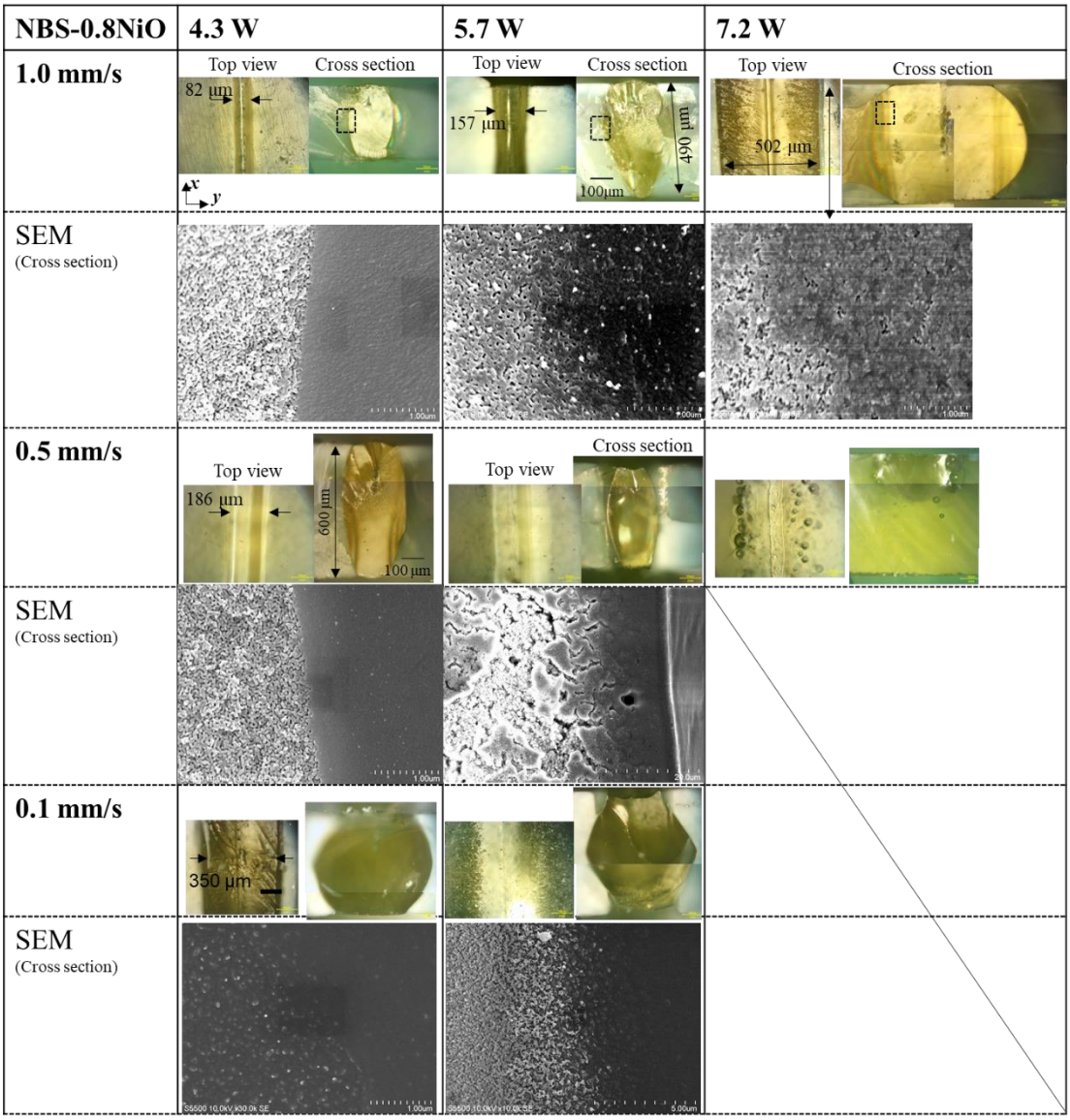

Figure 2.10 Top view and cross section of laser irradiated NBS-0.8NiO glass plates after acid leaching, with laser power and scan speed as parameters. SEM images were observed near the boundary between homogeneous region and nano-scale phase appearing region.

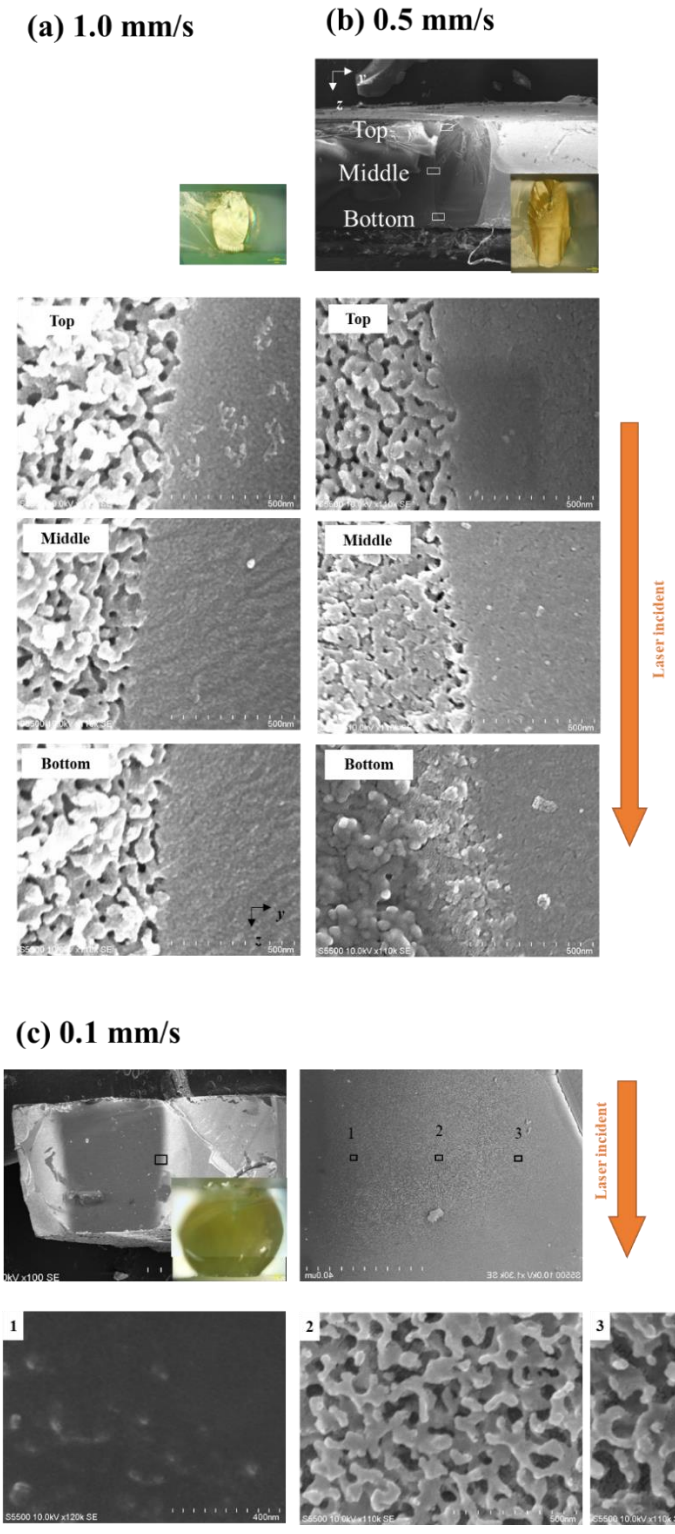

Figure 2.11 The porous/ non-porous boundary at top, middle, bottom part along laser incident direction. The phase separated glass plates were irradiated with 4.3 W with different scanning speed. (a) 1.0 mm/s, (b) 0.5mm/s, and (c) 0.1 mm/s.

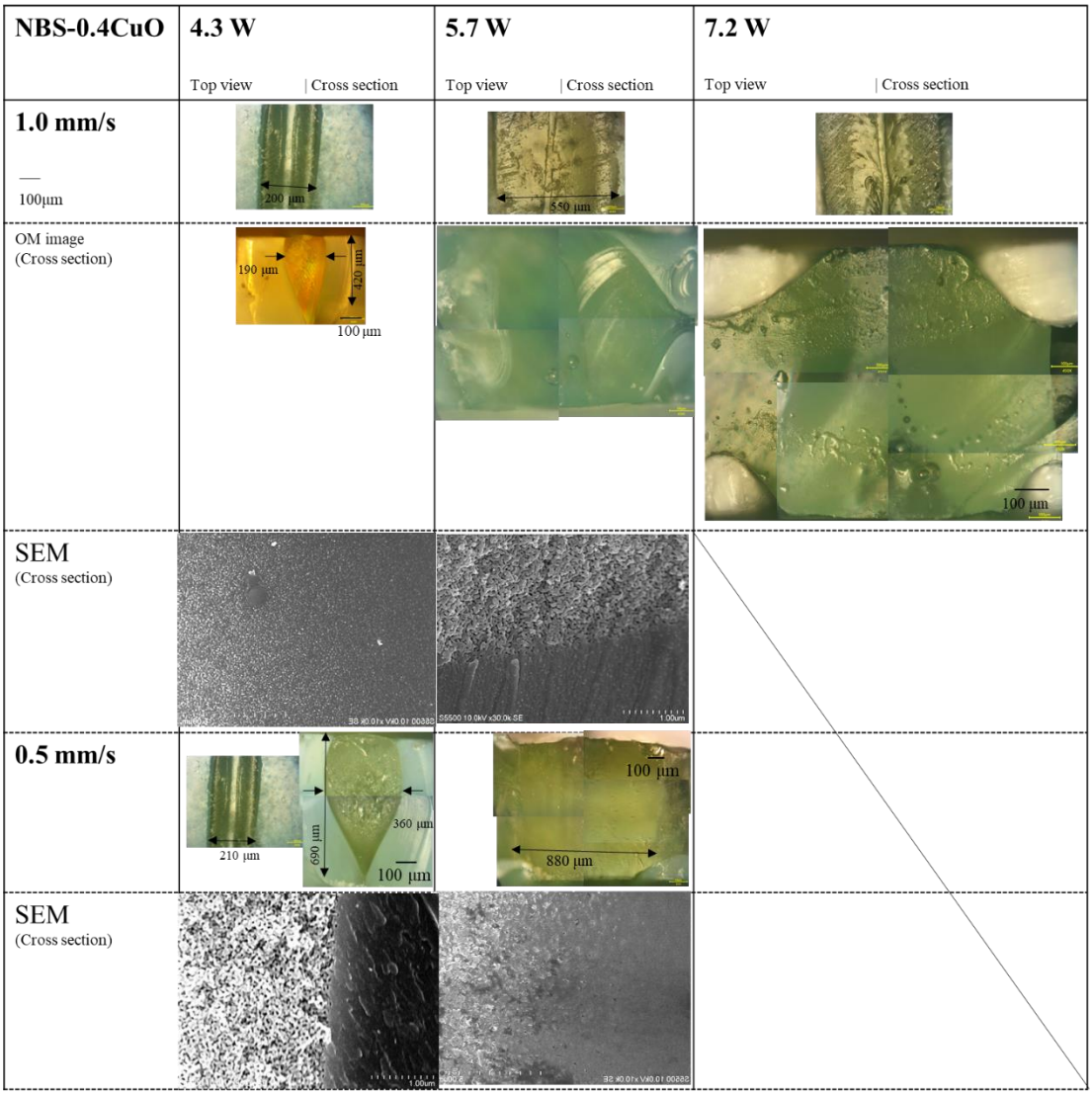

Figure 2.12 Top view and cross section of laser irradiated NBS-0.4CuO glass plates after acid leaching, with laser power and scan speed as parameters.

2.4 Discussion

2.4.1 The selection of glass composition

From **Figure 2.4**, absorption spectra of all NBS-*x*NiO showed similar absorption behavior as 6-coordinated (Ni^{2+} ion coordinated by 6 oxygen ions in octahedral configuration)[53]. Although due to slight spectral change in visible region, the color varied from yellow to green. Above *x*=1.0, the glass could not homogeneously mix after melt-quenching, showing unevenly distributed color. For *x*=0.2~0.8, the absorption coefficient at λ=1064 nm was independent of NiO concentration in NBS glass. Although under the actual laser irradiation with 10 W, both glass plate with *x*=0.2 and

0.4 did not show apparent modification even after exposure for several seconds. NBS-0.8 NiO showed different absorption behavior by changing laser power from 2~10 W, starting from slight modification to too intense absorption where the glass cracks soon after exposure. Such differences besides same apparent absorption coefficient may be due to effect of Rayleigh scattering observed 380-1500 nm, considering the decrease of transmittance at shorter wavelength (200~700 nm). NBS-0.8NiO was chosen for target composition, due to its homogeneity and it could be expected to adjust the effect of laser by changing the power.

For NBS-*x*CuO, absorption coefficient was almost proportional to the CuO concentration. NBS-0.8CuO showed too intense absorption at 10 W exposure. NBS-0.4 CuO showed similar absorption behavior to NBS-0.8NiO. Also, the absorption coefficient of λ=1064 nm of both compositions were α=2.0 cm^{-1}.

2.4.2 Absorption behavior with different doped ions species

By both **NBS-0.8NiO** and **NBS-0.4CuO** could successfully fabricate porous/ non-porous structure by partial homogenization of phase separated glass plate. As shown in **Figure 2.10 and 2.11**, the same laser power and scanning speed affected differently depends on doped ion species. The heat affected volume was larger in NBS-0.4CuO than NBS-0.8NiO, especially above 5.7 W. The laser irradiated volume inside the substrate expanded to horizontal direction toward beam incident direction as laser power increased. The irradiated lines next to each other started to be connected inside the glass, even when the lines are apparently separated at surface. And such a connection between lines could be observed with 5.7 W in NBS-0.4CuO and 7.2 W in NBS0.8NiO.

The absorbed laser light turns to heat and transferred to the surrounding volume as shown in **Figure 2.13**. There are two possibilities that may changes the laser modification effect in the glasses with similar absorbance: temperature dependence of absorption behavior and phase separation tendency. Firstly, the absorption coefficient depends on both wavelength and temperature. The absorption of laser is mostly due to d-d transition of additive TM ion in the glass. The temperature dependence of d-d transition behavior might be less significant at 1064 nm from previous report[102]. Further consideration will be in next chapter.

In addition to the absorbance of laser at 1064 nm, absorption behavior especially in visible to IR region directly affects radiative heat transfer inside the glass based on Rayleigh Jeans law, since oxide glass has high emissivity up to 0.9. It is reported that colored glass shows less radiative heat transfer [103]. The different absorption behavior

in visible region might have caused change in heat transfer behavior.

Another factor that may affect the laser modification is temperature dependence of phase separation. The typical phase separation behavior in ternary Na_2O-B_2O_3-SiO_2 system is reported in detail[104], and also the addition or alteration of glass components is known to change both the thermal properties and critical temperature[105]. The thermal properties from DTA and TMA measurement did not show significant difference between two different compositions, the effect at high temperature above Tg is still unclear.

The difference in phase separation behavior with temperature dependence will further discussed in chapter 4. The mechanism of clear boundary formation between porous/ non-porous structure will be discussed in chapter 5, based on the properties of glass and melt shown in following chapters.

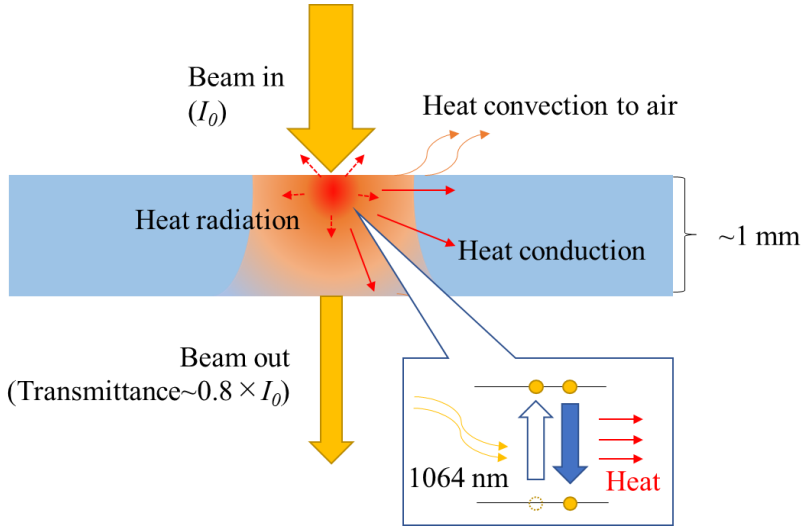

Figure 2.13 Schematic diagram showing laser absorption and heat transfer in the glass plate.

2.5 Summary

The phase separated sodium borosilicate (NBS) glass plate could be partially homogenized by CW-laser heating using transition metal ions as a heat source. Acid leaching on such a glass substrate washed away borate rich phase selectively realized glass substrate with porous silica/ non-porous borosilicate region exist on the same plane.

The CW laser with wavelength in NIR region could moderately be absorbed by Ni^{2+} or Cu^{2+} ion doped in borosilicate glass. NBS glass matrix has high transparency in NIR region, so the laser could pass through inside the glass substrate with slight absorption due to Ni^{2+} or Cu^{2+} ions. The homogenized region along the laser incident direction was penetrated through the glass substrate, beside using CO_2 laser where most of photon energy being absorbed at surface due to excessively high absorbance.

With fast laser scanning, the distinctive boundary between porous/ non-porous volume could be observed. This result indicates the possibility on microreactor fabrication by porous glass substrate consists of porous silica fluidics and borosilicate glass partition implemented with clear boundary.

3 Evaluation on phase miscibility in borosilicate glass probed by Ni^{2+} ion

3.1 Introduction

In chapter 2, the nanostructure of laser irradiated area was evaluated by FE-SEM observation. Although, direct observation of fabricated sample at ambient temperature only gives information after processing. Taking advantage of color change of Ni^{2+} after laser irradiation, miscibility of **NBS-0.8NiO** glass was evaluated by considering Ni^{2+} speciation as structural probe.

Since Ni^{2+} ion is sensitive to electron donor ability of its ligand, the change of oxide glass matrix would be reflected in its speciation. The speciation change of Ni^{2+} ion in glass is strongly dependent on its composition; 4-coordinated (Td) is dominant in glass composition with high optical basicity such as aluminosilicate glass[106]. 5-coordinated is dominant in most of the case with silicate glass[107]. In alkali borate glass, coordination number of Ni^{2+} ion is 5 to 6- coordinated (Oh) and it even forms Ni-enriched nanodomain when alkali concentration is low[108][109]. These compositional dependence can be expressed in theoretical optical basicity[106][110][111][112], which indicates electron donor ability of oxygen atoms in the glass system[113].

In order to understand the relationship between Ni^{2+} ion speciation and phase separation, the UV-visible-NIR absorption and Ni K-edge XAFS spectra were measured while glass sample was heating up to 1200°C. XAFS spectra was measured under high temperature in-situ, in order to avoid structural relaxation during cooling process. For further understanding on high temperature in-situ analysis, room temperature measurement with various heat treatment and direct nanostructure observation was practiced.

3.2 Experimental

3.2.1 Sample synthesis

NBS-0.8NiO glass with the composition of $6.8Na_2O$-$31.1B_2O_3$-$62.1SiO_2$ containing 0.8 mol% NiO (in molar ratio, R=Na_2O/B_2O_3=0.22, K=SiO_2/B_2O_3=2, M=63.26, Coefficient of thermal expansion=3.4 /10^{-7} K^{-1} at T<473°C, 13.8 /$10^{-7}K^{-1}$ at T>473°C) were fabricated with conventional melt-quenching method. Reagent-grade materials (FUJIFILM Wako Pure Chemical Co.) were wet-mixed using ethanol. After drying, powders were melted in a platinum crucible at 1000°C for 1 hour and then in 1550°C for 2 hours. These glasses were immediately put into the annealing furnace held at

450°C and cooled to room temperature at -1 °C/min. Further details of synthesis and its properties are on previous chapter. Hereafter the glass after above fabrication process was named "**As-melt (AM)**" sample**.** The glass showed light greenish transparency with spinodal decomposition which had already developed during annealing.

In order to consider the effect of phase separation on Ni^{2+} speciation, Al_2O_3-added glass with same *R* and *K* values, **NABS-0.8Ni**, was fabricated to be used as non-phase separated samples: composition 6.4 Na_2O-29 B_2O_3-6.4 Al_2O_3-58.1 SiO_2 containing 0.8 mol% NiO (*R*=0.22, *K*=2, M=65.73, CTE=$5.5x10^{-7}$ K^{-1} at T<480°C, $2.0x10^{-6}$ K^{-1} at T>480°C) . Synthesis process was same as that for **NBS-0.8NiO**.

3.2.2 Room temperature measurements on water quenched glasses

The glasses synthesized in section 3.1 was heat treated at various temperatures and water-quenched, to make the glass with frozen structure at elevated temperature. Hereafter these water-quenched glass is called **WQ.** The bulk glasses of both **NBS-0.8Ni** and **NABS-0.8Ni** were sliced into thickness of 0.5~0.8 mm and wrapped in Pt foil. These were heat-treated at temperature (in the range of 400~1000°C with 100°C step) for 20 minutes in the electric furnace. Soon after heat treatment, the glass piece in Pt foil was quenched in water.

These glass pieces were evaluated at room temperature and compared with spectral information obtained from high temperature measurements. XRD, optical absorption spectra, XAFS and SAXS were measured on WQ samples at room temperature. For checking the amount of residual NiO after leaching, X-ray fluorescence (XRF, M4 TORNADO, Bruker) with spot size=25 μm was used to analyze 5~10 points each on the sample surface. Measurement spot was set at a random point with similar appearance within 0.25 mm^2.

3.2.3 High temperature in-situ XAFS measurement

High temperature X-ray absorption fine structure (HT-XAFS) was measured at BL14B1 in SPring-8 (Hyogo, Japan). XAFS spectra were measured in transmission mode, from 8000 to 9250 eV using a Si (111) double crystal monochromator. Ni metal foil was used for energy calibration of absorption edge, *E*=8331.7 eV.

The **NBS-0.8NiO** glass rod (Φ=2 mm) was embedded in platinum ring (outer diameter =3 mm, inner diameter =2mm) and thickness was set to 0.8 mm. Before the measurement, the sample was heat treated at 1000°C for 20 minutes to erase phase separated structure once and water quenched in order to start the measurement with the sample glass more homogeneous.

Temperature program of the high-temperature measurement is shown in **Figure 3.1**. The sample was heated by the original compact furnace with a couple of SiC heaters located at 5 mm each from sample center. The platinum thermocouple in alumina protective tube (Φ=3 mm) was set 3 mm from sample center. The temperature was heated at 10°C/min and held at 600°C, 800°C, and 1000°C for 60 minutes and 1200°C for 45 minutes for XAFS measurement of 45 min.

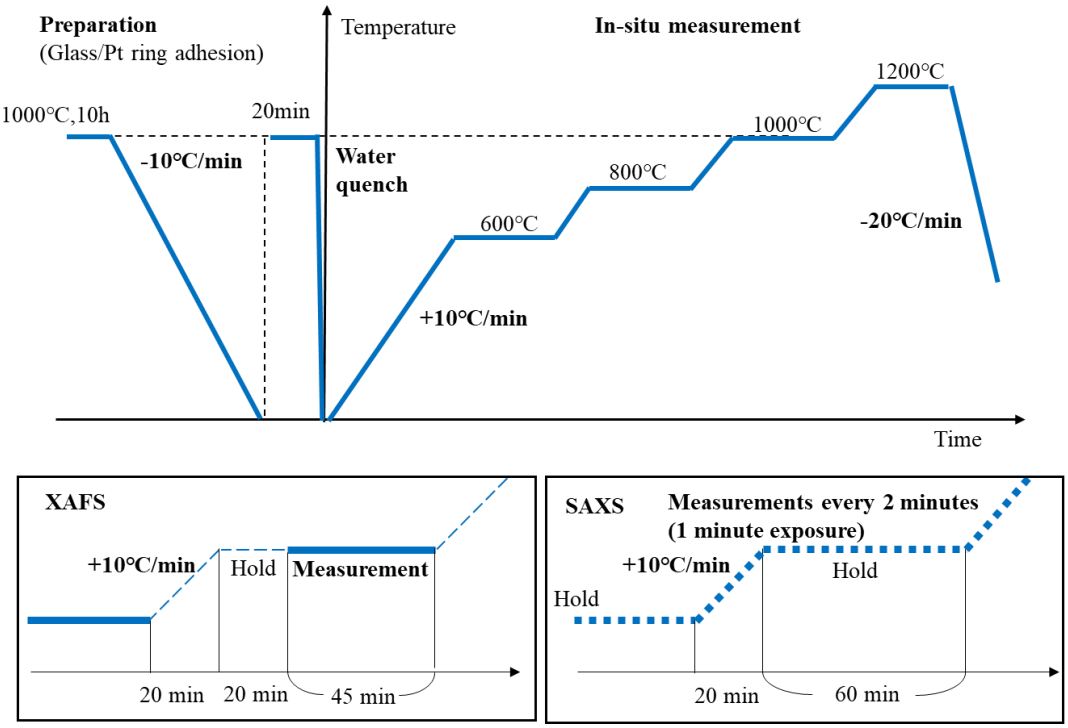

Figure 3.1 Temperature profile during high temperature in-situ measurement. Before the measurement, NBS-0.8NiO glass was heat-treated at 1000°C for 20 minutes and water-quenched immediately after taking out from furnace. XAFS signals were obtained in 45 minutes each, after holding at same temperature for 20 minutes. SAXS spectra was recorded every 2minutes during heating, including 1 minute exposure and 1 minute interval.

3.3 Results

3.3.1 Phase immiscibility evaluation of water-quenched glass by SEM images

Figure 3.2 shows SEM images of water quenched (WQ) samples after acid leaching and KOH treatment. The inset shows the appearance of each sample after leaching treatment. When the heat-treatment temperature was below 700°C, the visible color originated from Ni^{2+} ion (as shown in **Figure 3.4 (a)**) disappeared in WQ samples and turned to porous silica glass. Both 800°C-WQ and 900°C-WQ showed opaque appearance, and Ni^{2+} ion remained after leaching. 1000°C-WQ had transparent body and Ni^{2+} ion also remained. The quantitative amount of residual Ni^{2+} ion after leaching is on Table 3, measured by XRF. **NBS-0.8NiO 700°C-WQ** samples showed loss of most of Na^{+} and Ni^{2+} after acid leaching as well as **As-melt** sample, while 800°C~1000°C-**WQ** samples still contained most of them. These results indicate the existence of Ni^{2+} ion in interconnected borate rich-phase below 700°C, and transfer to different immiscible phase above 800°C. The most of **NABS-Ni** glass showed few components loss through acid leaching.

From SEM images of **NBS-0.8NiO(WQ)** in **Figure 3.2**, **As-melt** sample showed clear porous silica structure with average pore diameter of 50 nm. The 600°C-**WQ** glass showed silica network in nanoscale which was similar as **As-melt** glass, though silica rich phases were more aggregated, and the pore structure could not be observed clearly. Similar nano scale structure was found in 700°C-**WQ** sample, with slightly larger scale of silica rich aggregations than 600°C-WQ. In 800°C~1000°C-**WQ**, it was difficult to obtain SEM images of fine structures probably due to low composition contrast. Still some nanostructure could be observed in **NBS-0.8NiO** 800°C-WQ as shown in **Figure 3.2 (d-1)**, showing several dark spots about 600 nm, which might be the trace of residual borate rich phase, without interconnected structure in spinodal. Also, the small spherical dots with average diameter of 32 nm. The SEM image was clearly different from **WQ** samples treated under lower temperature, similar to fitting model change in SAXS spectra. 900°C-**WQ** sample showed similar nanostructure as 800°C-WQ, with larger number of dark spherical dots. The size of spherical dots appeared larger than 800°C-**WQ** up to diameter of 150 nm.

Figure 3.3 shows USAXS and SAXS spectra of **WQ** samples measured in ambient temperature. The **NBS-0.8NiO** glass soon after annealing (**As-melt**) showed typical spectra with spinodal phase-separation, similar to the spectra found in 600°C in-situ. Below 700°C-WQ, the spectra showed similar Bragg like peak with different peak position depends on heat treatment temperature. The spectra appearance significantly changed above 800°C. Convex curve was observed at low-q region (q=0.05~0.1 nm^{-1})

for 800 and 900°C-**WQ**. The 900°C-**WQ** sample even showed small sequential peaks at high-*q* region due to interference between scatterers. The 1000°C-**WQ** sample was totally different from other spectra and showed scattering intensity over entire q region. The residual scattering below q=0.1 nm^{-1} may be due to scatter from glass itself or air in the path.

On the other hand, all **NABS-NiO(WQ)** glass samples had similar low scattering intensity as that of **NBS-0.8NiO**(1000°C-**WQ)**. The scattering intensity of all samples showed a linear decrease with increasing *q*, showing similar spectra among all heat treatment temperature. The part of slight shoulder seems to be appearing at 900°C-WQ. From **Figure 3.4 (c)**, the appearance of NABS-WQ sample from 800°C~1000°C-WQ showed inhomogeneity in milli-scale, diverged into transparent, orange area and totally opaque, green area. The transparent area was mainly used for evaluation, but opaque volume might have contaminated during sample preparation. A small peak at q=0.5 nm-1 is due to capton tape in beam line, which was not observed in the spectrum of **NABS-NiO(**1000°C-**WQ)** without capton tape.

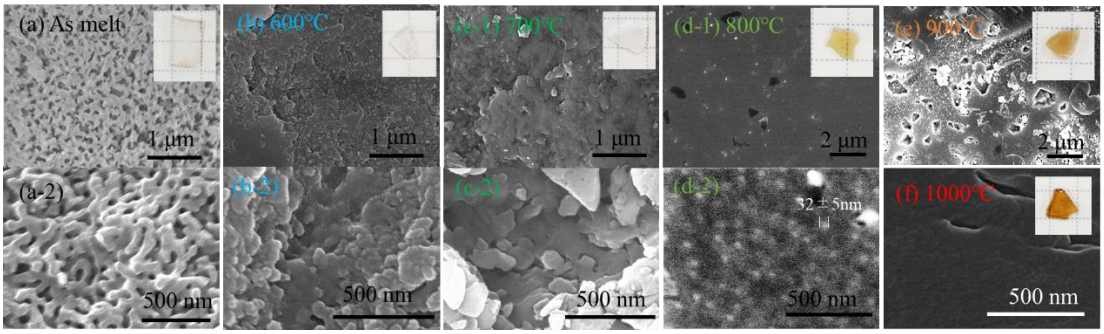

Figure 3.2 SEM images of NBS-Ni (WQ) samples after acid leaching and KOH treatment. Inset photos show the appearance of each sample.

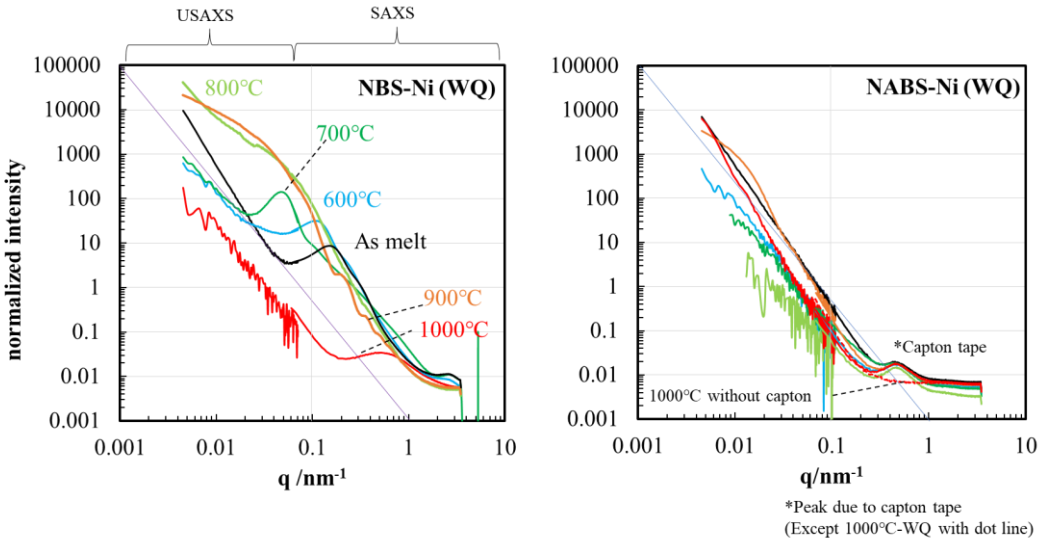

Figure 3.3 Room temperature SAXS + USAXS spectra of NBS-Ni(WQ) and NABS-Ni(WQ). As-melt glass pieces were heat-treated at respective temperature for 20 minutes and water-quenched. Spectra of NABS samples were affected by capton tape in sample holder, due to its low scattering intensity in high-*q* region.

3.3.2 Optical absorption of water quenched glass after heat treatment

As shown in **Figure 3.4**, **NBS-0.8NiO** and **NABS-0.8NiO** glass showed color and opacity variation depending on the temperature before water quenching. Coloration due to Ni^{2+} ion revealed significant change in high temperature treatment followed by rapid quenching. The color gradually turned from green, yellow, to brown as treatment temperature increased. The samples quenched from 800 ^{o}C and 900 ^{o}C were totally opaque and easily collapsed. **Figure 3.4 (b)** shows the absorption spectra of the water quenched target glass after various heat treatment temperature.

NBS-Ni(WQ) showed sequential spectral change as the heat-treatment temperature increased. The most significant peak around 24,000 cm^{-1} shifted to lower wavenumber side with the heat-treatment temperature. **NABS-Ni(WQ)** showed no peak shift irrespective of the heat-treatment temperature with less visible color change in **Figure 3.4 (a)**. The **NABS-Ni(WQ)** samples showed high inhomogeneity in macroscale including transparent part and opaque part randomly distributed, which can visually observed. The measurement on **NABS-Ni**(1000°C-**WQ**) glass was practiced selectively on transparent part.

The strongest band n_1 located around 24000 cm^{-1} shifted to lower energy side and its intensity grew as treatment temperature increased, as the band position plotted against treatment temperature in **Figure 3.4 (c)**. **NBS-0.8NiO** had main absorption band at higher position at lower temperature. Its position gradually shifted towards to lower wavenumber and shows similar peak position as **NABS-0.8NiO** as getting closer to 1000°C-WQ. Doublet band around n_2 also shifted to lower energy side with modifying its shape into single band. n_3 band, which is strongly related to laser absorption, stayed at constant wavenumber, independent of temperature before water quenching. Assignment of absorption bands in visible region can be done based on the electronic state diagram of TM ion. Since Ni^{2+} has d^8 electron configuration, the ground state corresponds to ^3F state. ^3F and higher levels of ^1D and ^3P in free ion separate into several states depending on strength of ligand field mainly generated by first coordination atoms in condensed system. From absorption spectra obtained in this work, there is no contribution of Td coordination states. 5 coordinated states of square pyramid (SP; C_{4v}) and trigonal bipyramid (TBP; D_{3h}) should be taken into account as the most intense bands at slightly lower energy range in addition to octahedral (Oh) coordination. So the shifting toward lower energy of main band ν_1 seems to be due to the coordination change from 6 to 5.

In **Figure 3.5,** absorption spectra were fitted with several Gaussian functions,

considering coexistence of Oh and SP, with absence of Td originated absorption. Fitted functions could be attributed to respective configuration based on similar absorption energy value in reference sample[106][114][115]. **Table 3.1** summarizes the band parameters. AM sample contains the largest contribution of bands due to Oh symmetry. Absorption of Ni^{2+} in SP symmetry also contributes to the AM spectrum and became larger with increasing heat treatment temperature before water quenching. Main band ν_1 shifted to lower energy side apparently due to the increase of the bands SP_1 and SP_2 ($^3B_1 \rightarrow {}^3E$ transition). Increasing SP_3 accompanied with remarkable change in spectral shape of doublet band, ν_2, because SP_3 shifted to lower energy side with increasing temperature while Oh_2 and Oh_3 did not shift and decreased in their intensities. Oh_4 and SP_4 would give same peak positions insensitive to the heat-treatment temperature. Finally, Peaks area of Oh_1 reduced to 4/9 and SP_1 increased almost twice.

Ni^{2+} in oxide glasses has been extensively investigated. Compared with the previous report of NiO absorption in other glass systems[116][117], the peak position of bands O_{h1}: $^3T_{2g}(F) \leftarrow {}^3A_{2g}$, O_{h2}: $^3T_{1g}(F) \leftarrow {}^3A_{2g}$, O_{h3}: $^1E\ (D) \leftarrow {}^3A_{2g}$, O_{h4}: $^3T_{1g}(P) \leftarrow {}^3A_{2g}$ can be expressed using optical parameter *Dq* and *B* as followings [118]:

$$O_{h4} = 10Dq \tag{3.1}$$

$$O_{h2} = 15Dq + 7.5B - 0.5(225B^2 + 100Dq^2 + 180DqB)^{\frac{1}{2}} \tag{3.2}$$

$$O_{h1} = 15Dq + 7.5B + 0.5(225B^2 + 100Dq^2 + 180DqB)^{\frac{1}{2}} \tag{3.3}$$

From the relationships above, Racah (inter-electronic repulsion) parameter *B* in Oh symmetry was obtained using the peak position of Oh_1, Oh_2 and Oh_4 with following equation:

$$B(\text{Racha}) = \frac{(O_{h1} + O_{h2}) - 3\,O_{h4}}{15} \tag{3.4}$$

Obtained *Dq* and *B* (Racha) were also shown in Table 2. Since Oh_4 band was insensitive to the heat treatment, the same *Dq* was given to all sample. On the other hand, Oh_1 and Oh_2 were weakly sensitive, and *B*(Racha) decreased with increasing temperature before quenching, indicating the decrease of ionicity of interaction between Ni-O. When Ni^{2+} is totally free from ligand field, B_{free}= 1080 cm^{-1}, and the *B* value decreases as covalency of Ni-O interaction increases. However, *Dq*/*B*(Racha) value increased from AM to WQ samples by only 1.7%. The effect of the heat treatment on Ni^{2+} in Oh symmetry is very small. This small change of covalency of Ni-O is also

consistent with very small shift of peak positions of SPi (i=1,2,3,4), which are sensitive to *Dq*. The spectral change due to the heat-treatment temperature does not reflect the change of symmetricity of Oh, but balance between Oh and SP coordinated Ni^{2+} existence.

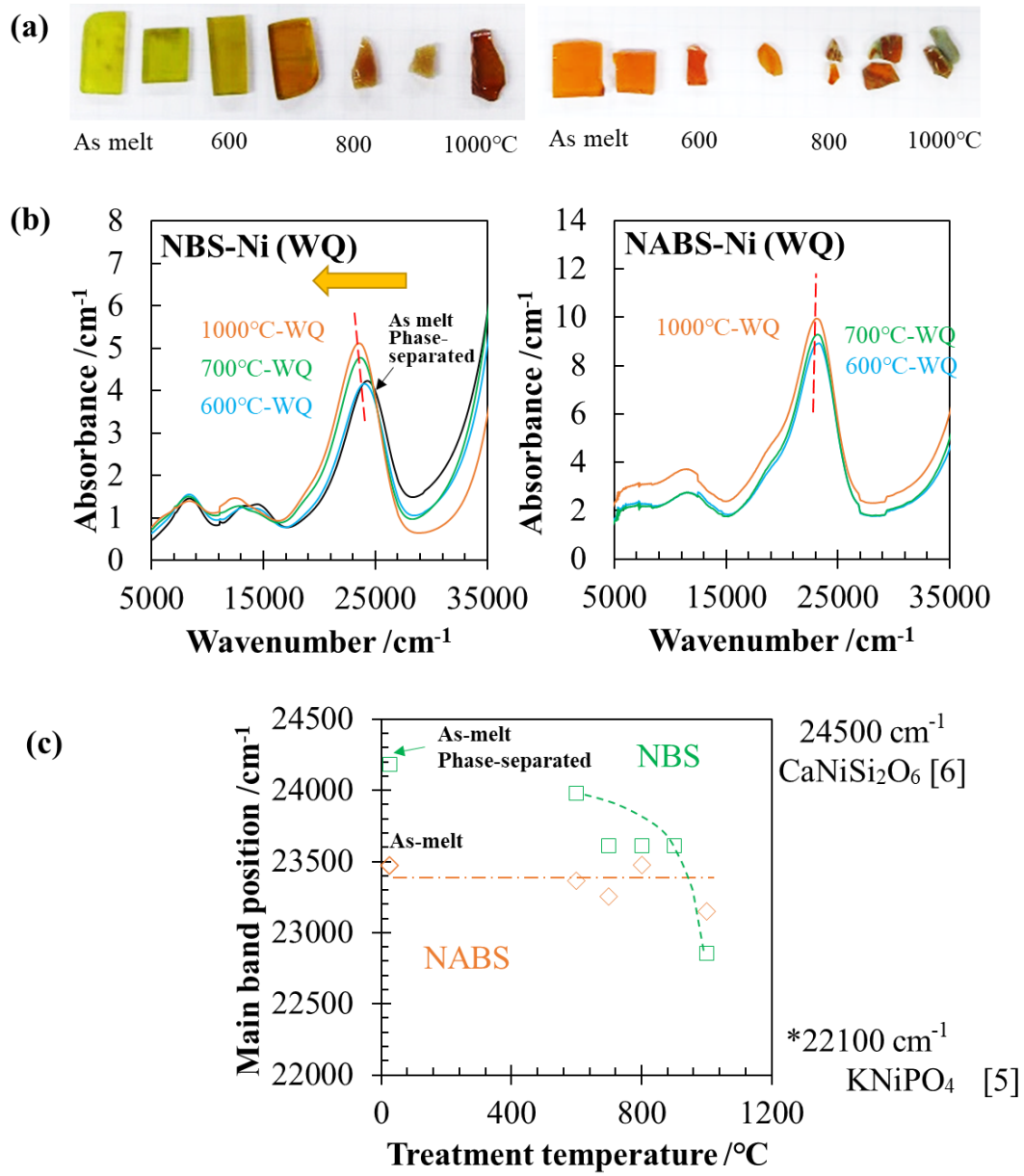

Figure 3.4 (a) Outlook of the glass pieces with various heat treatment temperatures before water quenching. Sample thickness was about 2~3 mm. (b) Absorption coefficient spectra of 0.8 mol% NiO bearing borosilicate (NBS) and aluminoborosilicate (NABS) glass with various heat treatment temperatures before water quenching. (c) Peak position of main absorption band. (d) Absorption spectra in visible region fitted with several Gaussian functions.

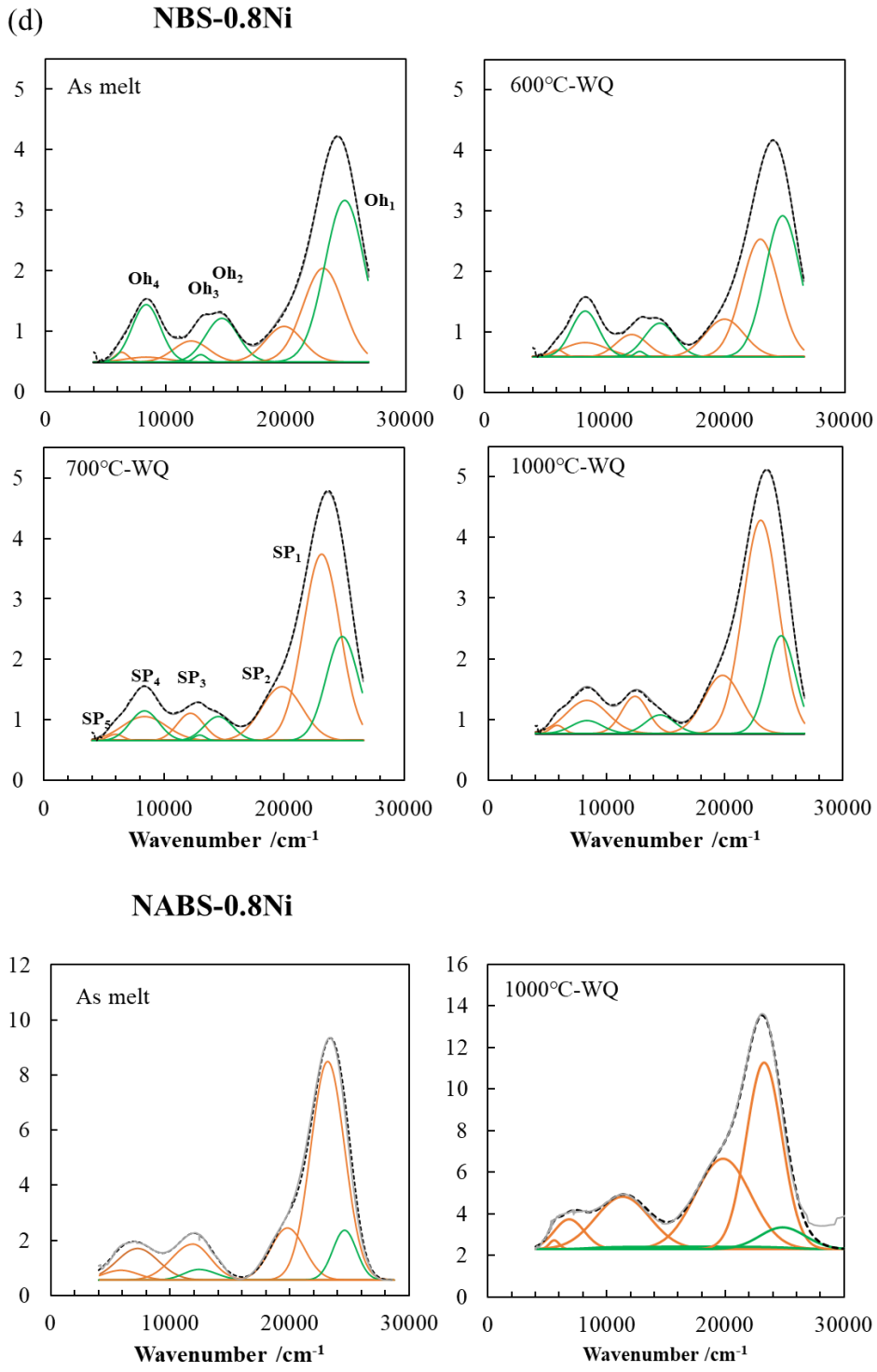

Figure 3.5 UV-vis absorption spectra with peak deconvolution based on absorption band of d-d transition of Ni^{2+} ion in square pyramid (SP, plotted in orange) and octahedral (Oh, green)

Table 3.1 Assignment of absorption band as octahedral coordination of 0.8 mol% NiO NBS glass with various heat treatment temperatures before water-quenching. Calculation of Dq and B for spectra assigned to 5 coordination *SP* is derived assuming similar electronic state to *Oh*. Data of the reference values are from L. Galoisy et al (1993)[114]

	Oh_1	SP_1	SP_2	Oh_2	Oh_3	SP_3	Oh_4(fix)	SP_4	SP_5	Dq	B	Dq/B
$^3A_{2g} \Rightarrow$	$^3T_{1g}$(P)			$^3T_{1g}$(F)	^1E(D)		$^3T_{2g}$(F)					
$^3B_1 \Rightarrow$	^3E	^3E	^3E			^3E		$^3B_2$	$^3A_2$			
AM	24,880	23,100	19,832	14,660	12,900	12,100	8,360	8360	6,300	836	964	0.867
Area %	37.9	25.0	8.9	9.6	0.6	5.0	1.5	10.8	0.8			
600°C-WQ	24,830	22,970	19,980	14,590	12,900	12,240	8,360	8360	6,030	836	965	0.874
	31.6	31.0	10.5	7.3	0.4	5.1	4.3	9.1	0.7			
700°C-WQ	24,860	23,100	19,820	14,520	12,960	12,190	8,360	8,360	5,930	836	953	0.877
	19.4	43.7	14.3	4.4	0.4	4.7	6.8	5.6	0.7			
1000°C-WQ	24,760	23,030	19,810	14,540	12,900	12410	8,360	8,360	5,839	836	948	0.882
	16.8	47.9	13.9	3.4	0.0	6.2	8.7	2.6	0.7			
$KNiPO_4$ [5]*		22,000	18,000				-	8,300	4,800	830	527	1.58
$CaNiSi_2O_6$ [6]*	24,450	-	-	14,900		-	8,200	-	-	820	983	0.834

3.3.3 RT-XAFS spectra of water-quenched glasses

Figure 3.6 (a) shows results of RT-XAFS spectra of water quenched (**WQ**) samples in order to compare two different compositions **NBS-Ni(WQ)** (solid lines) and **NABS-Ni(WQ)** (dotted lines) which were heat-treated at same temperatures before water-quenching. The edge jump of **NBS-Ni(WQ)** was always higher than those of **NABS-Ni(WQ)** and a clear small peak was found at 3861 eV in **NBS-Ni(WQ)**. Exceptionally, **NBS-Ni(**1000°C-**WQ)** and **NABS-Ni(**1000°C-**WQ)** absorption spectra were very similar even though certain amount of Al_2O_3 was contained in **NABS-Ni** glass.

The k^2 weighted spectra in the range of $3< k <9.5$ was processed with Hanning window. The two significant peaks were observed within all spectra. As a reference, the spectrum of NiO crystal (6-coordinated) is plotted on the top with black line, and the spectra from high temperature measurement is plotted below. The most significant peak near 1.4 Å indicates correlation between nickel and ligand oxygen (Ni-O). The peak around 2.6 Å indicates correlation between target nickel and the atoms in second coordination shell. NiO is cubic crystal consist of Ni^{2+} and O^{2-}, so coordination number of second neighbor is 12. The target glass had noticeable peak due to scattering from second neighbors, especially below 800°C.

By fitting the EXAFS signal by equation below, EXAFS parameters were derived for every temperature. All fitting parameter results are calculated with ${S_0}^2 = 1$.

$$\chi(k) = {S_0}^2 \left\{ \begin{array}{c} \dfrac{N_{\mathrm{O}}}{k{R_{\mathrm{O}}}^2} \exp(-2{\sigma_{\mathrm{O}}}^2 k^2) \sin\left(2kR_0 - \dfrac{4}{3}C_3 k^3\right) \\ + \dfrac{N_{\mathrm{Ni}}}{k{R_{\mathrm{Ni}}}^2} \exp(-2{\sigma_{\mathrm{Ni}}}^2 k^2) \sin(2kR_{\mathrm{Ni}}) \end{array} \right\} \tag{3.5}$$

where S_0 is the attenuation factor, N_i $(i = \mathrm{O}, \mathrm{Ni})$ is the coordination number, R_i is the atomic distance, ${\sigma_i}^2$ is Debye Waller factor, and C_3 is the coefficient of third cumulant. Two different path was used to fit two significant peaks explained above. The initial value of the parameters was taken after single scattered path from oxygen ($R_{eff} =$ 2.084 Å) and nickel ($R_{eff} = 2.947$ Å) in NiO crystal. C_3 is considered to be indicating the anharmonicity of potential[119].

The fitting results of RT-EXAFS signals are shown in **Table 2.2**. The obtained CNO was plotted in **Figure 3.11** by small open marks with those obtained by HT-XAFS on **NBS-Ni**. **NBS-Ni** (1000°C-**WQ)** sample at RT has CNO~4. 600°C-**WQ** sample has almost same CNO and Ni-O distance as those of **As-melt** sample, because WQ samples were heat-treated using **As-melt** sample, and low temperature treatment still contained

the effect of thermal history of **As-melt** glass. However, higher-temperature treatment than 800 °C is free from the effect of As-melt, showing higher scattering intensity over whole k-range. Details are shown in **section 3.3**.

With increasing the heat-treatment temperature, CNO gradually decreased below CNO=3.5, which was almost same as CNO of **HT-XAFS** measurement. On the other hand, CNO of **NABS-Ni(WQ)** samples showed almost constant CNO around 3.5 with any heat-treatment temperature. Addition of Al_2O_3 is known to decrease phase separation tendency. Ni^{2+} in this glass has low CNO irrespective of thermal history. There was very similar temperature dependence between peak shift of UV-vis main band plotted in **Figure 3.4 (c)** and CNO from RT-EXAFS (**Figure 3.11)** against the heat-treatment temperature in **NBS-Ni(WQ)** and **NABS-Ni(WQ)** samples.

Interatomic distance of Ni-O of **WQ** samples are also plotted. Ni-O distance of **NBS-Ni(WQ)** showed a slight increase with the heat-treatment temperature up to 800° C, and dopped to lower value to that **NABS-Ni(WQ)** samples had. **NABS-Ni(WQ)** also showed constant low Ni-O distance, and longer than those of **NBS-Ni**(1000 and 1200 °C) of HT-XAFS.

Ni-Ni correlation was also observed at **NBS-Ni**(600 and 800 °C-**WQ**) samples. Ni coordination number in second shell was high as much as those obtained from HT-XFAS analysis. Agglomeration of Ni^{2+} ions in this temperature region are also suggested in WQ samples.

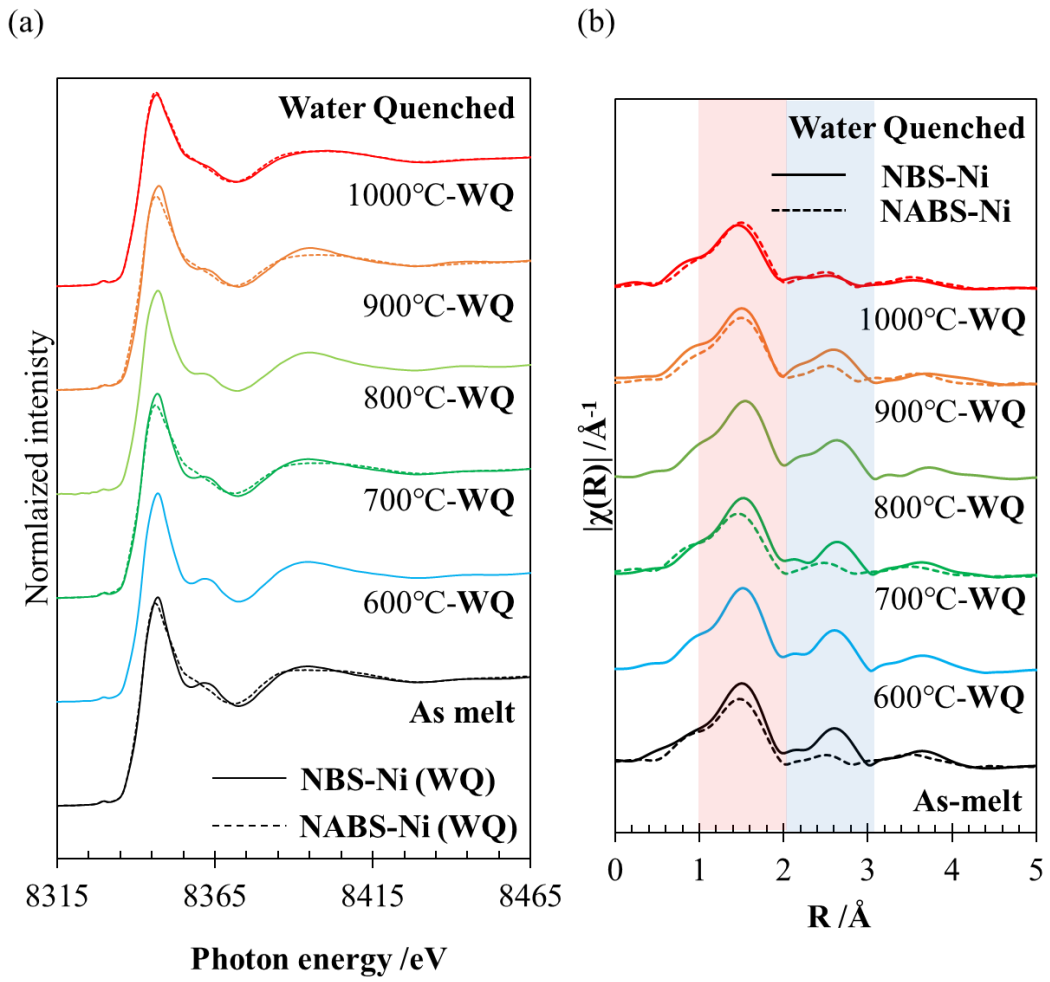

Figure 3.6 (a) XANES spectra of water-quenched samples after 20 minutes heat treatment at each temperature. (b) R-space plot of high temperature in-situ measured XAFS signals, after Fourier transformation on k^2-weighted k-space plot (3<k<9.5) with Hanning window.

3.3.4 Ni-K edge XAFS measurement in borosilicate glass and melt

Figure 3.7 shows the Ni K-edge HT-XAFS spectra obtained from high temperature in-situ measurement, with those of crystals at room temperature, whose coordination number of first coordination shell is known. All the spectra were normalized using the base line drawn for the energy range below the absorption edge and that well above it. The acquisition time of each spectrum of HT-XAFS was 45 minutes following 20 minutes waiting time after the temperature reached the intended temperature. Below 800°C, the absorption spectra were much more similar to crystalline reference with 5 and 6 oxygen coordinated Ni^{2+}, with higher jump at absorption edge at 8331 eV and distinctive signals at following energy values, around 8362 eV. Significant spectral change was observed between 800 ºC and 1000 °C; the edge jump height (Δμt) became lower by 25~30% compared to those of the spectra collected at 600~800 °C; Δμt ≈1.0±0.01 for spectra below 800 °C and 0.7±0.06 for above 1000 °C in average. The reference spectrum of 4 oxygen coordinated crystal has a lower edge jump similar to that at 1000 °C.

The pre-edge peak around 8328 eV was enlarged in **Figure 3.8**, here the peak intensity was converted to molar absorption coefficient ε (L/mol·cm) using the sample thickness *t* and Ni concentration in glass. Considering total absorption μ(E)*d* from XAFS signal (after substruction of the baseline drawn below absorption edge),

$$\varepsilon = \mu(E) \times M/(w_{\mathrm{Ni}} \times \rho \times 10^3 \times d) \tag{3.7}$$

where M is atomic weight of Ni [g/mol], w_{Ni} is weight proportion of Nickel atoms in glass, ρ is density [g/cm^3], and d is actual thickness of the sample[cm]. The density at room temperature is 2.22 g/cm^3. When the temperature increases, the volume of glass expands; ρ decreases and d increases. The glass sample was held in a small Pt cylinder with internal diameter of 2 mm and thickness *d*. This means that the cross term of ρd cancels the decrease of ρ and increase of *d*, so RT data can be used for ρd term in the denominator of equation (3.2). Pre-edge peak indicates the transition 1s→3d which is spin-forbidden electron transition[120], so increase of its intensity reflects the symmetricity of ligand field. **Figure 3.8** summarized the pre-edge peaks of **NBS-Ni(HT)**, **NBS-Ni(WQ)** and **NABS-Ni(WQ)**. As the references, the pre-edge peaks of standard crystals are shown in **Figure 3.8 (b)** where the peak intensity was not converted into molar absorption coefficient strictly. From these, the pre-edge peak

intensity varied much depending on the glass composition and measurement condition of temperature. **NBS-Ni(HT)** spectra showed intense and strong dependence on the condition, measurement temperature. At high temperature above 1000 °C, the pre-edge peak was intensified significantly, and showed the most intense peak at 1000 °C. At the ambient measurements on the water-quenched samples, **NBS-Ni(WQ)** and **NABS-Ni(WQ)**, the relatively low pre-edge peaks were observed. However, heat-treatment temperature dependence was stronger in **NABS-Ni(WQ)** than in **NBS-Ni(WQ)**. As found in the reference spectra **Figure 3.8 (b)**, pre-edge peak intensity is strongly dependent on the coordination number. The spin-forbidden transition of Ni^{2+} in glass reflected the surrounding coordination (the number and types of oxygens) and dynamics (at high temperature). **Figure 3.8 (c)** plotted the peak height against the measurement temperatures for **NBS-Ni(HT)** and the heat-treatment temperatures for **NBS-Ni(WQ)** or **NABS-Ni(WQ)**. Changes due to the temperature is clearly significant in **NBS-Ni(HT)** samples. The dependences of peak height and peak position of the pre-edge peak of **WQ** samples on the heat-treatment temperature are also plotted in **Figure3.8 (b)** and **(c)**. Compared with the pre-edge peaks of high temperature measurement in **Figure 3.8 (a),** those of WQ samples varied quite small.

Figure 3.9 shows Fourier transform of respective spectra measured at different temperature. The obtained fitting parameters for HT-EXAFS are given in Table 1 and their temperature dependences are plotted in **Figure 3.10.** The effect of C_3 become significant at elevated temperature and severely affect the result of atomic distance. C_3 was applied to the first coordination shell. Coordination number of ligand oxygen(CNO) was closed to 4 in **NBS-0.8NiO**(1000°C-**WQ**) at room temperature, and increased to 5 with temperature above the glass transition temperature up to 800 °C. For in-situ measured 1000°C and 1200°C, there were two different possible fitting results, as plotter by rectangle (CNO≈4) and triangle (CNO≈2). Those two fitting results have similar atomic distance and C_3, but lower Debye Waller factor for CNO≈2. In both cases, CNO showed rapid decrease from 800°C to 1000°C. Very similar temperature dependence was observed in the trend of the atomic distance Ni-O. The decrease of atomic distance was consistent with shorter atomic distance in 4-coordinated crystal compared to in 6-coordinated one [120][106]. Debye Waller factor shows thermal and structural disorder via decay of the amplitude of EXAFS oscillation as wavenumber increase in *k*-space. The fitting results showed the gradual increase of this factor above the glass transition temperature region. For fitting results with CNO≈4, Debye Waller factor of the first coordination increased up to 1000°C and kept similar value at 1200°C. On the other hand, fitting with CNO≈2 showed decrease of the Debye Waller factor

above 1000°C. It may seem unreasonable if Debye Waller factor only indicates thermal disorder, though **NBS-0.8NiO** showed decrease of the factor by increasing the treatment temperature from 800°C-WQ to 1000°C-WQ. Considering **NABS-0.8NiO** showed similar Debye Waller factor as **NBS-0.8NiO** 1000°C-WQ for all heat treatment temperature, lower CNO may have lower Debye Waller factor as structural disorder. Those results will be further discussed at Discussion.

Third cumulant C_3 also increased along with temperature, taking highest value at 1200°C. Above two fitting parameters related to temperature condition developed as temperature increased. The second peaks in *R*-space were also fitted without C_3 as in equation (3.2). As shown by the significance of the peak in *R*-space in Figure (a), the coordination number in second coordination shell increased by 800 °C, but peak itself became less significant above 1000 °C. For simplification, the second coordination shell was assumed to be consisting of Ni ion only, the number of Ni^{2+} ion increased up to 8 in second shell at 800 °C, but at 1000 °C, the correlation between Ni^{2+} ions disappeared, and other members (Si, B) came in the second shell.

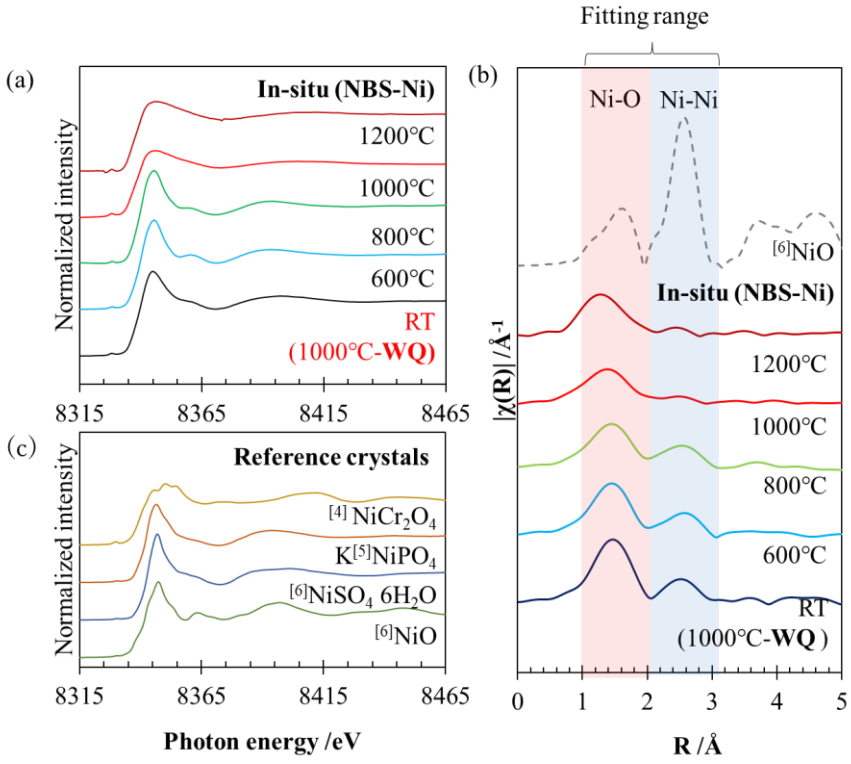

Figure 3.7 (a) XANES spectra and (b) R-space plot of high temperature in-situ measurement at Spring-8, BL19B1. (c)The 4 spectra from reference crystals were measured at room temperature, in BL14B2.

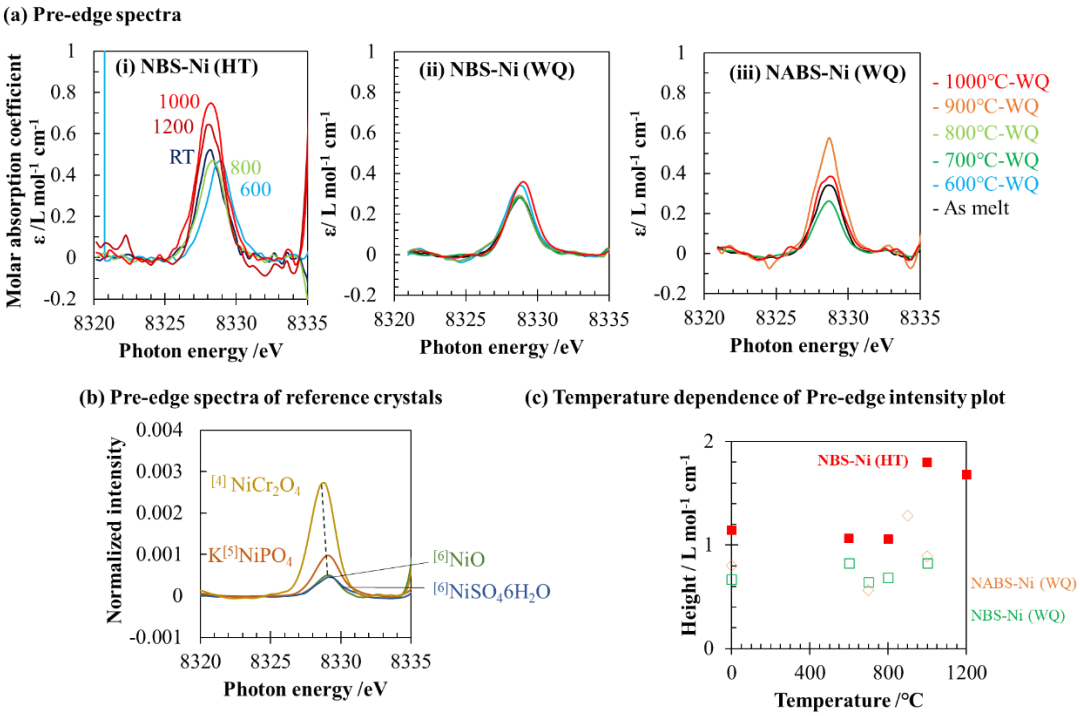

Figure 3.8 Pre-edge peak spectra of (i) NBS-Ni glass measured in high temperature and water-quenched samples after heat treatment at respective temperature (WQ) of (ii) NBS-Ni and (iii) NABS-Ni. Background (Linear + Lorentzian) was subtracted. (b) Temperature dependence of pre-edge peak intensity. Red filled triangle shows HT-NBS, (c) Pre-edge spectra of reference crystals shown in Figure 3.7 (c).

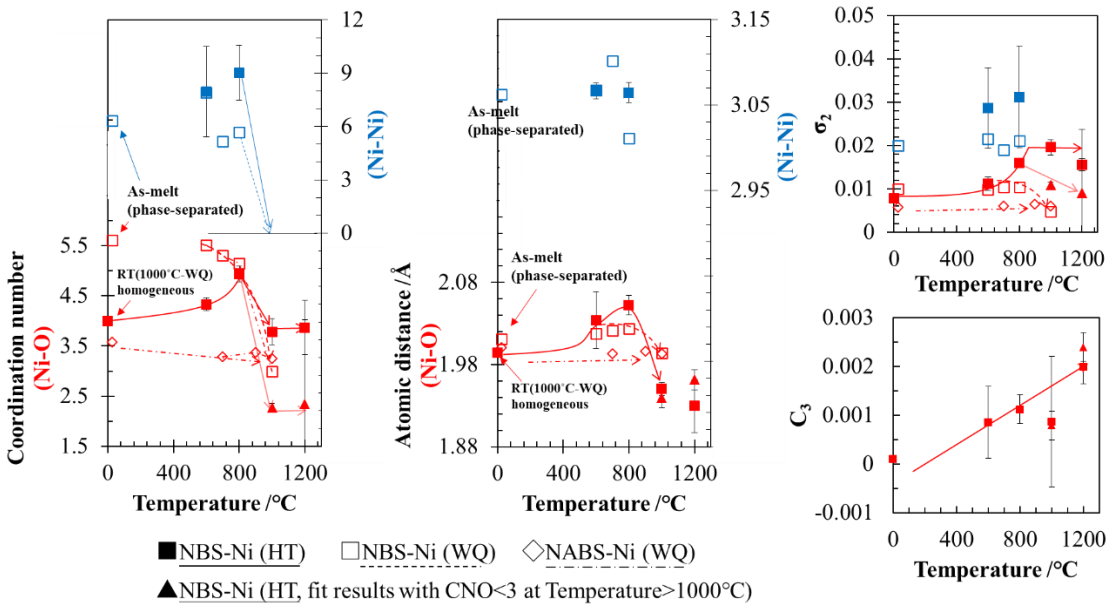

Figure 3.9 Temperature dependence of each fitting parameter. Approximate Tg is plotted with red dot lines, as a start point of characteristic change.

[121]

Table 3.2 Fitting parameters obtained from EXAFS analysis, using function shown in Eq. (3.2).

	CN (O)	Ni-O distance /Å	σ^2 /Å^2	C_3	CN (Ni)	Ni-Ni distance /Å	σ^2 /Å^2
High temperature in-situ (NBS-Ni)							
Room temperature (1000℃-WQ)	4.02	1.993	0.007	0.0001	(1.849)	(2.971)	(0.010)
600℃	4.33	2.034	0.011	0.0009	7.957	3.066	0.029
800℃	4.94	2.052	0.016	0.0011	9.021	3.064	0.031
1000℃	3.79	1.950	0.020	0.0009	(0.148)	(2.897)	(0.004)
1200℃	3.87	1.930	0.016	0.0020	-	-	-
▲1000℃	2.27	1.940	0.011	0.0008	-	-	-
▲1200℃	2.35	1.961	0.009	0.0024	-	-	-
Water-quenched (WQ) samples at room temperature							
NBS-Ni(WQ)							
As melt	5.61	2.011	0.010	-	(6.341)	(3.062)	(0.020)
600℃-WQ	5.50	2.018	0.010	-	7.919	3.068	0.022
700℃-WQ	5.30	2.022	0.011	-	5.151	3.102	0.019
800℃-WQ	5.15	2.024	0.010	-	5.672	3.011	0.021
900℃-WQ	4.70	2.030	0.008	-	8.236	3.051	0.023
1000℃-WQ	4.50	1.994	0.009	-	-	-	-
NABS-Ni(WQ)							
As melt	3.58	2.000	0.006	-	-	-	-
700℃-WQ	3.29	1.994	0.006	-	-	-	-
900℃-WQ	3.37	1.996	0.007	-	-	-	-
1000℃-WQ	3.25	1.994	0.006	-	-	-	-

3.3.5 Ni-K edge XAFS measurement in laser irradiated NBS glass plate

Figure 3.10 (a) shows the K-edge Ni XANES spectra of 0.8 mol% NiO bearing NBS glass with different treatments such as water quenching and laser irradiation with leaching. The first three spectra show the XANES spectra of reference crystals from [106]. The spectra indicating Ni^{2+} in $KNiPO_4$ is 5 coordinated and $NiSO_4 \cdot 6H_2O$ is 6 coordinated. 5 and 6 coordination can hardly distinguish from XANES spectra, with slight peak modification around 8360 eV. The spectra of glasses were apparently similar except a shallow peak around 8360 eV, highlighted with a dotted line. After laser irradiation, this peak became flat. Comparing AM and PS (580 ℃, 4h) samples, the PS sample showed more clear shoulder around 8360 eV. The samples water-quenched from high temperature (1000℃-WQ) showed further flattened peak compared to AM sample. This difference indicates the Ni^{2+} coordination modification by phase separation progress. The laser was irradiated on PS samples and the XANES spectra were measured after leaching, so XAFS signals of Ni^{2+} exclusively in laser-irradiated part could be collected. The spectrum of sample irradiated with 1.0 mm/s showed smoothening of the shoulder at 8360 eV.

Figure 3.10 (b) shows Fourier transforms of respective samples. Observed peaks indicate the correlation between center Ni^{2+} ion and other elements. The first strongest peak at 1.5 Å is attributed to the correlation with oxygen atoms which are forming ligand field around center Ni^{2+} ion. The second neighbor peak showed unique variation for each sample. As noticed in **Figure 3.10 (b)**, AM and PS was showing distinctive Ni-Ni correlation. This Ni-Ni correlation was observed in the laser-irradiated sample with 0.1 mm/s. On the other hand, sample water-quenched from high temperature (>1000 ℃) and laser-irradiated sample with 1.0 mm/s showed Ni-B correlation in second neighbor.

Approximate coordination number can be obtained by EXAFS analysis. **Table 3** shows the EXAFS derived parameters of samples and reference crystals with consistent coordination number[106]. Compared to AM and PS glasses, both coordination number (CN) and Ni-O distance are lower in the WQ samples. The laser irradiated samples also showed decrease in CN and Ni-O distance, indicating similar Ni^{2+} local environment with WQ sample.

EXAFS results from laser-irradiated area show average Ni^{2+} state of laser affected area with high etching durability (Spot size of x-ray was 1 mm x 3 mm). Under existence of several Ni^{2+} coordination states, EXAFS detects the average coordination number considering abundance ratio [107]. So Ni^{2+} in laser irradiated area possibly consist of either average CN everywhere, or much lower CN in heating center and

higher CN in surrounding of the laser irradiated area.

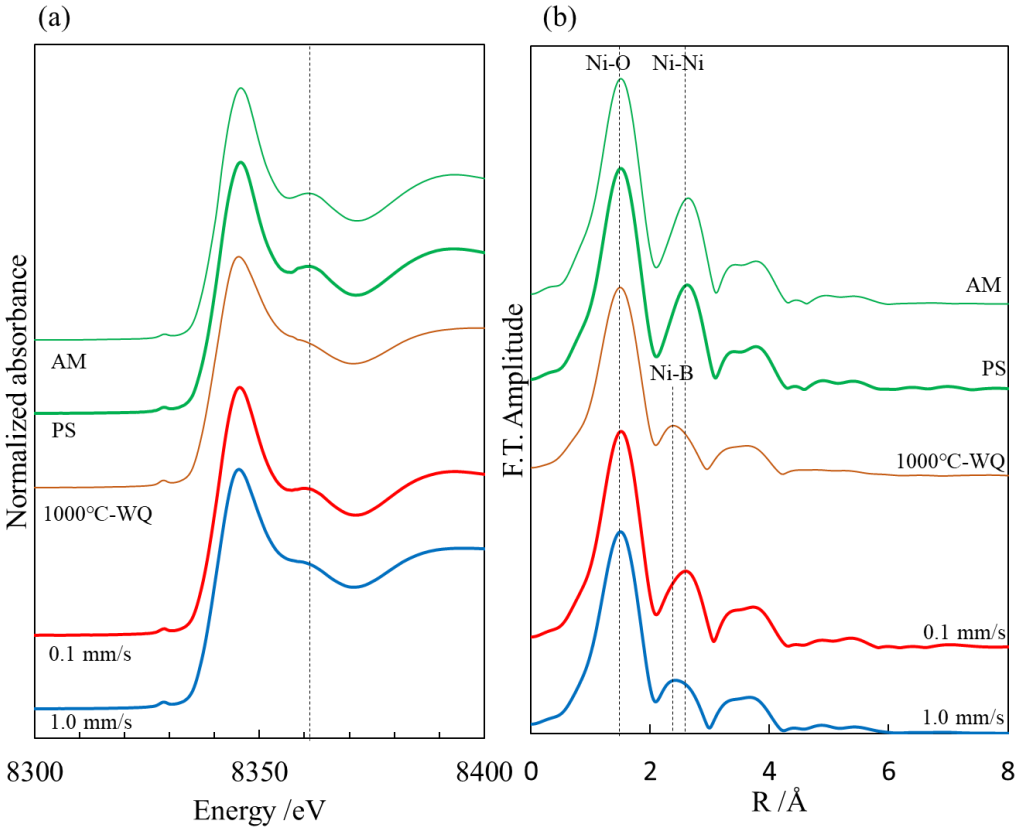

Figure 3.10 (a) XAFS spectra of NBS-0.8NiO after various heat treatment including water-quenching from 1000℃ and laser scanning. (b) R-space plot of XAFS signals, after Fourier transformation on k2-weighted k-space plot.

Table 3.3 Ni K-edge EXAFS derived parameters by fitting 1<r<3 (Å) region of **Figure 3.10 (b)**.

	CN (O)	Ni-O distance /Å	σ^2 /Å^2	CN (Ni)	Ni-Ni distance /Å	σ^2 /Å^2
AM	5.56	2.0034	0.0103	4.99	3.0862	0.01643
1000°C-WQ	4.18	1.9923	0.0091	-	-	-
6W 0.1 mm/s leached	5.22	2.0099	0.0098	3.07	3.0469	0.0157
6W 1.0 mm/s leached	4.60	1.9987	0.0092	1.265	3.0458	0.0119

3.4 Discussion

3.4.1 Homogeneity of phase separating NBS glass and Ni^{2+} environment

From previous report[122][123], transition metal ions such as Ni^{2+} are mostly distributed in B_2O_3 rich phase and does not remain in SiO_2 rich phase. It can also be confirmed by loss of Ni^{2+} after leaching of PS sample. Since Ni^{2+} is highly sensitive to composition or optical basicity of glass, various parameters that change absorption of Ni^{2+} ions had been reported [106][124][125][126][127]. Considering that end-member composition of each phase depends on heat treatment temperature[128], Ni^{2+} coordination in phase separated glass will reflect structural information of borate rich phase which may be even smaller than nanoscale. Local environment of Ni^{2+} ion can be one of the indicators of homogeneity in NBS glass, as borate rich phase disappears in total homogeneous borosilicate glass.

The target glass shows strong tendency on phase separation, which even shows high opacity when water-quenched after treatment even at 900 ℃. NBS glass with high phase-separation tendency is difficult to control its homogeneity in nanoscale. Even when the certain melt is rapidly quenched using steel twin-roller (-10^6 K/s), it still shows spinodal decomposition[24]. Although, sample which was quenched by water (~-50 K/s)[129] soon after heat treatment at 1000 ℃ showed distinctive color change from green to brown, and no reduction of NiO after acid leaching, which indicates Ni^{2+} presence in chemically durable phase such as homogeneous borosilicate, or phase containing silicate network.

3.4.2 Ni^{2+} coordination analysis

The coordination state of Ni^{2+} is sensitive to ligand field which changes its color depending on host glass structure[53]. Depending on field strength given by electron donating ligands next to transition metal, five-fold degenerated ground state of d-orbital split into several states for further stability. In the case of common field strength *Dq*, 6 coordinated neighbors (electron donating ligand; oxygen atoms in oxide glass) with octahedral structure shows higher Ligand Field Stabilization Energy ($LFSE_{Oh}=12Dq$), compared to 4 coordinated with tetrahedral structure ($LFSE_{Td}=10Dq$). Each of the scture shows different band energy dependence on absorbance due to respective energy splitting behavior and symmetricity of configuration. As intermediate state between octahedral and tetrahedral configuration; 5 coordination in trigonal-bipyramid D_{3h} or square pyramid C_{4v} shape can be found and it also shows different specification [114][115]. Besides apparent high stability of octahedral site, nickel divalent ion were

found in tetrahedral site in some cases.

The ligand field strength around TM ion in glass matrix is affected by several factors: composition, temperature and nano-scale inhomogeneity. The strength of field generated by ligand oxygens is mainly affected by composition, especially by nature and amount of alkali and alkaline ions, which have characteristic cationic field depending on its size and charge [116][53][130]. In the case of oxide glass, average electron donor ability of whole glass network can be evaluated by theoretical optical basicity Λ_{th}. Average optical basicity of the glass matrices was defined by Duffy and Ingram[131][132] to evaluate the electron donating ability of anions. Average optical basicity of the glass matrix can be calculated from composition as additive property, so it is a useful way to evaluate the field strength with different composition.

Octahedral sites are often found in host glass matrices with low electron-donation ability, which is often evaluated as having low optical basicity. As plotted in **Figure 3.11 (a)**, coordination number of Ni^{2+} shows correlation to optical basicity. Borate glasses tend to have low optical basicity compared to silicate glasses, though its basicity increases with increasing amount of alkali content [109]. Silicate glass is plotted among CN=4~5 and does not show octahedral sites [120][107]. Aluminosilicate glass with various nature of alkali/ alkaline earth cation [106] had high optical basicity with low coordination number, varying depending on its cation field strength. Considering potentially existing error in EXAFS analysis, it may be difficult to compare absolute value of coordination number obtained from different XAFS measurement and fitting procedure. Still, most of the results are consistent with configuration analysis by optical absorption spectra of d-d transition. There was inversed linear correlation between optical basicity and Ni^{2+} coordination number.

As shown in **Figure 3.11 (a)**, theoretical optical basicity of the sodium borosilicate glass in this study is 0.451. The expected optical basicity change considering compositional transition due to phase separation is not enough to earn distinctive basicity change. (SiO_2: 0.443, 6.8 Na_2O - 31.1 B_2O_3: 0.458). Such a coordination number variation within same glass composition had not been observed. Ni^{2+} in homogenization of phase separated glass reflected not simply merging of two phases with different compositions.

Considering insignificance of optical basicity change by phase separation, transition of Ni^{2+} ion might be indicating more local environmental reconstruction. Ni^{2+} ion might initiatively pull NBO to ligand in NBS glass with high homogeneity. This effect might particularly be enhanced by strong cation field strength of Ni^{2+}, due to its relatively small atomic radius. In such a case, Ni^{2+} with lower CN would be considered as

network former, as similar effect observed with Mg^{2+}, showing higher bonding covalency with tetrahedral coordination[133][134].

3.4.3 Ni^{2+} as structural probe in phase separated glass

The significant speciation changes of Ni^{2+} ion with different heat treatment were observed in sodium borosilicate (**NBS-Ni**) glass with nanoscale phase immiscibility. On the other hands, there was few speciation change in sodium aluminoborosilicate (**NABS-Ni**) glass, which has homogeneous body in nanoscale, observed by SAXS measurement. In this section we discuss about the origin of speciation change in Ni^{2+} ion and what it indicates in the glass with phase separation.

The relationship between Ni^{2+} speciation and phase immiscibility are clear from the plot of CNO depending on its treatment temperature as shown in **Figure 3.11 (b)** with green open circle for NBS-Ni(WQ). The orange open diamond shows the result from NABS-Ni(WQ) where phase separation is avoided, showing almost constant value independent of treatment temperature. The coordination number tend to be around 4-coordinated when the glass turns to miscible, such as 1000°C and 1200°C melt, 1000°C-WQ of NBS-Ni glass and NABS-Ni glass with any heat treatment temperature. In addition, the size of the phase in NBS-Ni(WQ) glass increased as heat treatment temperature increased. Similarly, coordination number of oxygen CNO in NBS-Ni(WQ) samples decreased with heat treatment temperature increase. CNO of NBS-Ni from in-situ measurement in 600°C, where the scatterer size was still developing from miscible to immiscible, was plotted in between 4-coordinated and 6-coordinated.

When the CNO obtained from laser irradiated area are plotted in **Figure 3.11 (b)**, the degree of immiscibility can be roughly estimated. Both laser-scanned sample with 1.0 mm/s and 0.1 mm/s had CNO value in between miscible and immiscible. The result that faster scanning (1.0 mm/s) showed higher miscibility was consistent with the result from chapter 2. The slower scanning might introduce further heat transfer with gradual cooling, which causes the phase separation development after homogenization by laser exposure.

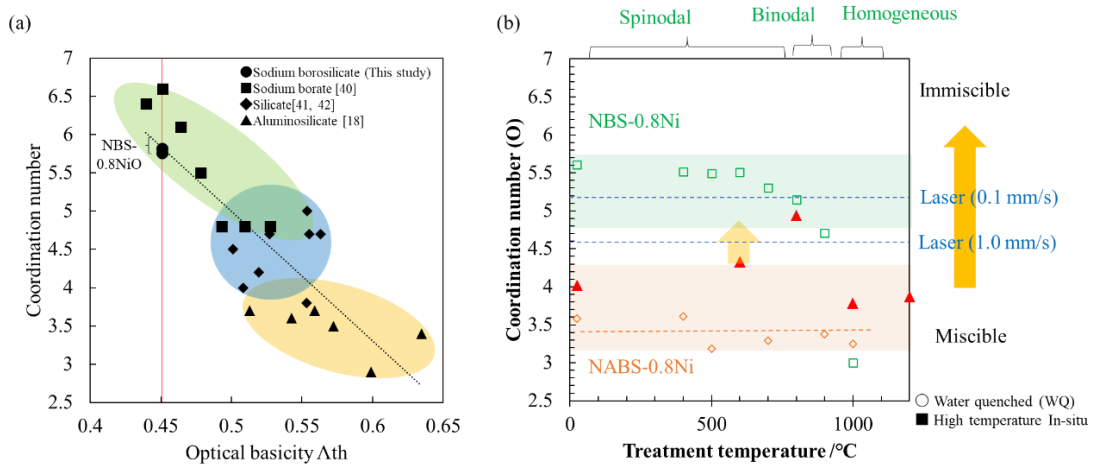

Figure 3.11 (a) R-space plot of XAFS signals, after Fourier transformation on k^2-weighted k-space plot. (b) CNO of NBS-0.8NiO after various heat treatment including water-quenching from 1000℃ and laser scanning, with homogeneous NABS-0.8NiO as reference

3.4.4 Thermal effect on Ni^{2+} ion local environment

XAFS measurement using advantage of a monochromatic high intensity X-ray beam has great benefit on characterizing the elements in materials under extreme condition. Its application to glass under non-ambient condition has been gathering much attention, because the glass structure in nanometer size and larger are dependent on the preparation history and their properties have been controlled based on these knowledges. High temperature measurement, of course, had been focused in several previous reports on glass melts[135][136].Thermal history from melting temperature above liquidus temperature down to the glass transition via super-cooling condition, is the picture of glass forming materials. Phase separation of NBS system proceeds at super-cooling condition below liquidus temperature. Thanks to its very low crystallization tendency, nanometer-size structural modification is possible by controlling temperature and treatment time to which the initial glass or melt is subjected. Phase-separation progress diffusion and resulted structural evolution have been investigated on the quenched samples, but very few by in-situ analysis.

The EXAFS analysis on spectra collected in-situ at high temperature, however, has several difficulties due to two main reasons. One is the treatment of anharmonicity in the interatomic potential appeared at high temperature. At room temperature,

distribution function can be expressed simply by gaussian, because the most of elements are located at the potential minimum formed by the surrounding elements. At high temperature, cumulant should sufficiently describe anharmonicity of potential due to thermal expansion [137]. As shown in Eq.(3.5), C_3 is included in the phase of sine function in *k*-space, together with atomic distance. These two parameters, C_3 and atomic distance, are highly correlated to each other in the fitting procedure. It have been reported that without contribution of C_3 to the temperature dependence, atomic distance does not coincide with the result obtained from high temperature XRD measurement[119]. From high temperature in-situ EXAFS analysis results in **Figure 3.9** and **Table 3.2**, C_3 value increased as temperature increased. Thanks to the introduction of anharmonicity in potential, trends of local environments of Ni^{2+} at high temperature were evaluated well.

Another difficulty is due to low XAFS signal intensity at high temperature. Similar trend is observed in high-temperature or high-pressure measurement independent of focused atomic species [137][107]. From Eq. (1), the signal amplitude is expressed by coordination number, and its decay along with *k* value is expressed by Debye Waller factor σ^2. The effect from these parameters could hardly distinguish when the signals are weak and the phase of *k*-space signals are unclear in high *k*-region, in our case after k=7 $Å^{-1}$. So, it was difficult to validate the fitting result, which is reasonable; CNO=4 with high σ^2 or CNO=2 with relatively low σ^2.

Though there are other two factors which may help to understand coordination of Ni^{2+} ion: pre-edge peak in XAFS spectra and the main band in UV-vis spectra. Pre-edge peak is attributed to transition from 1s orbital to empty 3d orbital, which is quadrupolar and parity forbidden[138]. When d-orbital lose its inversion center by effect of ligand field, the transition is allowed and pre-edge peak start to increase its intensity and shift toward lower energy side[107]. So, it had been probed that both peak intensity and position is reflecting the coordination number of first coordination shell; lower intensity with the shift of peak position to higher energy side for octahedral and higher intensity with the shift of peak position to lower energy side for tetrahedral coordinated [139]. From **Figure 3.8 (c)**, pre-edge peak intensity of 1000°C and 1200°C measured in-situ showed excessive high molar absorbance compared to the results from lower temperature and **WQ** samples. It indicates lower symmetricity in high temperature above 1000°C than other samples showing 4-coordinated such as **NABS-0.8NiO(WQ)** and 1000°C-WQ of **NBS-0.8NiO**. For high temperature in-situ measurement above 1000°C, pre-edge position shifted toward lower energy, indicating low coordination number, similarly, to **NABS-0.8NiO(WQ)** samples. Considering the structural information obtained from

pre-edge peak of XAFS spectra, coordination above 1000°C might show 4-coordinated, but with lower symmetricity of ligand field. The ligand configuration above 1000°C might be highly random or dynamic due to thermal energy, observed as average of few ligand atoms with low symmetricity.

The other factor showing coordination of Ni^{2+} is the peak position of main band in UV-vis region. The several bands extended in UV-vis-NIR region are associated to d-d transition, where the absorption behavior can be explained by ligand field theory. Although UV-vis spectra were not obtained at high temperature in-situ, the results of **WQ** samples will help to understand relationship between coordination number from EXAFS analysis and ligand field configuration from UV-vis spectra. The spectral analysis of **NBS-0.8NiO(WQ)** on UV-vis spectra with ligand field theory is detailed in our previous report [110].

Another difference of two fitting results with different CNO, is Debye Waller factor. The fitting with CNO=4 had higher Debye factor than the results from lower temperature. It might seem unreasonable that fitting with CNO=2 has lower Debye Waller factor at higher temperature, though series of **NBS-0.8NiO(WQ)** also showed decrease of Debye Waller factor as heat treatment temperature increased. It may indicate the dominance of structural disorder, strongly affected by the coordination number. When compared to other reports of Ni K-edge EXAFS signals from Ni containing glasses in ambient condition[120][106], Debye Waller factor was much lower than the results of **NBS-0.8Ni** either for WQ samples and high temperature and in-situ measurement, while **NABS-0.8NiO** showed similar Debye Waller factor as other reports. It may be considered that NBS had several Ni^{2+} ion coordination site due to nanoscale clustering. Since EXAFS data shows the average coordination number when there are several different Ni^{2+} coordination state, with higher Debye Waller factor than single coordination site[107].

Recently, Galoisy et al. reported that 4-coordinated Ni^{2+} ion with planar-square will show specific peak in edge jump and such a feature could not be found in case of alkali borate glass [138]. Considering this fact, the highest pre-edge peak from spectra measured above 1000°C appeared to show relatively higher symmetricity compared to planar square coordination. Still, it is difficult to conclude that CNO=4 above 1000°C, since there is possibility of CNO=2 appeared in tetrahedral coordination. Stability of such a local structure might be low, though it may be accomplished instantaneously and XAFS spectra had been observing the average structure during entire measurement time.

In addition, XANES spectra above 1000°C showed lower $\Delta\mu t$ than that of lower temperature. The similar feature was found with Ni^{2+} ion coordinated by 4 oxygen

atoms[138] or ligand with higher electron donor ability such as S^{2-}[140]. Although, the peak shape of spectra above 1000°C in-situ are totally different from those spectra from reference crystals, with no wrinkle on the edge jump peak. This wrinkle, or dispersive peaks in XANES appear due to existence of several unoccupied orbitals such as conductive material or distorted crystal. Smooth, single wide peak in XANES region may indicate spatial expansion of d-orbital in high temperature.

3.5 Summary

The high-temperature in-situ transformation of phase separation in NiO doped Na_2O-B_2O_3-SiO_2 (**NBS-0.8NiO**) glass could be observed from viewpoint of morphology and composition. The coordination number and atomic distance could be obtained from EXAFS analysis. The signals at high temperature could be obtained clearly by transmission mode XAFS measurement, the thermal effect on XAFS signal was clearly distinguished by fitting procedure. Since Ni^{2+} ion also works as laser absorbent, the light absorption behavior could be estimated considering UV-vis-NIR spectra with similar coordination number at room temperature.

The speciation of Ni^{2+}ion drastically changed along with phase separation development and homogenization, changing its coordination number from 6-coordinated to 4-coordinated. Starting with green coloration in phase separated glass, it turned to brown when the glass turned homogeneous above 1000°C. The Ni^{2+} ion is known to stay selectively in borate rich phase and is sensitive to local environment. Since the optical basicity calculated from oxide glass composition has strong correlation with coordination number of Ni^{2+} surrounded by oxygen, Ni^{2+} ion speciation might reflect composition of surrounding glass matrix changing from borate rich phase to borosilicate phase as temperature increases. The color change of Ni^{2+} containing glass after laser irradiation indicates the mixture of borate rich phase and silica rich phase had maintained at room temperature.

4 Time resolved in-situ observation of dynamic transition behavior of phase miscibility during heat treatment

4.1 Introduction

In chapter 3, the immiscibility due to phase separation in NBS glass was evaluated by speciation change of Ni^{2+} ion. The local environment of Ni^{2+} ion is sensitive to the electron donor ability of ligand oxygen, so temperature dependence of compositional change in respective phases effectively caused the coordination change in Ni^{2+} ion. Although, the morphology such as spinodal / binodal could not be detected and phase separation behavior of NBS-0.4CuO is still unknown.

In this chapter, Small Angle X-ray Scattering was measured to evaluate the detailed nanoscale morphology after various heat treatment, with comparison between several compositions to see the effect of each atomic component. In addition, time-resolved in-situ measurement during heating and cooling process was achieved observing transient behavior toward homogenization during laser heating and development of phase separation in homogeneous glass during cooling process.

4.2 Experimental

4.2.1 Sample preparation

The NBS glasses were prepared by melt-quenching method as explained in chapter 2. These two compositions were suitable for laser processing in chapter 2. For room temperature measurement, water-quenched (**WQ**) samples were fabricated for **NBS-0.4CuO**, **NBS (without additive TM ion), and NBS-0.2NiO** glasses in order to consider the effect of additive TM ions to phase separation behavior. In addition, 0.8 mol% NiO doped NBS glass with different K=SiO_2/B_2O_3 ratio (K=3: 5.2 Na_2O- 23.7 B_2O_3- 71.1 SiO_2 and K=1.5: 8.0 Na_2O- 36.8 B_2O_3- 55.2 SiO_2) were prepared by melt-quenching method and WQ samples were prepared, while the composition of the target glass NBS-0.8NiO has K=2.

For high temperature in-situ measurement, glass pieces with composition of **NBS-0.8NiO** and **NBS-0.4CuO** were embedded in Pt-ring as explained in chapter 3. Two different initial states before in-situ measurement were prepared: 1000°C-WQ and PS (phase separated: after 1000°C-WQ, kept in 580°C for 4 hour and cooled in ambient condition).

4.2.2 High temperature in-situ SAXS measurement.

High temperature in-situ measurement of SAXS spectra with different thermal histories were measured for **NBS-0.8NiO and NBS-0.4CuO** glasses at BL19B2 at

SPring-8. X-ray energy was 18 keV, with the exposure duration time of 1 minute for every measurement with 1 minute interval. Camera length was set as 3 m. The transmittance of X-ray was in the range of 0.68~0.71.

The glass specimen in Pt ring were treated under three different thermal history to obtain initial glass condition with different miscibility before measurement. The temperature profile during measurement was controlled as explained in **Figure 4.1**. Before the heat treatment, glass was cooled down gradually (-1°C/min) from 1000°C to confirm adhesion between Pt zig and the glass sample. The glass pieces were totally greenish opaque at this point (as photo shown in **Figure 4.7**).

The **temperature profile I** is reproduced from high temperature in-situ XAFS measurement in chapter 2. Before the measurement, the glass samples were water-quenched from 1000°C to realize homogeneous state under room temperature (Hereafter represented as ①). In **temperature profile II**, sample was heated up to 1200°C. Two different initial glass states were used to observe homogenization behavior: ① homogeneous (1000°C-WQ) and ② phase separated (580°C for 4 hours and air-cooling). For **NBS-0.8NiO** glass, SAXS spectra were obtained under heat treatment as **temperature profile III** starting with totally opaque state soon after gradual cooling. After reaching 1200°C and hold for 20 minutes, the glass was cooled down to 700°C and hold for 20 minutes. The sample was heated up to 1200°C again.

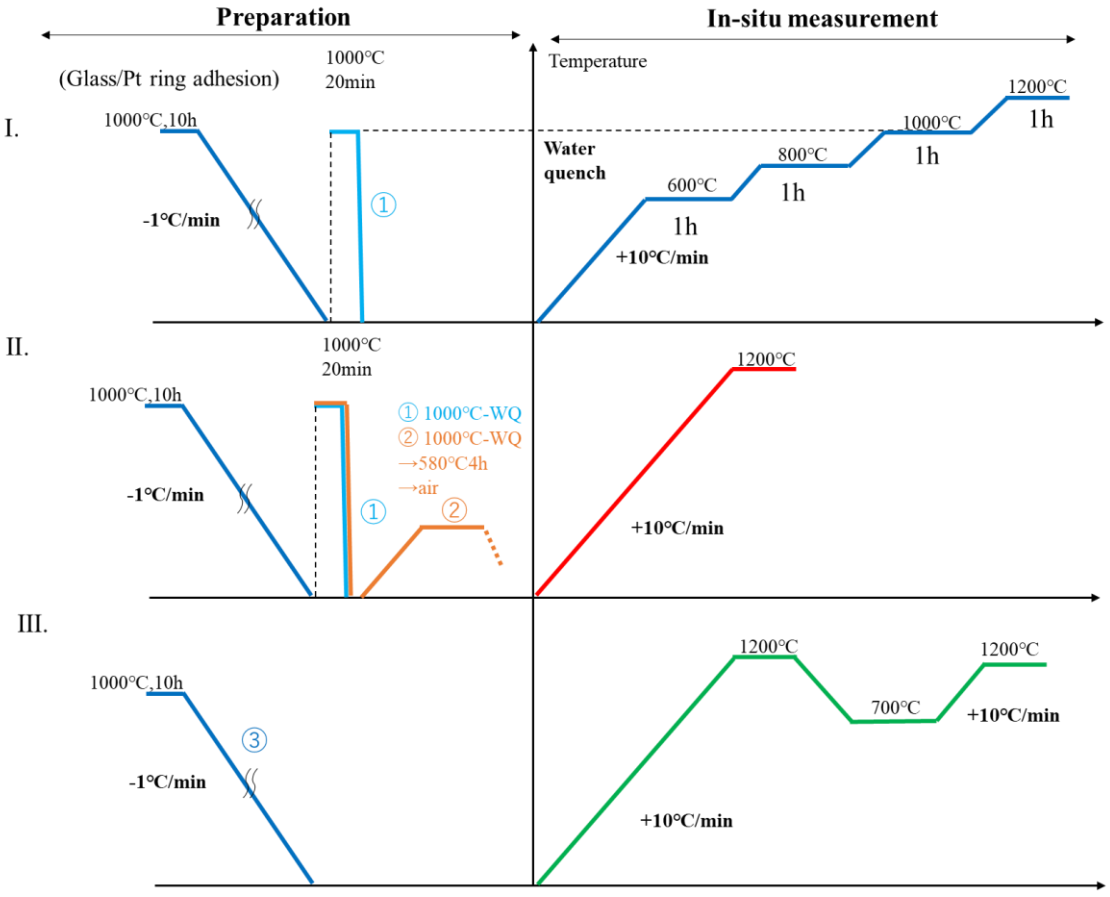

Figure 4.1 Thermal history of time-resolved high temperature in-situ SAXS measurement. The spectra were obtained every two minutes with exposure time of 60 seconds.

I. The same thermal history as high temperature in-situ XAFS measurement. In addition to NBS-0.8NiO, NBS-0.4CuO was measured. (Hold at 600, 800, 1000°C for 1 hour at each temperature,+10°C/min)

II. The sample with two different initial phase miscibility (① Miscible=1000°C-WQ and ② Immiscible) were observed during heated up to 1200°C by +10°C/min.

III. The slowly cooled (-10K/min from 1000°C) NBS-0.8NiO glass was heated up to1200°C and cooled down to 700°C, then again heated up to 1200°C afterward. The difference of homogenization behavior depends on different initial condition.

4.3 Results

4.3.1 Immiscibility of water-quenched glasses with varying compositions

Firstly, the SAXS spectra of WQ samples of NBS-0.8NiO and NBS-0.4CuO were plotted in **Figure 4.2 (a)** and **(b)**. The WQ samples of NBS-0.8NiO showed more distinctive difference depends on heat treatment temperature. Contrary to NBS-0.8NiO which showed significant scattering intensity increase above 800°C, the scattering intensity started to decrease above 800°C in NBS-0.4CuO. The broad peak was observed near 0.3 nm^{-1} and it gradually shifted to higher q-region as treatment temperature increase. It indicates lower homogenization temperature in NBS-0.4CuO than NBS-0.8NiO.

In order to evaluate the effect of additive amount of NiO in NBS glass, WQ samples with NBS-*x*NiO (x=0, 0.2, and 0.8) were compared as plotted in **Figure 4.2 (a)**, **(c)**, and **(d)**. The composition of NBS-0.2NiO and NBS was similar to NBS-0.4CuO, showing decrease of scattering intensity above 800°C. The 800°C-WQ of NBS-0.2NiO showed slight increase of scattering intensity over wide q-range, indicating the increase of NiO might be the cause of binodal formation at 800~900°C. From the results, homogenization of phase separated glass expected to start from lower temperature with glass composition of NBS-0.4CuO. As shown in (e), the WQ samples of NBS-0.8MgO was prepared to compare with NBS-0.8NiO, where NiO in NBS-0.8NiO is substituted to MgO. Since Mg^{2+} ion has similar cation field strength to Ni^{2+} ion, it was expected to observe similar phase separation behavior as NBS-0.8NiO. Although, NBS-0.8MgO showed almost same behavior as NBS without additive ion.

Figure 4.3 shows water-quenched samples with varying SiO_2/B_2O_3 ratio (*K*) heat treated under different temperature before quenching. With highest SiO_2 content (*K*=3), 1000°C-WQ sample showed high scattering intensity at low q-region, with effect of interference among scattering objects indicated by continuous several peaks observed around 0.1 nm^{-1}. Such interference is mainly due to high population of droplet s. On the other hand, 1000°C-WQ samples of composition with lower SiO_2 contents (*K*=2, 1.5) showed low scattering intensity compared to other heat treatment temperature, indicating relatively homogeneous states. In addition, 800°C-WQ and 900°C-WQ sample of *K*=1.5 showed highest scattering intensity similarly to other compositions, though without effect of interference. Overall, higher SiO_2 content contributed to observation of immiscibility at high temperature and higher population of droplet precipitation at 800~900°C.

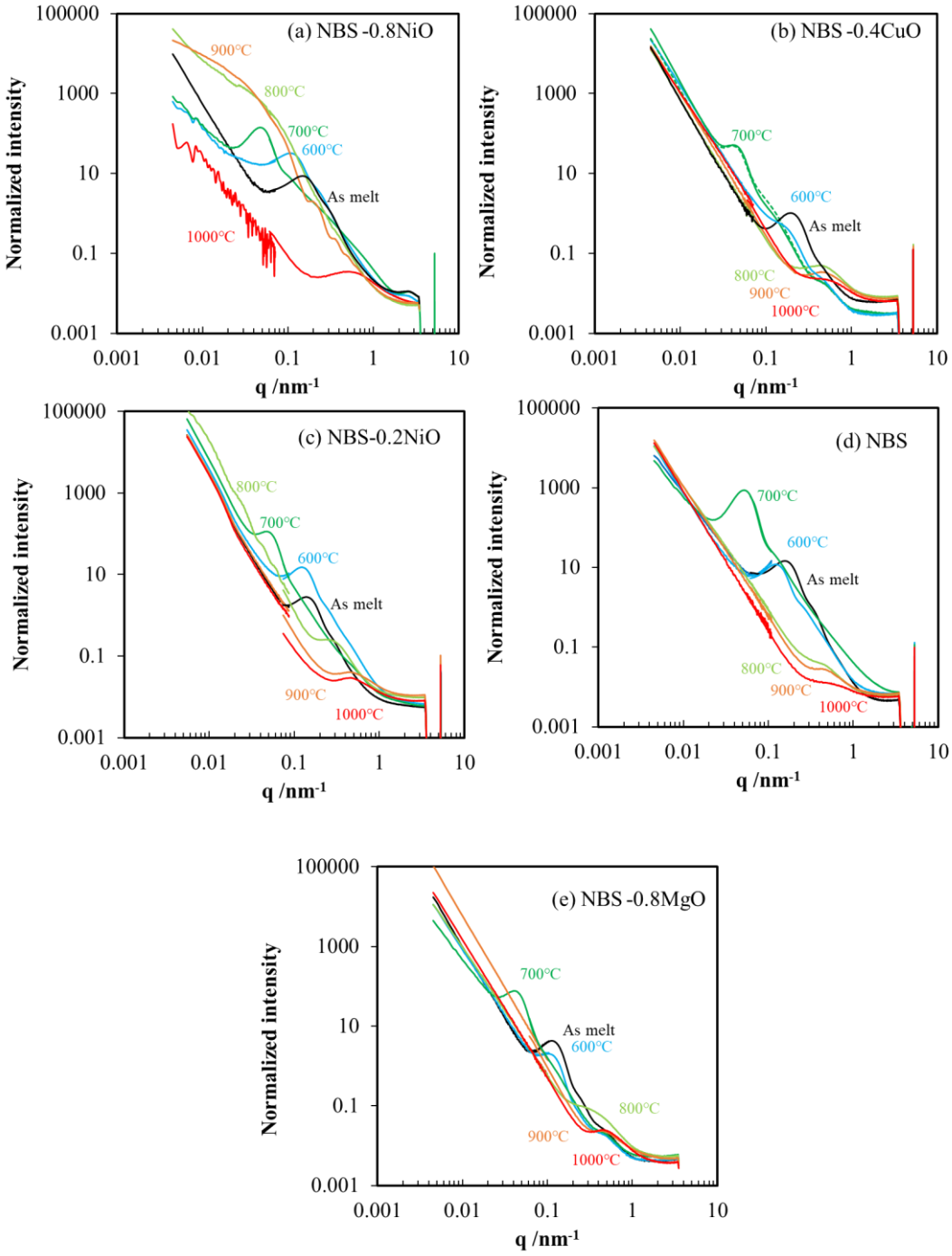

Figure 4.2 SAXS spectra of NBS glass (*K*=2) with varying additive ion species and amount. The samples were water-quenched after heat treatment at respective temperature for 20 minutes.

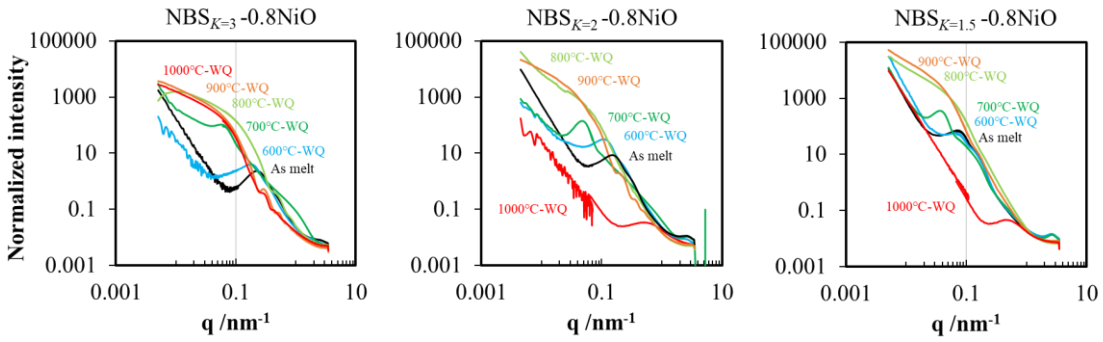

Figure 4.3 SAXS spectra of WQ samples with varying SiO_2/B_2O_3 ratio (*K*).

4.3.2 Effect of Ni^{2+} and Cu^{2+} ion on temperature dependence of immiscibility change in NBS glass observed by high temperature in-situ SAXS measurement

Figure 4.4 (a) shows the overview of time-resolved high temperature in-situ SAXS spectra of NBS-0.8NiO and NBS-0.4CuO obtained under temperature profile I (1 spectrum/ 2minutes), started with relatively homogeneous condition at room temperature (1000°C-WQ). Compared to NBS-0.8NiO, the changes in spectra appearance were less significant when the temperature is increased. Figure4.4 (b) shows the time dependence of correlation length L_{corr} obtained from SAXS spectrum. The rapid and significant increase of L_{corr} were not observed at 800°C in case of NBS-0.4CuO. Contrary, the L_{corr} started to decrease above 800°C.

Figure 4.5 shows the SAXS spectral change at each temperature region, comparing changes in NBS-0.8NiO and NBS-0.4CuO. The difference of dynamic behavior of phase separation were significant in wide temperature range. From room temperature to 600°C, the slight shoulder observed at room temperature showed totally opposite development in each composition. This shoulder in NBS-0.8 NiO showed shift toward lower q region around q=0.4~1.0 nm^{-1}, indicating the size increase as temperature increase. Contrary, the shoulder in NBS-0.4CuO became less significant as temperature increase. While holding at 600°C, NBS-0.8NiO kept developing the size of scatterer, while spectra showing typical spinodal phase separation. NBS-0.4CuO at 600°C showed slight emergence of peak at new region, around q<0.1 nm^{-1} including USAXS region, which was not obtained for in-situ measurement. After 1-hour hold at 600°C, NBS-0.8NiO and NBS-0.4CuO showed opposite change during heating up to 800°C. While NBS-0.8NiO significantly increased its scattering intensity in wide q-range, NBS-0.4CuO started to decrease the scattering intensity and reached to bottom at 800°C, where no further decrease of intensity could be observed in higher temperature up to

1200°C. The homogenization temperature of NBS-0.4CuO appeared to be around 700~800°C, without showing binodal phase separation. NBS-0.8NiO started to decrease its scattering intensity above 800°C and showed spectra with stable and low intensity. Although, its intensity started to decrease again during heating up from 1000°C to 1200°C.

In the cooling process from 1200°C melt, both glasses kept homogeneous until reaching to specific temperature. It started to increase scattering intensity below 933°C (±20°C) for NBS-0.8NiO and 780°C for NBS-0.4CuO. The major phase separation development stopped at 690°C for NBS-0.8NiO and 500°C for NBS-0.4CuO. The temperature range where homogenization started in heating process and phase separation develop started in cooling process were very similar in both glasses. From these results, NBS-0.8NiO apparently had much higher homogenization temperature compared to NBS-0.4CuO, consistent with the results obtained from WQ samples with different treatment temperature. There was slight peak around 0.4~1.0 nm^{-1} in 800~1000°C-WQ samples in NBS-0.4CuO, even though these temperature range appeared to be in miscible region from in-situ measurement. Considering the phase separation during cooling process in NBS-0.4CuO start with intensity increase around $q<0.1$ nm^{-1}, the residual peak in WQ samples had not been developed during cooling process.

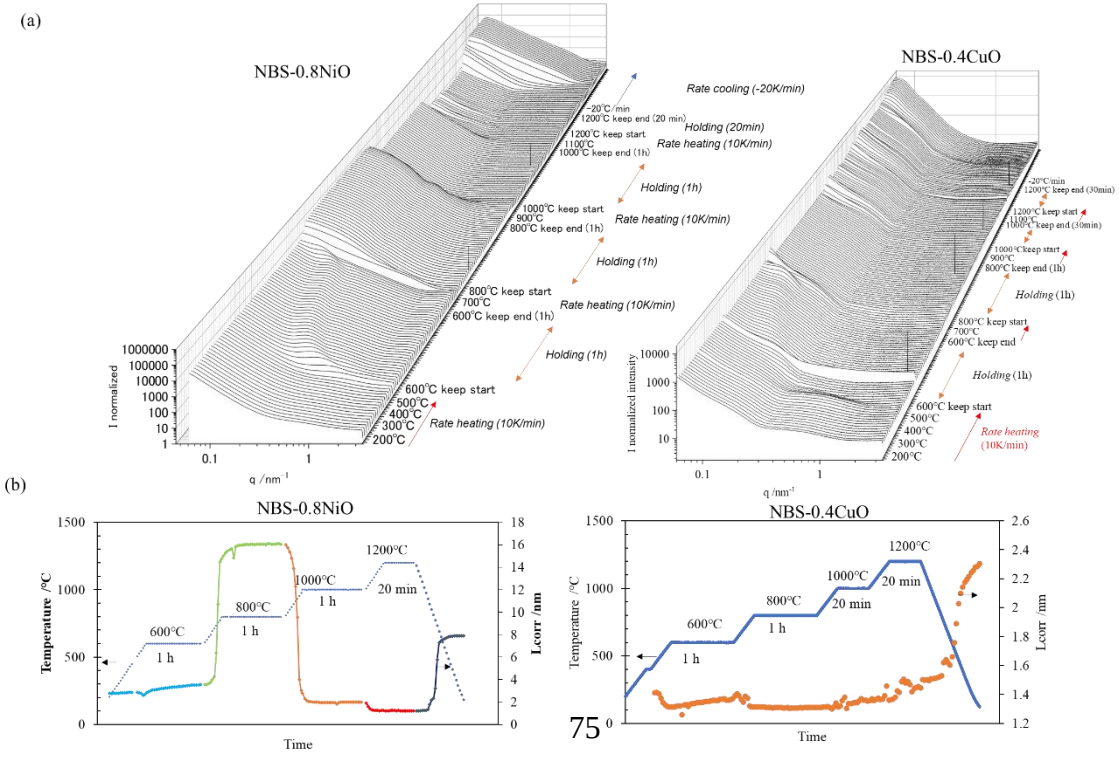

Figure 4.4 (a) Overview of time-resolved high temperature in-situ SAXS spectra of TM ion doped sodium borosilicate glass (NBS-0.8NiO and NBS-0.4CuO). Sample were kept under constant temperature at 600, 800°C, 1000°C (30 minutes), and 1200°C (30 minutes) respectively. (b) Time dependency of correlation length development observed from spectra shown in (a).

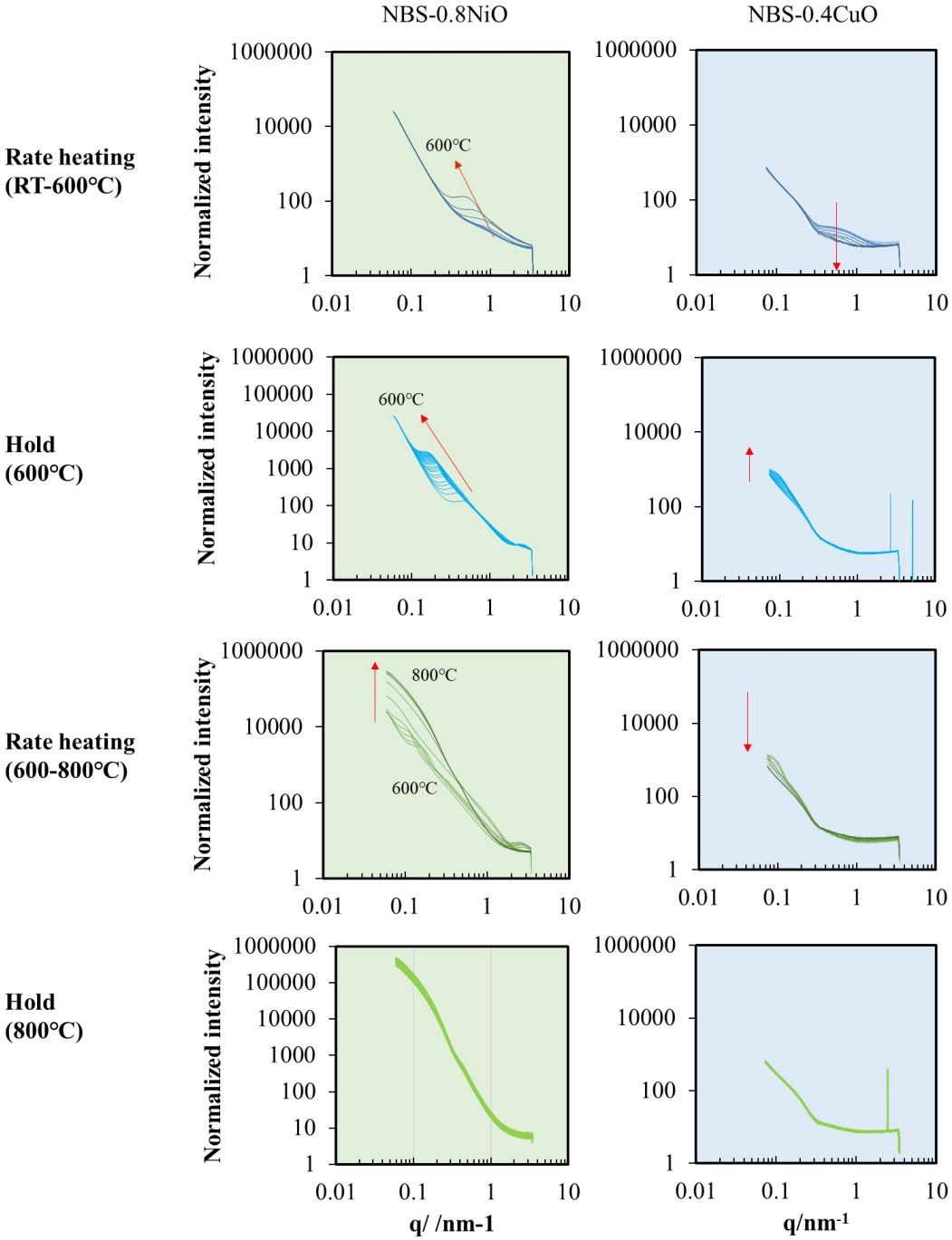

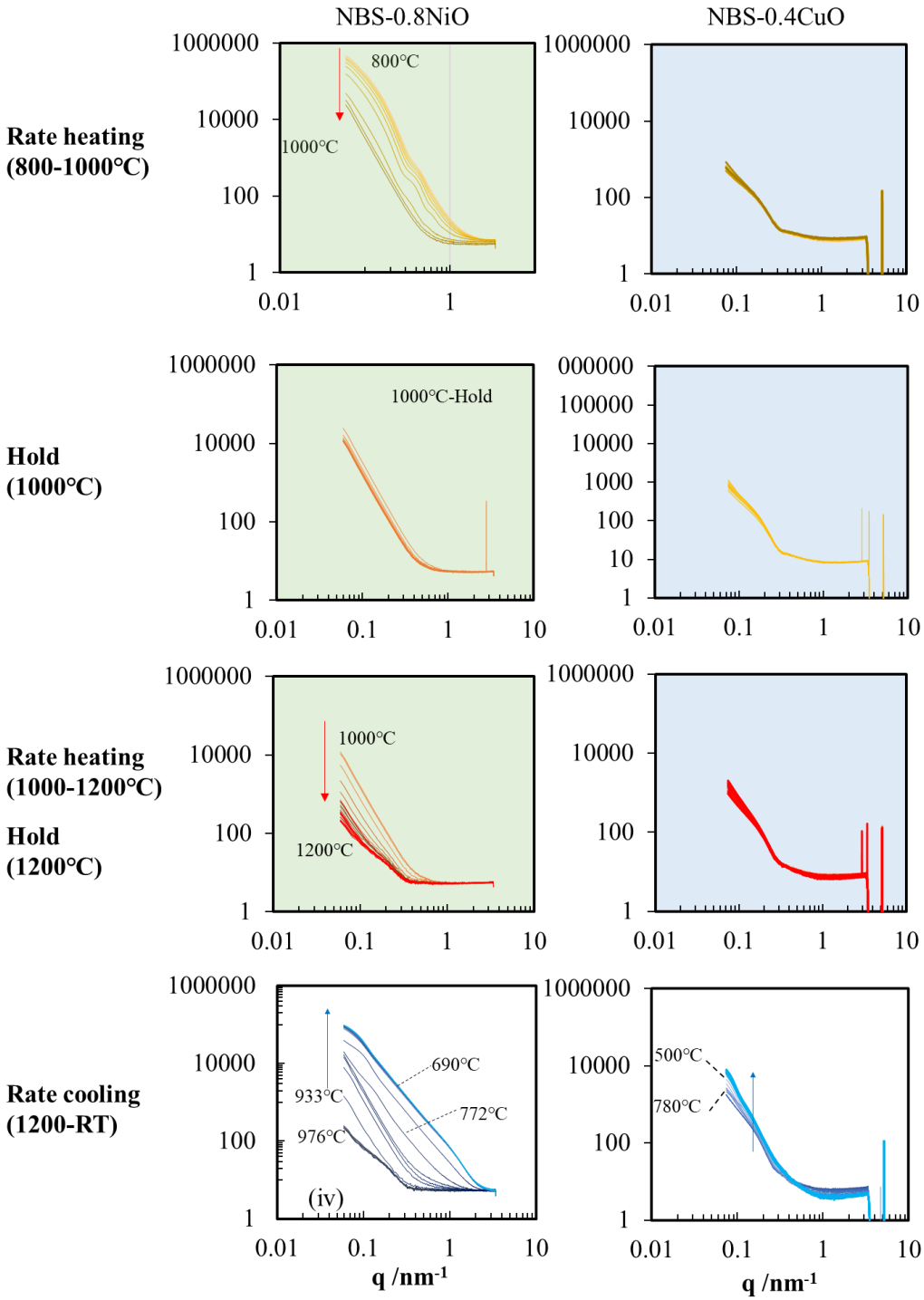

Figure 4.5 SAXS spectra of NBS-0.8NiO and NBS-0.4CuO obtained during high temperature in-situ measurement with temperature profile I shown in Figure 4.1.

4.3.3 Time-resolved observation of phase separation behavior during heating up to miscible temperature

Figure 4.6 shows SAXS spectra of NBS-0.8NiO and NBS-0.4CuO glasses measured during heating following temperature profile II explained in Figure 4.1. For NBS-0.8NiO, additional measurement was practiced on different immiscibility: homogeneous (1000°C-WQ, shown in (a)) and phase separated in spinodal (after 1000°C-WQ, heat treated at 580°C for 4 hours and cooled in room temperature, shown in (b)). The glass with composition of NBS-0.4CuO was started with spinodal phase separation as initial immiscibility, shown in (c).

The most significant difference by changing initial immiscibility appeared in temperature range below 600°C, by comparing **Figure 4.6 (a) and (b)**. When the homogeneous NBS-0.8NiO (1000°C-WQ) glass were heated up from room temperature, the Bragg-like peak started to appear from 560°C and the peak shifted toward low-q region. Contrary when phase separated NBS-0.8NiO were heated from room temperature, the existing Bragg-like peak kept decreasing its intensity at same peak position with increasing temperature. Although above 600°C, both initially homogeneous and phase separated NBS-0.8NiO glasses showed similar spectral transition while heating up to 800°C. In both cases, the Bragg-like peak started to shift toward low-q region while increasing its intensity, and the intensity got saturated at 765°C (±5°C). Afterwards, temperature dependence of dynamic behavior was very similar including the critical temperature where homogenization started, 940°C.

As shown in **Figure 4.6 (c)**, the phase separated glass with composition of NBS-0.4CuO showed different SAXS spectrum appearance at room temperature, but showed similar dynamic behavior when heating up from room temperature to 600°C. The Bragg-like peak is less significant in NBS-0.4CuO, though its intensity kept decreasing as temperature increase. Above 600°C, the scattering intensity started to decrease where Bragg-like peak existed, besides slight increase of intensity at high-q region. The developed scattering intensity in high-q region until 600°C started to decrease above 800°C. Above 1000°C, no significant change in spectra was observed.

Figure 4.7 shows explanation and results of time-resolved high temperature in-situ SAXS measurement with **temperature profile III**. Before the measurement, NBS-0.8NiO glass was cooled down from 1000°C with rate of -1°C. The sample were totally opaque and coloration of Ni^{2+} was green, both indicating highly immiscible structure. After acid leaching, Ni^{2+} ion was washed away, and FE-SEM image showed porous structure with larger silica rich phase volume and smaller pore volume compared to

Figure 3.2. These results indicate spinodal phase separation, though the SAXS spectrum appearance were different from spinodal phase separation formed after heat treatment at 580°C, without showing Bragg-like peak in the range of q=0.1~0.3 nm^{-1}.

When this highly opaque glass is heated from room temperature up to 800°C, no spectral change was observed. Above 800°C, the scattering intensity gradually started to decrease and its decay rate from 1004°C, and gradually stopped decreasing above 1070°C. The scattering intensity at high-g region (q>1 nm^{-1}) kept constantly low before and after heating, indicating the unavailability of phases smaller than 1 nm.

By cooling down the homogeneous melt at 1200°C down to 700°C, the phase separation developed again and showed increase of scattering intensity in entire q range observed in SAXS measurement (q=0.07~3 nm^{-1}). When it heated up to 800°C, the intensity a low q range increased and decreased at high- q range, showing similar spectrum appearance as binodal phase separation observed in chapter 3. Above 810 °C scattering intensity started to decrease again, starting homogenization. The significant change appeared from 975°C, and the decay stopped around 1076°C.

In case of **temperature profile III**, homogenization behavior of NBS-0.8NiO was clearly different depending on initial immiscibility. Slow cooling from 1000°C resulted in highly opaque phase separated glass, with stability of the immiscibility up to 800°C. Binodal phase separation growth was not observed at temperature range around 800°C. But once the glass turned homogeneous at high temperature melt, it started to similar homogenization behavior as **temperature profile II**. On the other hand, homogenization behavior of temperature profile I was totally different from the other temperature profiles.

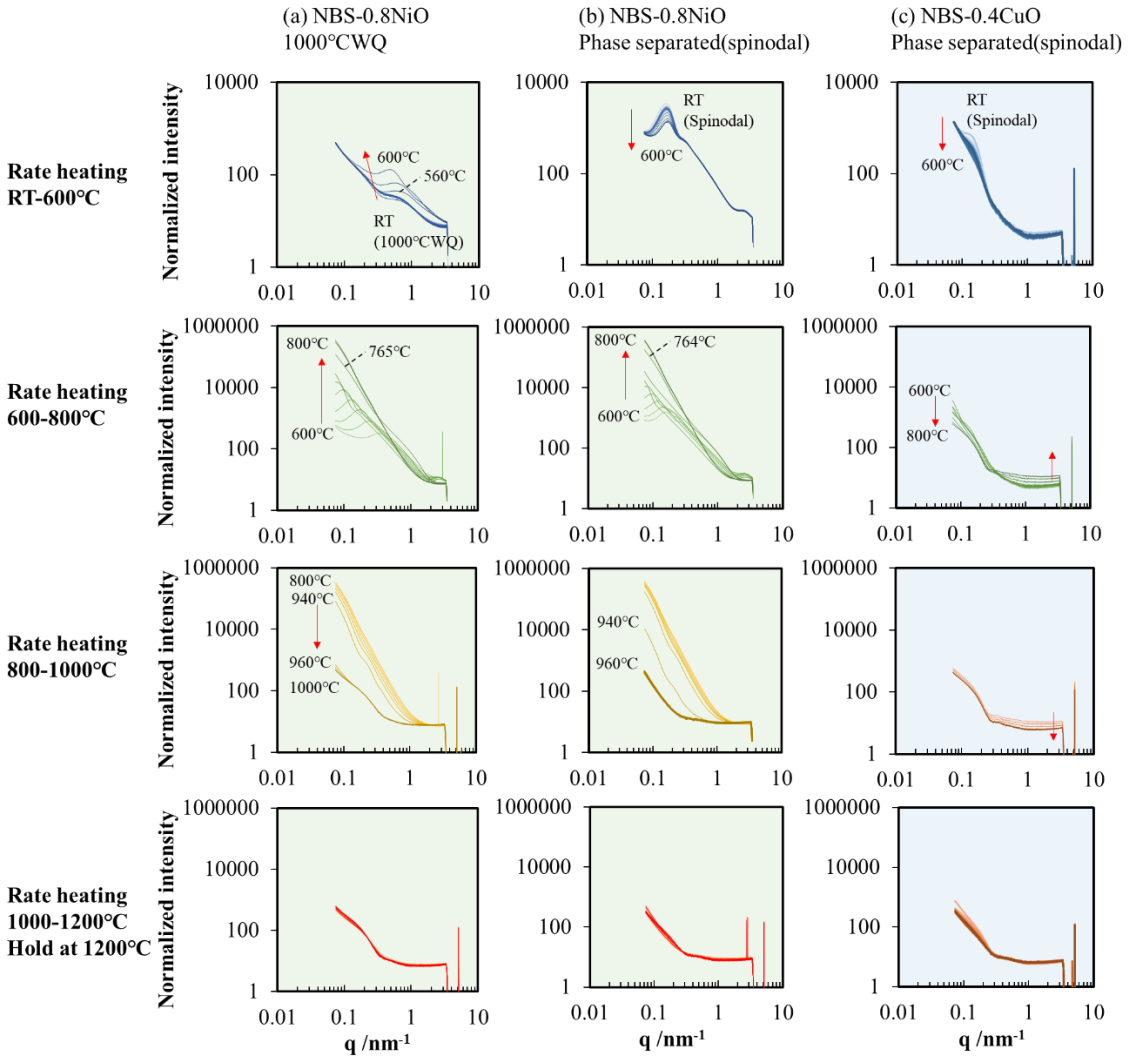

Figure 4.6 SAXS spectra of NBS-0.8NiO (green back) and NBS-0.4CuO (blue back) obtained during high temperature in-situ measurement with temperature profile II, with different heat treatment before measurement.

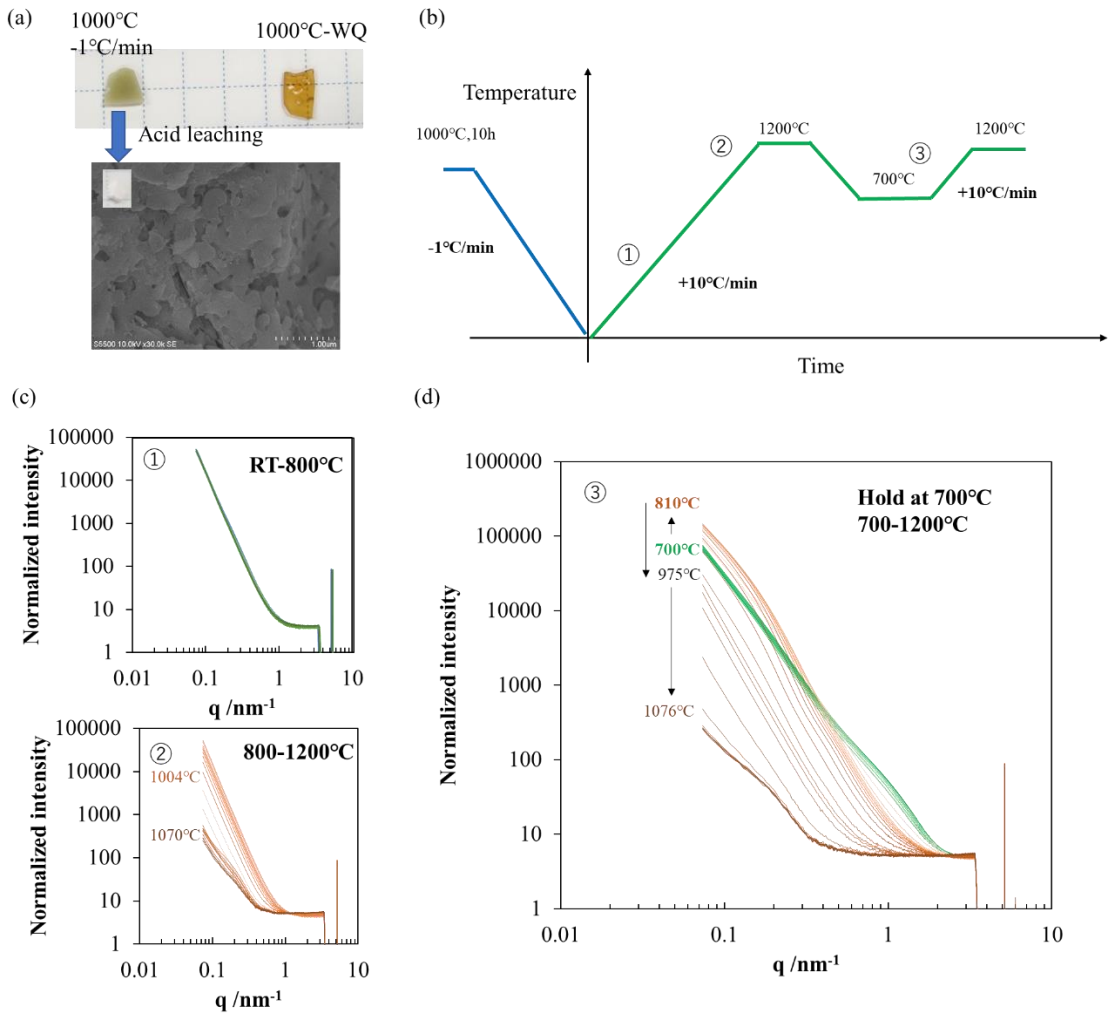

Figure 4.7 (a) The sample appearance of NBS-0.8NiO glass before in-situ measurement (Cooled down from 1000°C in rate of -10°C/min). In comparison, sample heat treated in 1000°C -WQ afterwards is shown in right. Images below show the microstructure of 1000°C -10°C /min sample after acid leaching. The sample were totally opaque-white without residual NiO, indicating porous silica remained after borate rich phase was washed away. (b) Temperature profile before and during high temperature in-situ SAXS measurement.(c) (d)SAXS spectra of NBS-0.8NiO obtained during high temperature in-situ measurement with temperature profile III.

4.3.4 Time-resolved observation of phase separation behavior during cooling down from miscible temperature

Figure 4.8 shows time resolved SAXS spectra obtained during cooling process down from 1200°C melt, with varying cooling rate. For NBS-0.8NiO glass, cooling rate of -50, -30, -20, -10 °C/min were measured. With any cooling rate, it was common that the

scattering intensity started to increase from high-q region, which might indicate that the phase separation growth started with abrupt appearance of relatively large scatter (>10 nm), besides gradual expansion starts from fluctuation. In addition, the temperature where scattering intensity growth started was almost independent of cooling rate, by most of the measurement observed intensity growth around 950°C. The scattering intensity at low q-region started afterwhile, from 760°~800°C. After reaching room temperature, all the samples showed high scattering intensity in entire q-range observed in SAXS measurement with no Bragg-like peak observed, which was very similar to the spectrum obtained after cooling down from1000°C by -1°C/min as shown in **Figure 4.7**. The glass cooled in -50°C/min showed slightly lower scattering intensity compared to other cooling rates.

The SAXS spectra obtained from NBS-0.4CuO showed less significant change, but the temperature where phase separation started could be observed. With cooling rate of -30°C/min, the scattering intensity development started below 694°C, and for -20°C/min development could be observed below 780°C. Those temperature were relatively lower compared to NBS-0.8NiO. The results are consistent with homogenization temperature in heating process, where NBS-0.4CuO showed lower critical temperature without showing binodal phase separation at 800°C. Contrary to NBS-0.8NiO, the scattering intensity of homogeneous NBS-0.4CuO glass showed slight decrease in high-q range ($q>1$ nm^{-1}) during cooling down. The temperature where the peak intensity reached lowest were marked in right column of **Figure 4.8** with yellow lines. The scattering intensity increase at this region was also observed when the NBS-0.4CuO glass was heated up from 600°C to 800°C, while scattering intensity at low-q region were decreasing as shown in the right column of **Figure 4.6**.

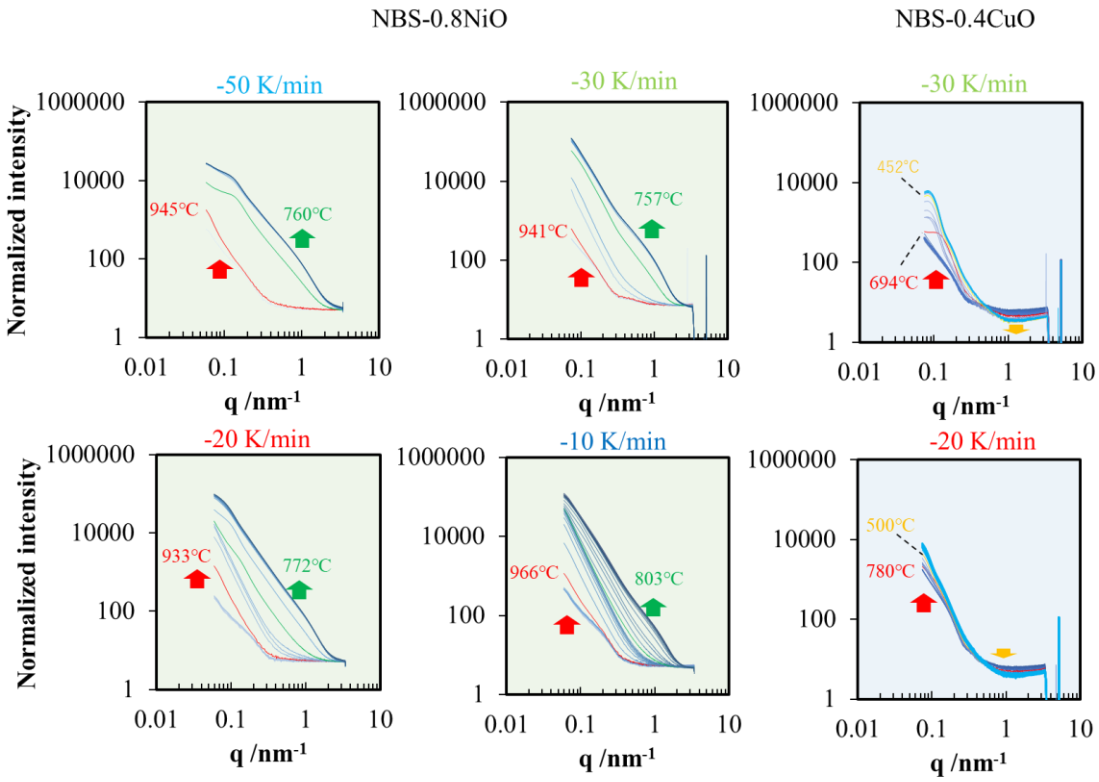

Figure 4.8 Time resolved high temperature in-situ SAXS spectra observed during cooling down from melt at 1200°C with varying cooling rates. In each plot, the temperature where the drastic increase started in high-q region (red) and low-q region (green). For NBS-0.4CuO, temperature where scattering intensity in high-q region was lowest is marked (yellow).

4.4 Discussion

4.4.1 Effect of additive transition metal ion on phase separation

The temperature dependence of phase separation behavior could be observed including size of the phases and their morphology from SAXS measurements. The approximate temperature dependence of phase separation in respective composition could be observed by room temperature measurement of WQ samples after various heat treatment temperature.

The effect of additional transition metal ion on phase separation behavior was much significant than difference observed in thermal properties below glass transition temperature. As shown in chapter 2, Tg and thermal expansion showed few changes within ±10°C and CTE ±0.5 $\cdot 10^{-6}\,m^{-1}$. Considering that further addition of NiO in NBS (*K*=2) glass had resulted in further difference, amount of NiO can be the dominant factor which decides the temperature dependence of phase separation, especially the critical temperature of homogenization. Since Ni^{2+} ion has similar cation field strength as Mg^{2+} ion[106], phase separation behavior of MgO-containing NBS glass.

The expansion of immiscible region and higher miscible temperature is reported by additive network modifier components[141]. Although **NBS-0.8MgO** glass did not show similar phase separation behavior as **NBS-0.8NiO** above 800°C, rather resembling to NBS glass without additive ion by scattering intensity decrease started from 800°C. In addition, the homogenization temperature of 1000°C observed with NBS-0.8NiO was higher than other reports of Na_2O-B_2O_3-SiO_2 (755°C [104]) system and Na_2O-MgO-B_2O_3-SiO_2 (790°C [142]) system. Considering these results and facts, significant change of phase separation behavior by additive of NiO more than 0.8 mol% is due to complex effect of strong cation field strength and higher molecular weight than MgO.

The NBS glass with higher SiO_2 content showed immiscibility even in higher temperature, as shown in **Figure 4.3**. The results indicate **NBS$_{K=2}$-0.8NiO** is located in right side of the phase separation dome with increasing homogenization temperature as SiO_2 contents increases, as illustrated in **Figure 4.9**. The reference ternary diagram of Na_2O-B_2O_3-SiO_2 system without NiO is shown in the left of **Figure 4.9 (a)**. Comparison of temperature dependence of phase separation with different additive TM ion is shown in (b). NBS-0.8NiO with K=1.5~3 showed binodal phase separation, with increasing population of droplet as silica contents increased. On the other hand, NBS-0.4CuO directly turned homogeneous after spinodal phase separation.

From chapter 2, both NBS-0.8NiO and NBS-0.4CuO successfully showed clear boundary between porous/ non-porous volume boundary by CW-laser scanning. Although the width of laser irradiated line was different: NBS-0.4CuO showed wider

homogenized volume, as shown in **Figure 2.10**. The lower homogenization temperature might have broadened the homogenization area at farther point away from laser focal point with lower accumulation temperature.

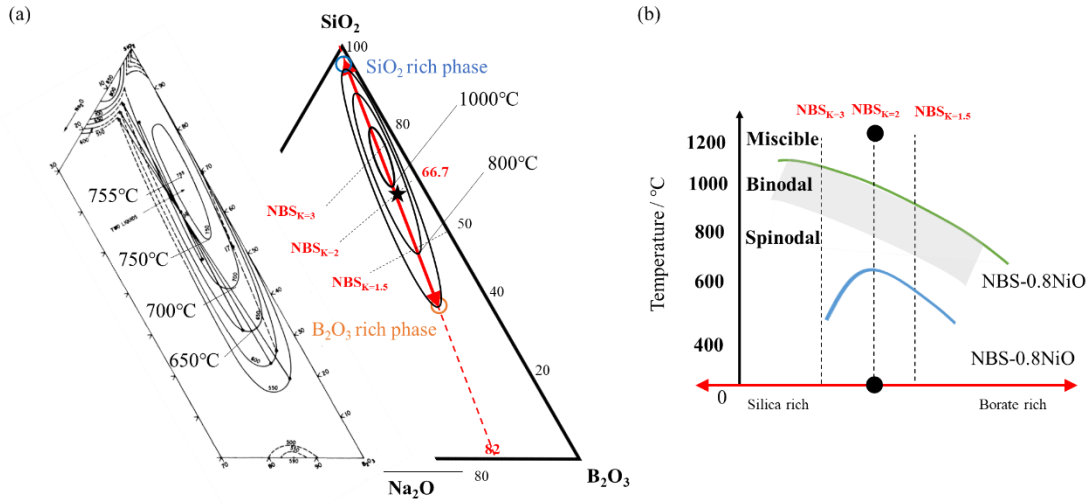

Figure 4.9 (a)(b) Approximate phase separation domain marked in ternary diagram of Na_2O-B_2O_3-SiO_2 after doping NiO. The main composition is marked with star. The reference diagram of Na_2O-B_2O_3-SiO_2 without NiO is from [104]**.**

4.4.2 Homogenization behavior during heating process of glass with various initial immiscibility

The effect of initial immiscibility on dynamic transient behavior toward homogenization could be observed by time-resolved high temperature in-situ measurement. These phase separation characteristics under non-isothermal treatment may give important clue on understanding the mechanism of partial homogenization in phase separated glass plate with heat introduction by laser absorption.

The time-resolved in-situ measurement showed different homogenization behavior depends on thermal history and initial immiscibility. **Figure 4.10** shows time-dependent change of correlation length L_{corr} in NBS-0.8NiO during heating up to 1200°C. There were 3 different types of homogenization behavior, with varying apparent homogenization temperature. Heating rate was +10°C/min for all temperature profile.

The lowest homogenization temperature was 960°C, shown as ***A*** in Figure 4.10. was observed when the 1000°C-WQ and PS (580°C for 4 hours, cooled in air) samples were heated straight up to 1200°C in +10°C/min (temperature profile II). Just before homogenization indicated by rapid decrease of Lcorr, the time-resolved development

behavior of binodal phase separation was matched exactly. Only difference among these two different time-resolved measurements was initial immiscibility and phase separation development behavior below 800°C. Although two sample showed different initial immiscibility, both samples had passed high temperature range in fast cooling rate and never exposed to that temperature range of 1000~800°C before heating for in-situ measurement.

The second lowest homogenization temperature was 1080°C as shown in ***B***, observed by heating up the SC (slowly cooled, -1°C/min from 1000°C) sample from room temperature to 1200°C (temperature profile III-①②) and the sample which was cooled down from 1200°C to 700°C in -10°C/min and hold at 700°C for 20 minutes (temperature profile III-③), heated from 700°C to 1200°C. The major difference between the samples showed lower homogenization temperature as marked ***A***, was that both samples in ***B*** had exposed to temperature range of 1000~800°C in slow cooling rate below -10°C/min before in-situ measurement.

Temperature profile I showed different homogenization behavior compared to ***A*** and ***B***. The decrease of L_{corr} was started soon after heated above 800°C, and stopped decreasing few minutes after reaching at 1000°C. While isothermal heating at 1000°C, no change was observed in L_{corr} and spectral appearance. Although by further temperature increase up to 1200°C, further decrease of L_{corr} and scattering intensity at q range of 0.08~0.4 nm^{-1}, as shown in **Figure 4.5**. This temperature profile had longest exposure time to 800°C before homogenization. It indicates the homogenization of phase separated NBS-0.8NiO glass is affected by binodal phase development under 800°C. Since binodal phase separation in this glass system yields silica-rich droplet as discussed in section 4.4.1, the diffusion process of silica might have been the last step which was rate-controlling the homogenization. Similarly, dissolution of quartz particle in borosilicate glass was reported to start dissolve from 600°C, and the size of quartz particle keep decreasing when heated up to 1200°C in 5°C/min [143]. For example, the dissolution of 45 μm quartz particle completed at 1100°C, besides the dissolution temperature become higher as particle size increases. Temperature difference of homogenization may be due to size of binodal silica droplets.

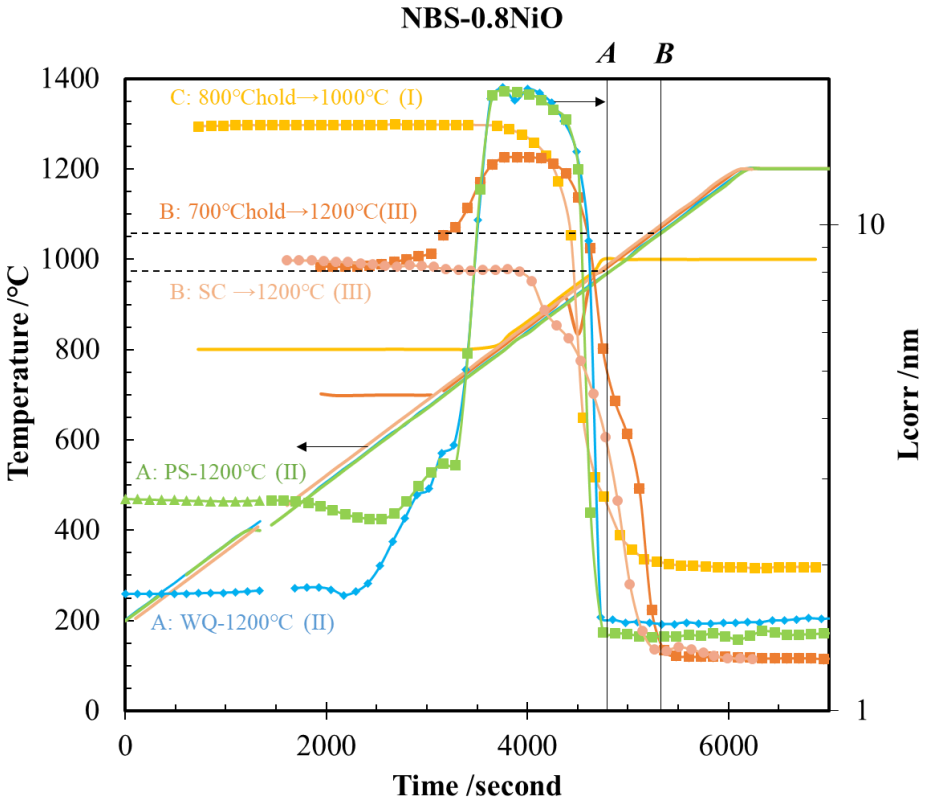

Figure 4.10 Time dependence of correlation length L_{corr} (Dots with line) during heating up NBS-0.8NiO glass to miscible temperature (1000°C or 1200°C). Solid line shows temperature profile. All profiles are set to be 6000 seconds when the temperature reached to 1200°C.

4.4.3 Phase separation development in cooling process from miscible melt

Figure 4.11 shows time resolved change of L_{corr} during cooling process from 1200°C, with varying cooling rate. Since all sample showed similar and lowest L_{corr} at 1200°C, the both NBS-0.8NiO and NBS-0.4CuO was considered as completely homogenized.

The glass composition of NBS-0.8NiO started to show phase separation at 940°C, independent of cooling rate. There were two different phase separation development behavior. One is observed with -50 K/min and -30 K/min: increase of L_{corr} rapidly grown from 940°C. Another behavior is observed with -20 K/min and -10 K/min: L_{corr} started to gradually increase at 940°C, then it changed growth rate rapidly increased at 810°C. This common temperature of growth rate change may indicate the clear boundary between miscible/ immiscible shown in phase separation dome and boundary of binodal/ spinodal, as the green line and bottom of gray shaded drawn in **Figure 4.9 (b)**.

With glass composition of NBS-0.4CuO, the L_{corr} growth retention was observed during cooling process, though the observed temperature range was different among respective cooling rates. Since the faster cooling rate showed lower boundary temperature, such differences may be due to delay of phase separation appearance due to lower viscosity.

The different immiscibility development behavior was observed in NBS-0.4CuO. The growth of L_{corr} in NBS-0.4CuO once stopped soon after the increment started with same increase rate. While L_{corr} apparently stopped increasing, q-range of major increase of SAXS spectra intensity changed from low-q to high q region. In higher temperature range, the scattering intensity increment was observed at $q<0.6$ nm^{-1}, while intensity at q>0.6 nm-1 kept decreasing. When the L_{corr} started to increase again, the scattering intensity at $q>6$ nm^{-1} start to increase slightly. The decrease of scattering intensity at high-q range during with phase separation development was not observed with NBS-0.8NiO. This result indicates residual scatterer at 1200°C. Since the size of scatterer is approximately 1 nm, it could be due to either phase separation or other atomic clustering.

Overall, the phase separation development could not be avoided with cooling rate of -50°C/min. Although faster cooling would help to avoid significant phase separation development before reaching room temperature. There was remarkable difference between NBS-0.8NiO and NBS-0.4CuO: the homogenization temperature was lower in NBS-0.4CuO by 200°C. The effect of this difference in phase separation behavior will be considered in next chapter, reflecting critical temperature value to thermal history obtained from calculation.

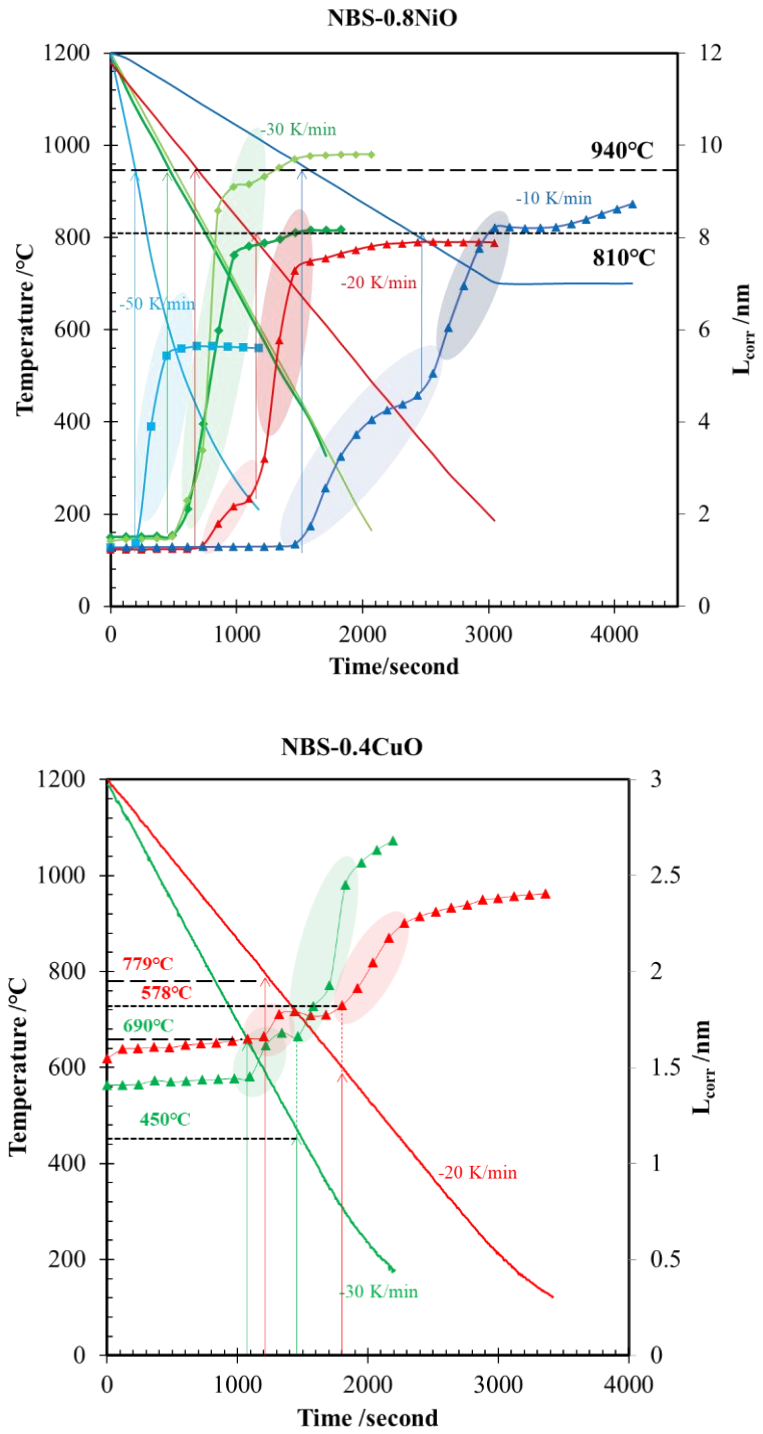

Figure 4.11 Time dependence of correlation length L_{corr} (Dots with line) during cooling down NBS-0.8NiO and NBS-0.4CuO glass from 1200°C, where all the samples showed high miscibility.

4.5 Summary

Morphology of nanoscale immiscibility due to phase separation could be evaluated by SAXS spectra. Both the effect of composition and thermal history on phase separation behavior could be observed by SAXS measurement on various composition and time-resolved high temperature in-situ measurement respectively.

The addition of NiO in NBS glass drastically changed phase separation behavior compared to other additive components. The homogenization temperature increased by 200°C compared to the NBS glass without additive ion. Also, binodal phase separation were observed with addition of 0.8 mol% NiO, which was not available in the NBS glass without additive ion, and also NBS with other additives such as CuO and MgO.

Time-resolved high temperature in-situ measurement of SAXS spectra revealed dynamic behavior of homogenization of phase separated glass during heating and development during cooling from miscible melt. The homogenization of phase separated glass in NBS-0.8NiO was dominated by dissolution of silica rich phase droplet developed under exposure of 800°C. The glass with composition of NBS-0.4CuO turned directly from spinodal phase separation to homogeneous glass.

In cooling process, the temperature where phase separation start was independent of cooling rate when homogenization temperature is high enough to show low viscosity. When phase separation started to develop from low temperature near glass transition temperature, phase separation development was too slow to follow -30K/min. The actual temperature range of active phase separation development was obtained from time resolved SAXS measurement under isothermal heat treatment in respective glass composition.

5 Computer simulation on spatial distribution of thermal history and phase separation in glass substrate by laser heating

5.1 Introduction

In chapter 4, the homogenization behavior during heating and phase separation development from miscible melt during cooling down were obtained from time-resolved high temperature in-situ SAXS measurement. From analysis, specific temperature of boundary between miscible and immiscible was obtained for respective composition. Considering these actual phase separation behavior, mechanism of boundary formation between porous /non-porous volume by laser heating process on glass is expected to be clarified.

In this chapter, thermal history in glass substrate during laser scanning were calculated by finite element method using COMSOL. By comparing thermal history distribution with actual laser irradiated and acid leached sample, how the clear boundary was formed and required thermal history was considered.

5.2 Theory

5.2.1 Heat transfer and laser absorption in a glass substrate

The heat transfer in the solid material obeys the following equation [144]:

$$\rho C_p \frac{\partial T}{\partial t} + \nabla \cdot \boldsymbol{q} = Q \tag{5.1}$$

$$\boldsymbol{q} = -k\nabla T \tag{5.2}$$

where ρ is the density (SI unit: kg/m^3), C_p is the specific heat capacity (J/(kg·K)), k is thermal conductivity (W/(m·K)), T is absolute temperature (K), $\boldsymbol{q}$ is the heat flux by conduction (W/m^2), and Q contains additional heat source (W/m^3). There were two different heat sources considered in this laser heating model in glass:

$$Q = Q_{laser} + Q_{rad} \tag{5.3}$$

Laser absorbed heat Q_{laser} and radiative heat from higher temperature volume Q_{rad}. Since glass substrate is highly transparent toward laser light, the transmitted light on the surface is absorbed by the inner volume underneath. The intensity I_i (W/m^2) of i^{th} beam through the material decreases as the beam propagates and is absorbed by the medium. This is described by the Beer-Lambert Law equation:

$$\frac{e_i}{||e_i||} \cdot \nabla I_i = -\left(\kappa(\lambda) I_i + \varepsilon_0(T) e_{b,\lambda}(\lambda, T)\right) \tag{5.4}$$

where e_i is the orientation of the i^{th} beam, $A(\lambda)$ is the absorption coefficient (m^{-1}) of the

medium with λ is wavelength of the incident laser light (nm), ε_0 (T) is material emissivity depends on temperature, and $e_{b,\lambda}(\lambda, T)$ is black body emissive power (W/m^3) depends on wavelength and temperature. The blackbody emissive power is defined as:

$$e_{b,\lambda}(\lambda, T) = \frac{2\pi {n_r}^2 h {c_0}^2}{\lambda^5 \left(e^{\frac{hc_0}{\lambda k_B T}} - 1 \right)} \tag{5.5}$$

where n_r is refractive index of the media, h is Planck constant (J·s), c_0 is the speed of the light in vacuum (m/s), k_B is the Boltzmann constant (J/K), and λ is considered as laser wavelength to be absorbed. Here, the laser absorption due to thermal radiation is also included. From the conservation law of energy, material reflectivity R_0 and absorptivity A_0 has relation of $1 = R_0 + A_0$. Kirchhoff's law states that the material emissivity ε_0 at thermodynamic equilibrium is equal to the absorptivity; $A_0 = \varepsilon_0$. So when the material shows radiation in wavelength of laser light, the laser is absorbed as much as radiated. Here $\kappa(\lambda) I_i$ can be considered as laser absorption due to additive TM ion and $\varepsilon_0(T) e(\lambda, T)$ is due to heat radiation in glass network.

Assuming the total laser absorbed intensity I_λ in glass substrate with thickness L under incident laser intensity I_0,

$$I_\lambda = I_0 e^{-\kappa_{Laser} \cdot L} \tag{5.6}$$

equation (5.4) can be simplified as

$$\frac{e_i}{||e_i||} \cdot \nabla I_i = -\left(\kappa(\lambda) + \frac{\varepsilon_0(T) e_{b,\lambda}(\lambda, T)}{I_\lambda} \right) I_i = \kappa_{Laser}(\lambda, T) I_i \tag{5.4}'$$

The heat introduces by laser absorption correspond to the energy deposited by laser beam:

$$Q_{laser} = \sum_i \kappa_{Laser}(\lambda, T) I_i \tag{5.7}$$

Here the laser incident direction is defined as $e_i = (0, 0, -1)$. When the gaussian laser beam is exposed by scanning velocity of v (m/s) along x-axis on the glass substrate surface in x-y plane,

$$I_i = (1 - R_0) \frac{2P_o}{\pi w(z)^2} \mathrm{e}^{\frac{-2\left((x_0 + vt)^2 + y^2\right)}{w(z)^2}} \tag{5.8}$$

where P_0 is laser power (W), $w(z) = w_0 \sqrt{1 + \left(\frac{\lambda z}{\pi {w_0}^2} \right)^2}$ is spot size at z (m) away from surface, beam spot size w_0 (m) at focal point, and x_0 (m) is the beam location at t=0 (s).

Focusing on the surface boundary between solid and air, the heat conduction and radiation from surface to ambient radiation is considered [145]:

$$\boldsymbol{q} = h(T_{amb} - T) + \varepsilon \sigma_{SB} \left({T_{amb}}^4 - T^4 \right) \tag{5.10}$$

where h is heat transfer coefficient , ε is surface emissivity, σ_{SB} is Stefan-Boltzmann constant (W/(m^2·K^4)) and T_{amb} is temperature of ambient air surrounding the solid.

5.2.2 Radiation model in thin transparent media

Radiative heat transfer is highly dominant in transparent materials compared to opaque materials [146]. Here let I_λ be the monochromatic intensity of radiation. When the beam traverses distance ds, its attenuation due to absorption $-dI_\lambda$ is given by:

$$-dI_\lambda = \kappa_\lambda I_\lambda ds$$
$$I_\lambda = I_{0\lambda} e^{-\kappa_\lambda s} \tag{5.7}$$

where κ_λ is monochromatic absorption coefficient.

The radiation regime depends on the optical thickness $\tau_{o\lambda} = \kappa_\lambda L$ of absorbing medium[147]. In optically thick media $\tau_{o\lambda} \gg 1$, radiative heat transfer is approximated as heat flux $\boldsymbol{q_r}$ expressed by Rosseland approximation:

$$\boldsymbol{q_r} = -\frac{16{n_r}^2 \sigma_{SB} T^3}{3\beta} \nabla T \tag{5.8}$$

where β is extinction coefficient. Although when $\tau_{o\lambda} \gg 1$, in a case such as sample thickness is thin with high transparency, mean free path of the photon $1/\kappa_\lambda$ become longer than sample thickness. In such a case, temperature calculation accuracy would be discarded. To obtain more accurate result with high resolution, the general radiative transfer equation can be written as:

$$\Omega \cdot \nabla I(\Omega) = \kappa\big(I_b(T) - I(\Omega)\big) \tag{5.9}$$

Without effect of scattering, including blackbody radiation intensity $I_b(T) = \frac{{n_r}^2 \sigma_{SB} T^4}{\pi}$.

The radiation incident $G = \int_{4\pi} I(\Omega) d\Omega$ where $I(\Omega)$ is the radiative intensity at given position following Ω direction, should be considered. Based on P1 approximation [148], radiative heat can be expressed as

$$Q_{Radiation} = \nabla \cdot (D_{P1} \nabla G) = \kappa(G - 4\pi I_b) \tag{5.10}$$

Where $D_{P1} = 1/3\kappa$ is P1 diffusion coefficient. Assuming gray body radiation (ε <1, wavelength dependence is neglected), κ was defined as average of spectral absorption coefficient.

5.3 Experimental

5.3.1 Apparent Laser absorbance measurement

The apparent laser absorbance of the glass substrate was measured to obtain the material parameter to be used in calculation. The glass substrate of NBS, NBS-0.8NiO, NBS-0.4CuO with sample thickness of 0.1, 0.2, and 0.4 mm were prepared. The laser was irradiated with 4.2 W, 5.7 W, and 7.2 W by 0.5 mm/s, during heating at 100°C. The transmitted laser light intensity was directly measured by power meter.

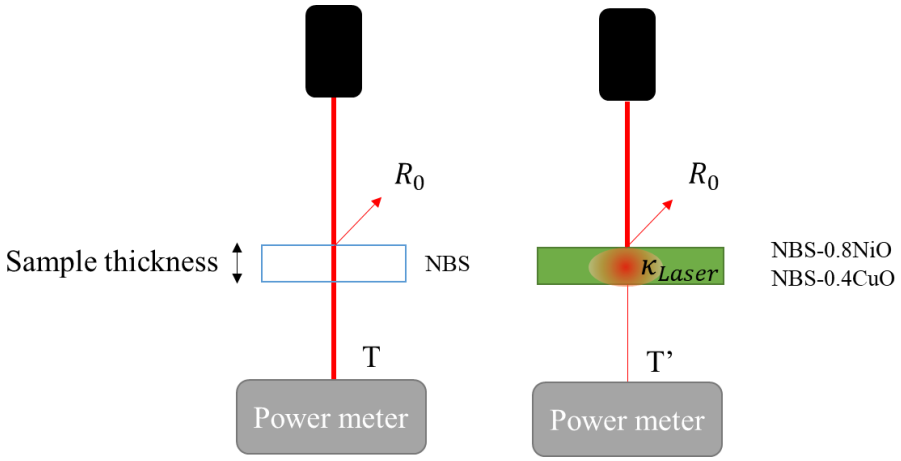

Figure 5.1 Schematic of laser absorbance measurement setup

5.3.2 Thermal history calculation by finite element method

A multi-physics model-based 3D finite element (FE) heat transfer model on COMSOL™ platform was developed to predict the thermal histories during laser scanning on the glass substrate. The solid with *heat transfer* (ht) model was built with *radiation in participating media* (*rpm*) module. As illustrated in **Figure 5.2,** *radiative beam in absorbing media* (*rbam*) was applied on the separate volume with width of laser beam waist. The ambient temperature was set as 100°C, considering the sample was heated while laser was exposed. The sample thickness was 0.5 mm, with cubic sample of 5 mm×13 mm, with thermal insulation at all side surface parallel to *z*-axis. The time dependence of temperature profile was calculated, with laser scanning started from laser focal position of (-5, 0, 0) in mm.

The parameters used in the calculation are shown in **Table 5.1** and **Figure 5.3**. For heat capacity and emissivity, temperature dependence of their value was included in the calculation. The density of the target glass was experimental value obtained by pycnometer at 27°C. Laser absorbance due to d-d transition were obtained from UV-vis measurement at room temperature. Spectral absorbance κ was less dominant for result temperature in range of 2~100 m^{-1}.

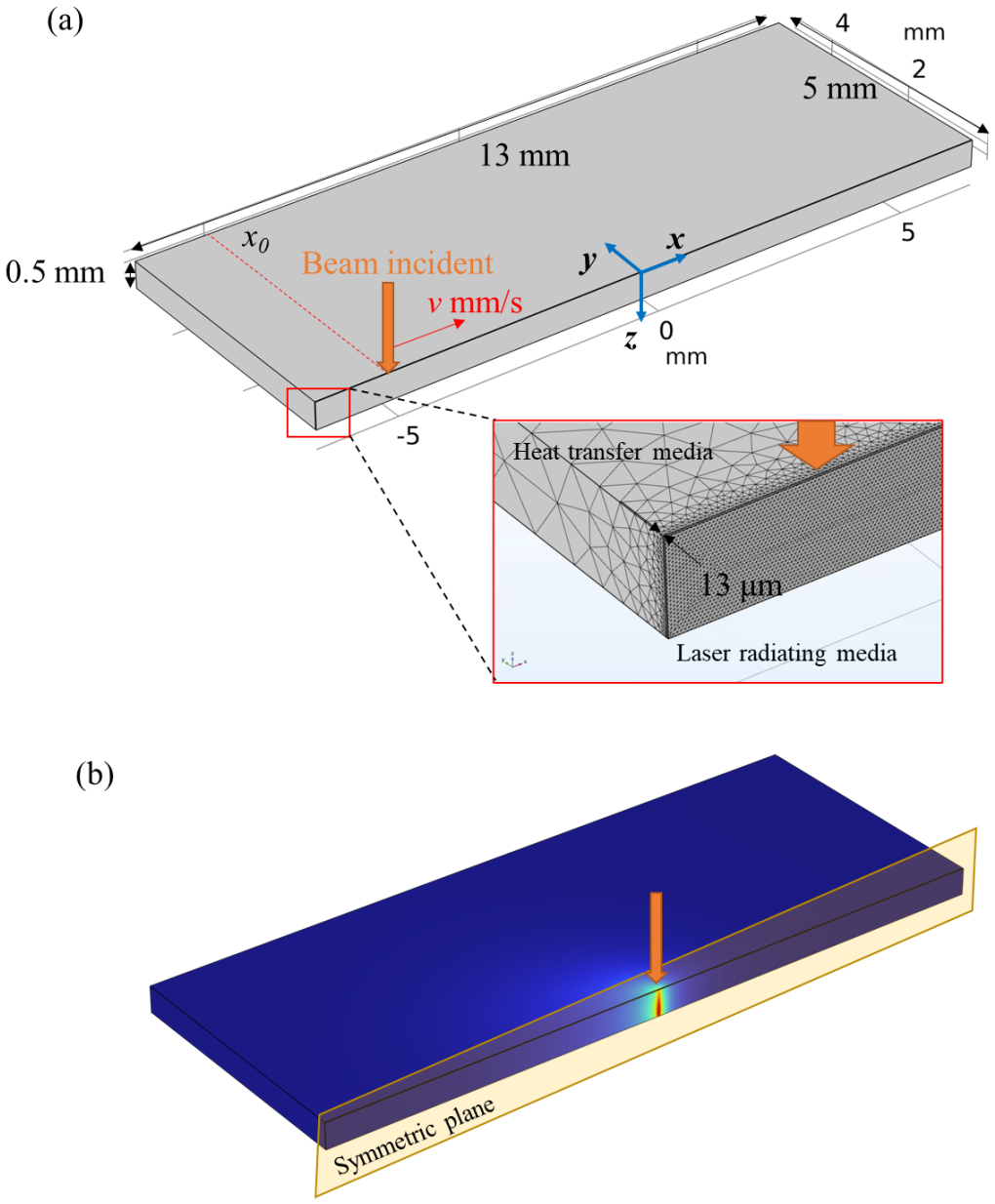

Figure 5.2 (a) Geometry of the heat transfer calculation model. The inset shows the laser exposed volume separately built with its width of laser beam waist at focal point. (b) Example of temperature profile plot. The calculation was simplified by considering the symmetricity of laser heat transfer shows against *x*-*z* plane, parallel to laser scanning direction.

Table 5.1 The parameters used in calculation. Temperature dependence was considered for dominant parameters.

Properties		**Value**	**unit**	**ref**
Density	ρ	2219	kg/m^3	Measured
Specific heat capacity	Cp (T)	**Figure 5.3**	J/kg·K	Data of Pyrex glass from [149]
Heat conductivity	*k*	0.835	W/m·K	[150]
Emissivity	ε (T)	**Figure 5.3**	-	Data of window glass (thickness: 0.1 cm) [103]
Laser absorbance (Absorption due to d-d transition at 1064 nm)	*A* (λ=1064 nm)	80	1/m	**Figure 2.2** Measured
Refractive index	n_r	1.5	-	[150]
Spectral absorption coefficient	κ	27	1/m	[151]
Heat transfer coefficient to air	*h*	10	$W/m^2·K$	[145]

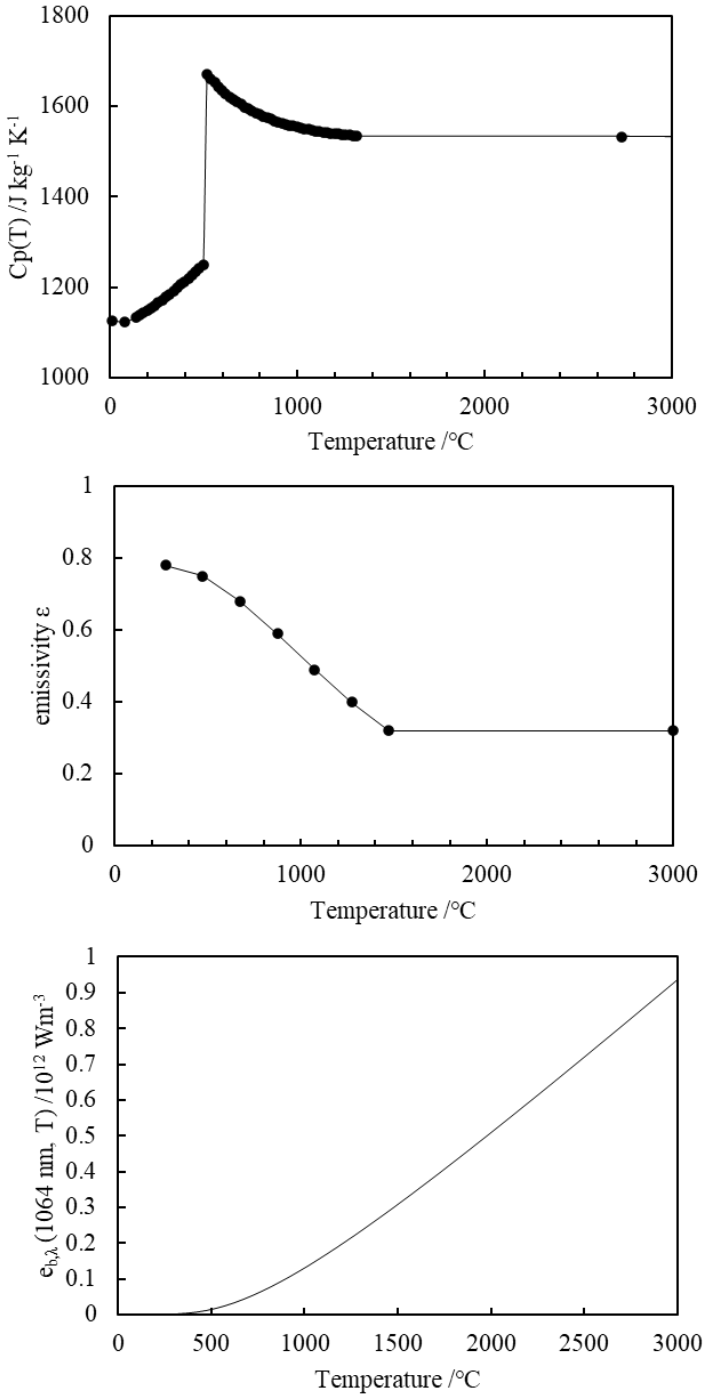

Figure 5.3 Temperature dependence of some parameters used in the calculation. The value of Cp(T) is data of Pyrex glass from [149]**. Emissivity is data of window glass with thickness of 0.1 mm** [103]**. The value of e $_{b,\lambda}$ (1064 nm, T) was calculated from equation (5.5).**

5.4 Result

5.4.1 Apparent laser absorbance measurement

The transmitted laser (λ=1064 nm) intensity of glass substrate was measured directly. In the glass substrate with composition of NBS, there were no absorption of the light with wavelength of 1064 nm as shown in Figure 5.4 The peaks in visible range are due to d-d transition of additive transition metal ion. Both NiO and CuO added glass had similar absorbance at λ=1064 nm. The difference among NiO and CuO was dominance of absorbing band. For NBS-0.8NiO, the main absorption band was around 400 nm and its position shifted when the coordination number changed from 6-coordinated (as-melt) to 4-coordinated (1000°C-WQ). Considering the high-temperature in-situ measurement in chapter 3, the absorbance of main absorption band may increase at high temperature. Considering that absorbance value of NBS glass at 1064 nm was 20 m^{-1}, absolute absorbance of NBS-0.8NiO and NBS-0.4CuO were approximated by subtracting 20 cm^{-1} from the indicated value in **Figure 5.4.**

The apparent laser absorbance was obtained from the ratio between transmitted laser intensity I and initial intensity I_0 (I/I_0=Transmittance), as shown in **Figure 5.5**. Without glass substrate, the ratio was always 1, with any laser intensity. From laser irradiation on the NBS glass without additional TM ion, the ratio was independent of the sample thickness and 0.94. This result indicate there were no absorption in NBS glass and the reflectivity at the surface was about $\boldsymbol{R}$=0.06. By setting NBS-0.8NiO or NBS-0.4CuO glass, the intensity was further decreased as the sample thickness increased. The thickness dependence of absorbance in NBS-0.8NiO was approximately following the Lambert-Beer law. Absorption coefficient of $\boldsymbol{A}$=2.1 cm^{-1} could be obtained. Contrary, NBS-0.4CuO showed different thickness dependence.

Based on the results obtained from apparent laser absorbance, I_λ in equation (5.4) was approximated as

$$I_\lambda(z) = (1-\boldsymbol{R})\frac{2P_o}{\pi w(z)^2}\exp(\boldsymbol{A}z) \tag{5.11}$$

Where the surface of glass substrate relies on x-y plane and has thickness in negative direction along z-axis.

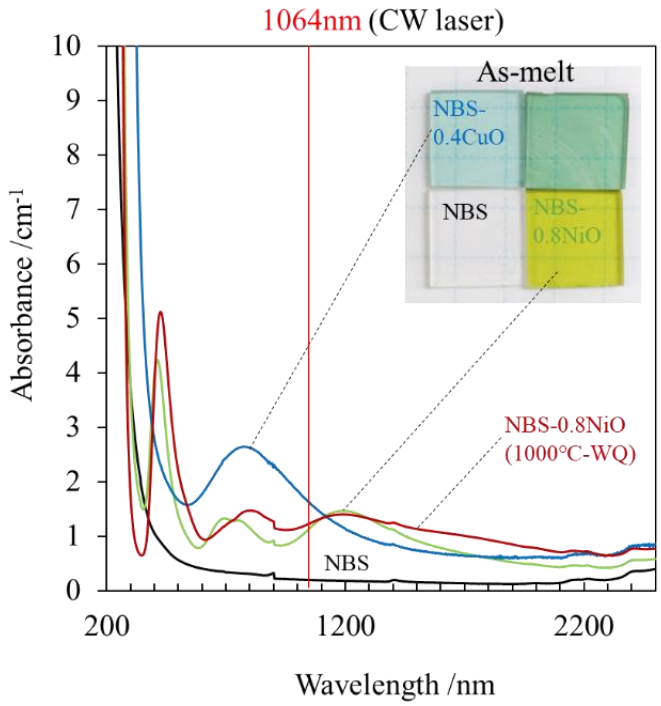

Figure 5.4 UV-vis absorption spectra of the glasses with target composition.

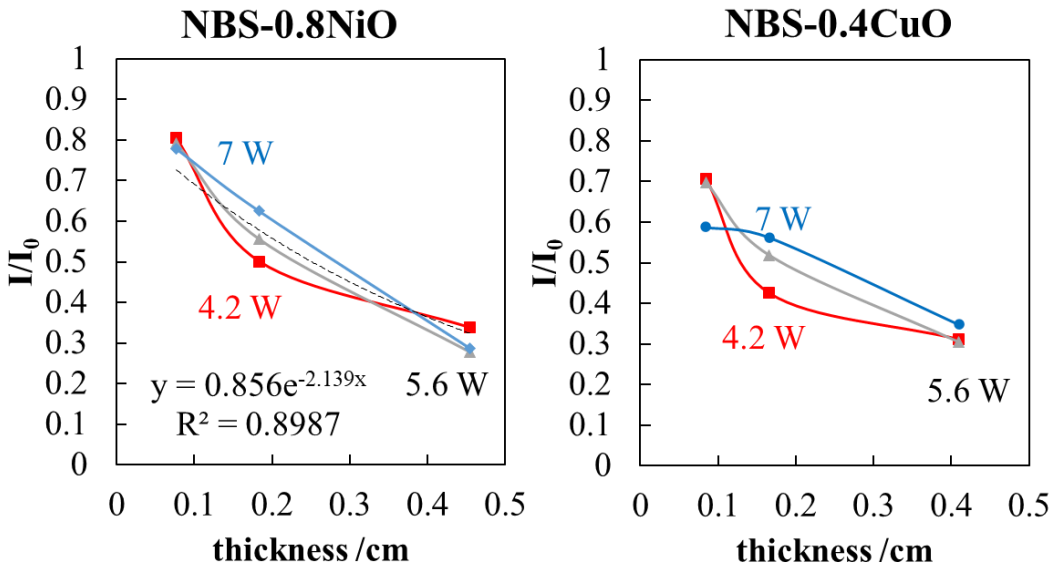

Figure 5.5 Laser (λ=1064 nm) intensity ratio (transmittance) in NBS-0.8NiO and NBS-0.4CuO glass substrate during heating at 100°C with different thickness.

5.4.2 Temperature calculation in laser absorbing media

The temperature distribution in y-z plane at x=0 calculated by FE method is shown **Figure 5.6 (a)**. The laser irradiation with 4.3 W with different scanning speed (1.0 mm/s and 0.5 mm/s) and 1 mm/s with varying laser power (4.3 W, 5.7 W, and 7.2 W) was focused, since the clear boundaries between porous and non-porous region were observed with some of these scan speed and laser power combinations. Each color is attributed temperature range from 100 to 940°C as shown in the bar, where 940°C was found to be homogenization temperature of NBS-0.8NiO. The temperature above 940°C indicated by same color. The vertical dot line representing the location of boundary between porous and non-porous region observed in actual NBS-0.8NiO substrate. By comparing with cross section of laser-irradiated glass substrate, these dot lines were always located at the boundary between temperature range of 900°C (plotted in red) and higher temperature above 940°C (dark red). These coincidences indicate the certain validity of the calculated results. NBS-0.4CuO showed much wider affected volume, especially laser irradiation above 5.7 W. The result was reasonable considering NBS-0.4CuO had lower homogenization temperature.

The temperature profile along the laser incident direction (z-axis) was distinctive from simple Lamber-Beer law, which would usually become narrower as the penetration depth become deeper. The width of high temperature (T>940°C) distributed volume became widest at very middle of sample thickness. This result was very similar to the actual laser affected volume observed in chapter 2, showing barrel-like shape along z-direction.

By the laser irradiation with 4.3 W and 0.5 mm/s, both NBS-0.8NiO and NBS-0.4CuO. The temperature at surrounding of the laser scanning center reached above 940°C for about 1 second. The apparent laser affected line width was almost same among two compositions. Though for NBS-0.4CuO, the homogenized volume was surrounded by different porous structure compared to original porous structure. The temperature range of surrounding volume approached up to 800~900°C foe 0.5 seconds and remained around 600°C for a while after laser focal point passed away. The irradiation with 4.3 W 1.0 mm/s showed similar result, with shorter duration at temperature above 940°C (0.1 second). NBS-0.8NiO showed clear boundary of porous / and non-porous volume, though NBS-0.4CuO showed gradual appearance of porous structure as distance increases in y-axis direction.

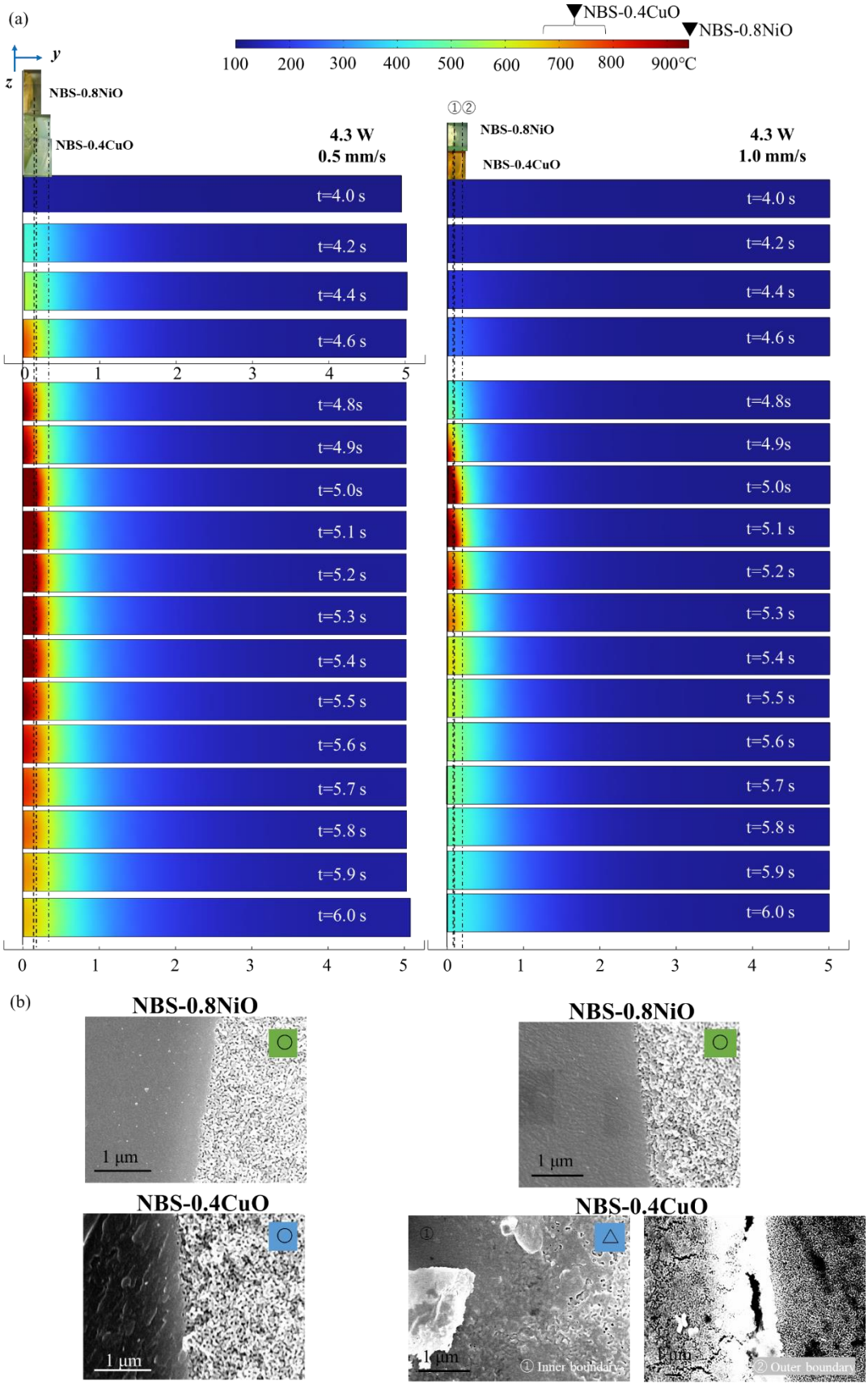
(a)
NBS-0.4CuO
NBS-0.8NiO
100 200 300 400 500 600 700 800 900°C
y
z
NBS-0.8NiO
NBS-0.4CuO
4.3 W
0.5 mm/s
①②
NBS-0.8NiO
NBS-0.4CuO
4.3 W
1.0 mm/s
t=4.0 s
t=4.2 s
t=4.4 s
t=4.6 s
t=4.8s
t=4.9s
t=5.0s
t=5.1 s
t=5.2 s
t=5.3 s
t=5.4 s
t=5.5 s
t=5.6 s
t=5.7 s
t=5.8 s
t=5.9 s
t=6.0 s
0 1 2 3 4 5
(b)
NBS-0.8NiO
NBS-0.8NiO
1 μm
1 μm
NBS-0.4CuO
NBS-0.4CuO
1 μm
1 μm
① Inner boundary
② Outer boundary

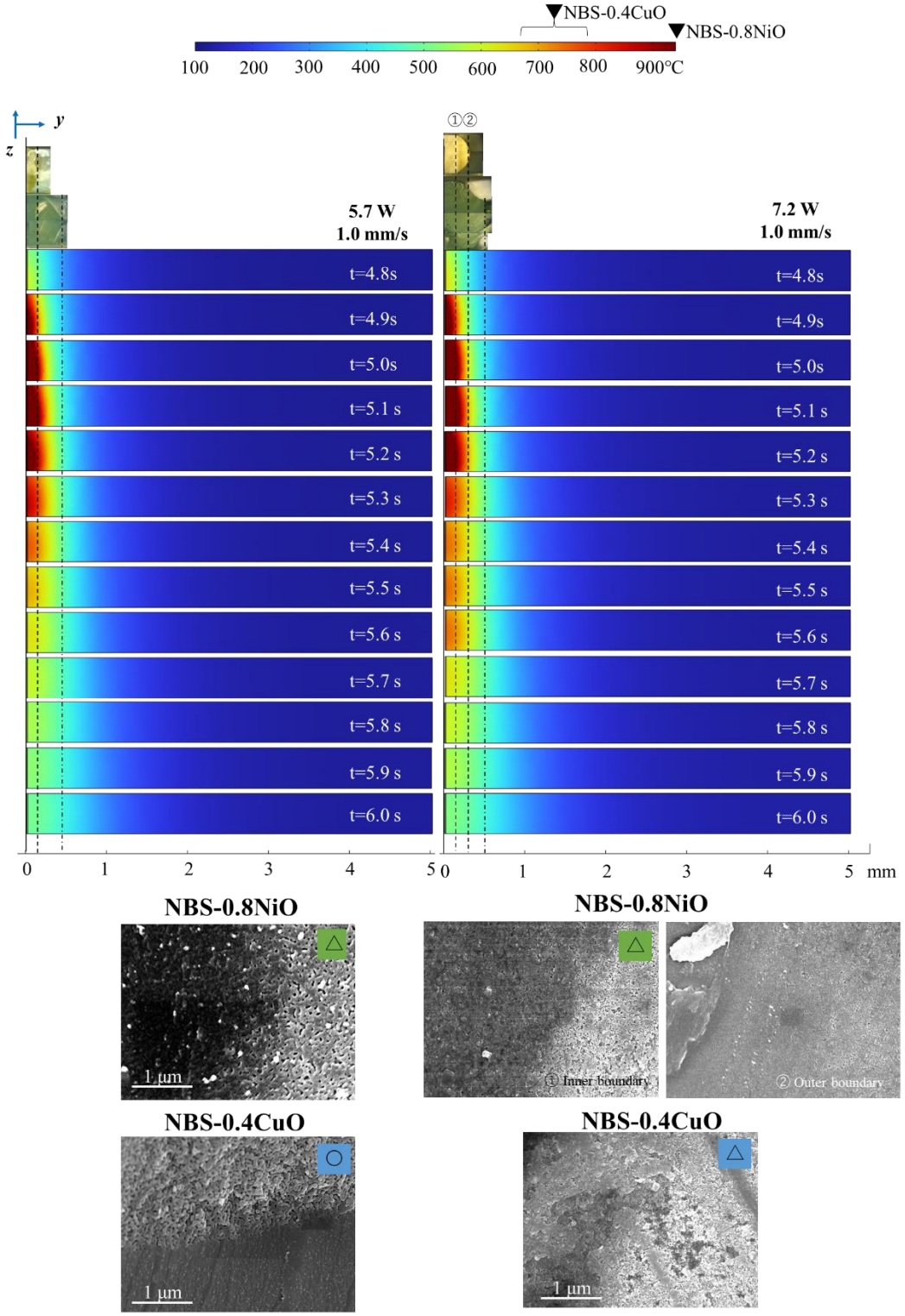

Figure 5.6 (a) Temperature distribution in y-z plane at x=0. The center of laser focal point pass by at t=5 seconds. The temperature above 940°C (homogenization temperature of NBS-0.8NiO) are plotted in same color (dark red). The vertical dot lines show the position where the boundary of TM ion remaining and washed away after acid leaching.

By increasing laser power from 4.3 W up to 5.7 and 7.2 W, heating duration above 940°C prolonged by 4 times. The boundary started to be blurred in NBS-0.8NiO.In NBS-0.4CuO, the laser affected line width started to significantly increase above 5.7 W. With 5.7 W, clear boundary was observed in the horizontal direction to laser incident due to highly expanded laser affected volume at the middle of sample thickness.

Figure 5.7 shows the temperature profile before and after laser focal point is approached at x=0 and z=-0.3 The temperature profiles were plotted every 0.02 second for 1.0mm/s and 0.5 mm/s, and 0.2 second for 0.1 mm/s. The temperature changing behavior was different in heating and cooling process. In the heating process, the temperature increment was fastest, and the increment rate became slower as distance from focal point increased. On the other hand, cooling process of 1.0 mm/s and 0.5 mm/s showed different behavior: while temperature is decreasing at focal point, the temperature keep increasing at about 0.6 mm away from focal point. Overall, the appearance of thermal history strongly depended on laser scanning speed. The accumulation temperature was different depending on both scanning speed and laser power.

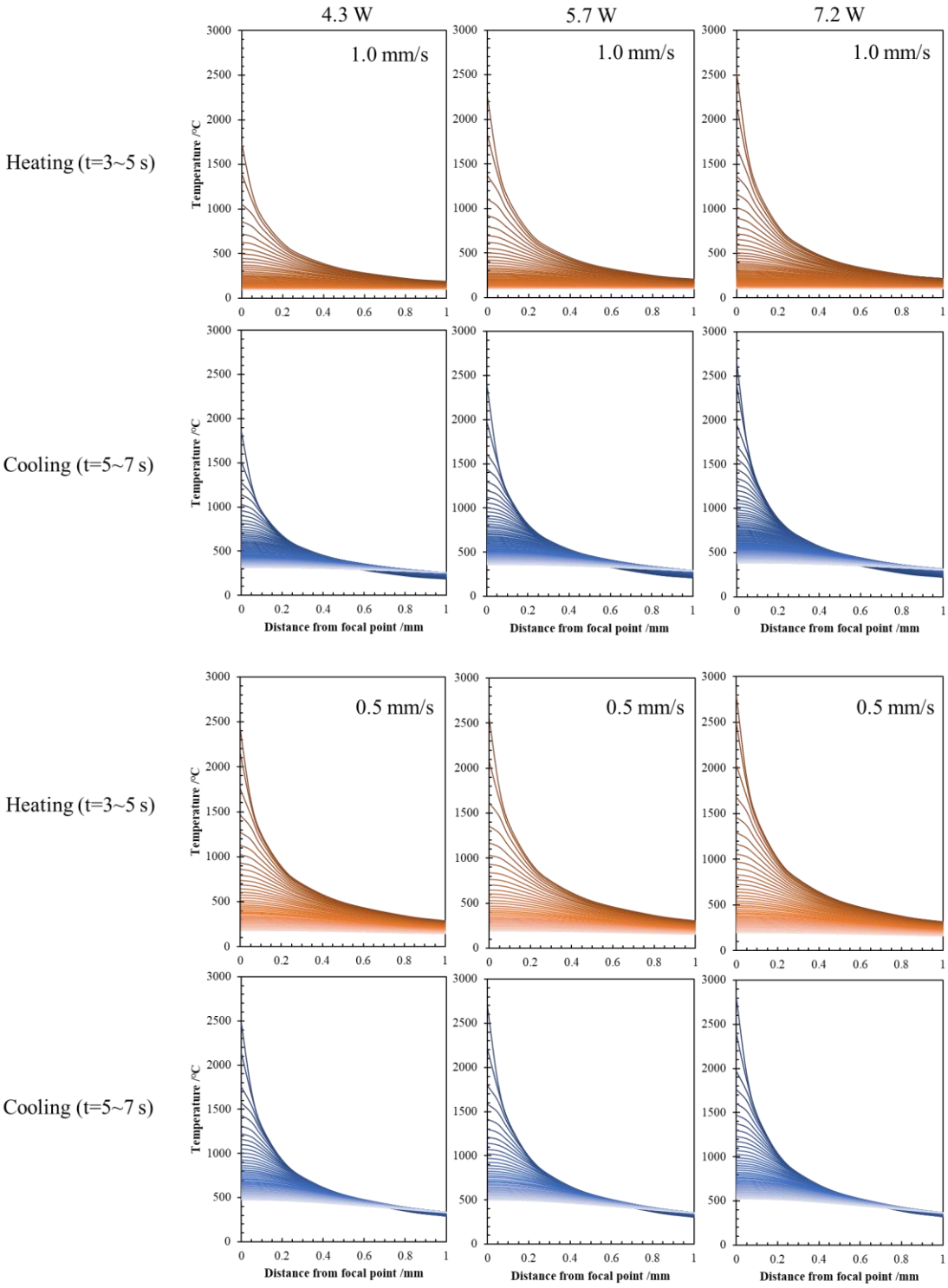
4.3 W
5.7 W
7.2 W
1.0 mm/s
0.5 mm/s
Heating (t=3~5 s)
Cooling (t=5~7 s)
Temperature /°C
Distance from focal point /mm

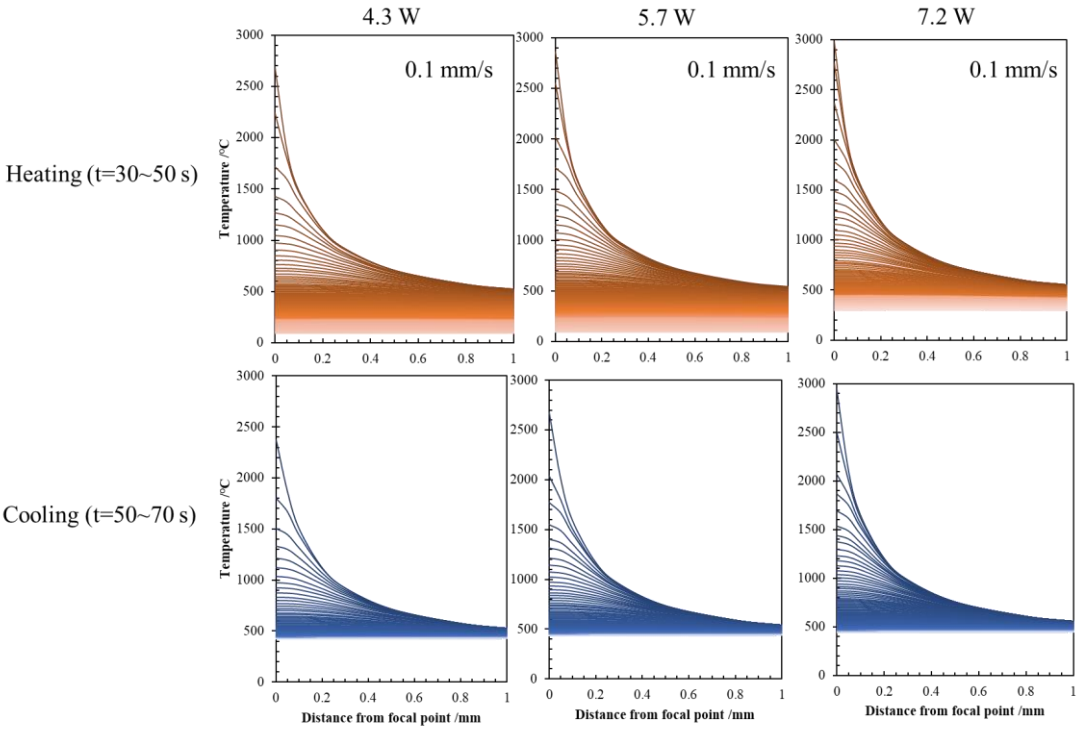

Figure 5.7 Temperature profile when laser focal point is approaching (heating) and passing by (cooling) at canter of top surface (0, 0, 0) in laser absorbing media. The plot was shown 0.02 seconds each for 1.0 mm/s and 0.5 mm/s, and 0.2 seconds each for 0.1 mm/s.

5.4.3 The thermal history distribution at porous/ non-porous boundary

The temperature range where phase separation development was significant could be observed by time resolved high temperature in-situ SAXS measurement during cooling process from homogeneous melt as shown in **Figure 4.11**. The phase separation development behavior was different depending on cooling rate, though the immiscibility always started to appear from 940°C in NBS-0.8NiO glass. The phase separation development rate was different depending on the temperature range below 940°C: from 940°C to 810°C, the increase rate of L_{corr} was relatively slow and this phase separation was considered to be due to nucleation growth scheme in binodal (droplet) development. From 810°C to 600°C, the increase rate of L_{corr} was much faster and considered to be spinodal development, caused by amplification of fluctuation. On the other hand, NBS-0.4CuO showed different phase separation temperature depending on cooling rate. In average, the homogenization started around 800°C and development behavior changed below 600°C, then the growth mostly stopped at 500°C.

In **Figure 5.8**, the cooling rate in respective temperature range was calculated at each

point and plotted as maps. In addition, the heating duration above homogenization temperature (940°C for NBS-0.8NiO and 800°C for NBS-0.4CuO) was calculated and plotted below the cooling rate maps. The cross-section images of laser irradiated sample are shown together and their porous/ non-porous boundary location is marked by dot line in vertical direction.

Most of these boundary lines in NBS-0.8NiO glass matched to the edge of the region where temperature increased above 940°C. The laser scanning with 0.1 mm/s showed 2 different boundaries from microscopic observation; inner boundary was not apparent in optical microscope, but SEM image showed distinctive color gap with straight boundary, marked in red dot line. The outer boundary, where color change was observed in optical microscope, matched to the edge of the region heated above 940°C. The cooling rate was always faster from in higher temperature range. Contrary, the boundary position in NBS-0.4CuO glass could not be reproduced by the mapping of region where temperature was heated above 800°C. The color-remaining volume was much larger compared to the region where temperature was heated up to 500~600°C, as shown in cooling rate map in 600~500°C.

Phase separation development was faster and most significant in temperature range around 600°C. This is probably due to relatively low viscosity with high composition contrast in phase separation dome. Although, cooling rate slow downed as temperature decreases. **Table 5.2** shows the calculated cooling rate and heating duration above homogenization temperature at the point where porous/ non-porous boundary was observed in the fabricated sample. The laser irradiation condition which could fabricate clear porous/ nonporous boundary was colored in red. When the porous structure gradually appeared and the boundary was ambiguous, the results are colored in blue. There was distinctive difference in cooling rate between the laser irradiation condition which could and could not fabricate the clear boundary in NBS-0.8NiO. When the cooling rate in the range of 810~600°C is faster than 16800°C/min, the clear boundary was successfully observed. On the other hand, duration above homogenization temperature was not affecting the possibility of clear boundary formation. This result suggests that 0.05 second was enough to make phase separated glass to be homogenized, with temperature increasing up to 1000 to 2000°C. Considering that phase separation never shows homogenization below homogenization temperature, enough fast cooling rate at the point temperature reaches above homogenization temperature could realize the porous/ non-porous boundary.

The laser irradiation with 5.7 W and 0.5 mm/s apparently fulfill the requirement for clear boundary formation. Although, the crack between porous/ non-porous was

dominant and difficult to evaluate. The fragility is another factor which should be taken account to fabricate the porous / non-porous glass substrate for microreactor. Apparently, NBS-0.8NiO showed higher fragility due to cracks generated at surrounding of the homogenized volume, due to narrower width by laser irradiation.

1.0 mm/s

NBS-0.8NiO	4.3 W	5.7 W	7.2 W
Cross section images	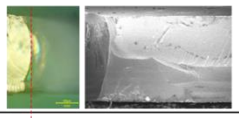	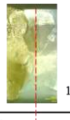	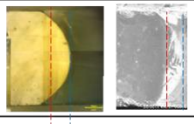
Cooling rate /940-600°C	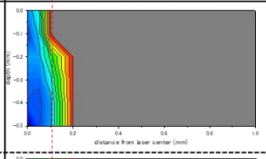	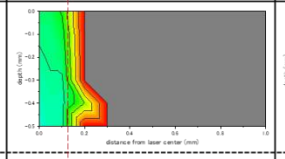	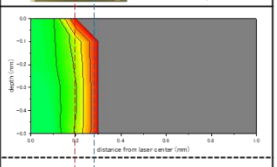
Cooling rate /810-600°C	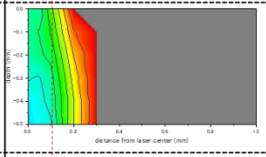	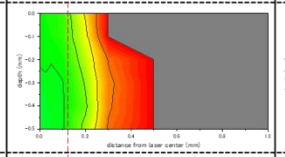	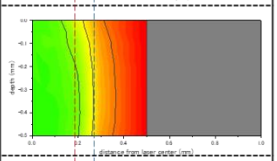
hold time above 940°C	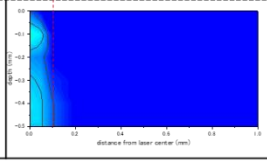	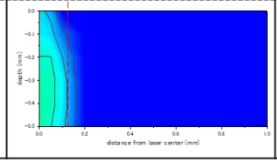	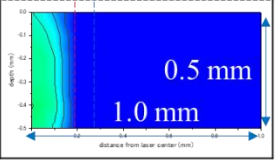

NBS-0.4CuO	4.3 W	5.7 W	7.2W
Cross section images	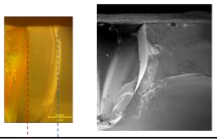	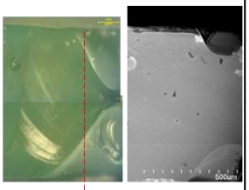	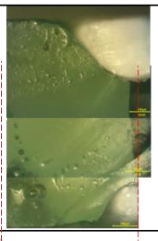
Cooling rate /800-500°C	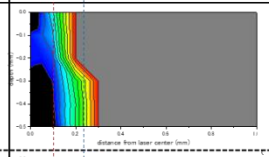	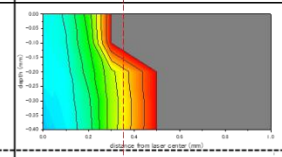	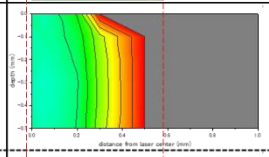
Cooling rate /600-500°C	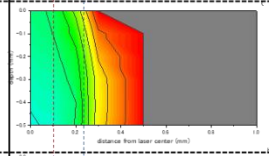	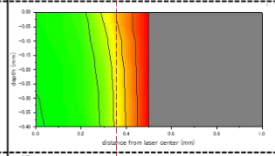	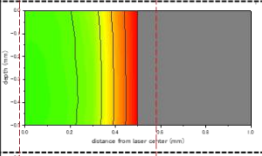
hold time above 800°C	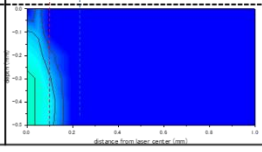	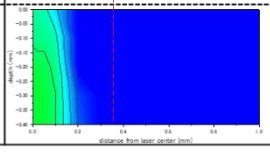	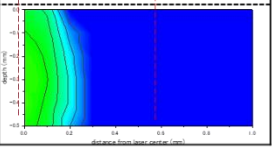

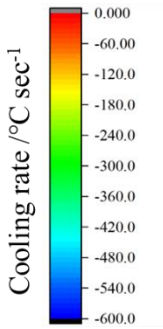

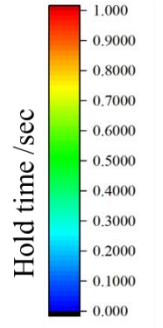

0.5 mm/s

NBS-0.8NiO	4.3 W	5.7 W	7.2 W
Cross section images	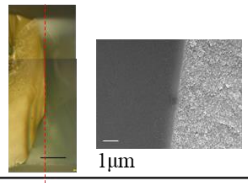	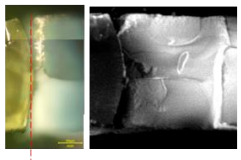	
Cooling rate /940-600°C	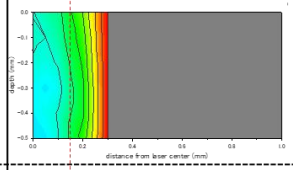	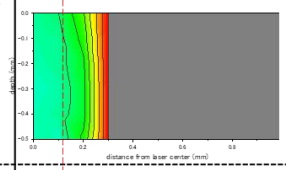	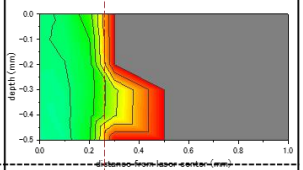
Cooling rate /810-600°C	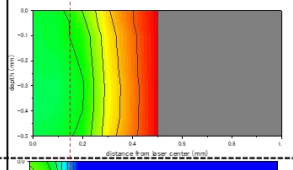	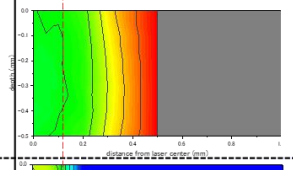	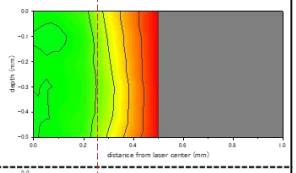
hold time above 940°C	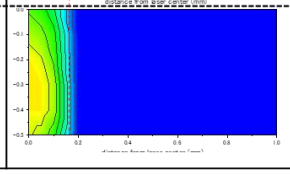	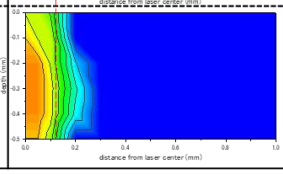	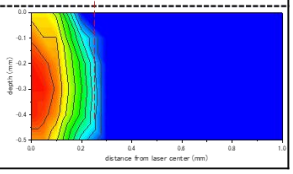

NBS-0.4CuO	4.3 W	5.7 W
Cross section images	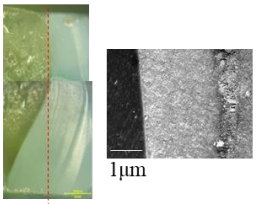	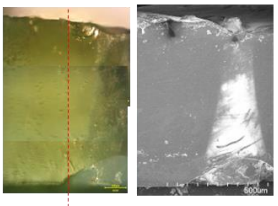
Cooling rate /800-500°C	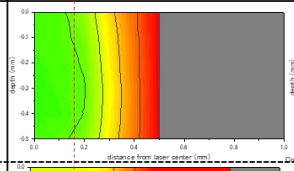	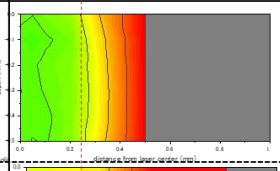
Cooling rate /600-500°C	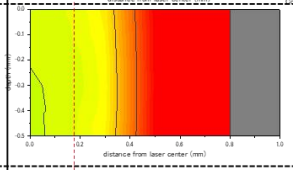	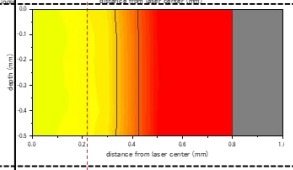
hold time above 800°C	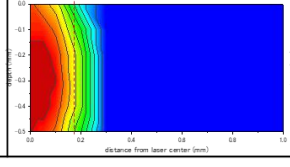	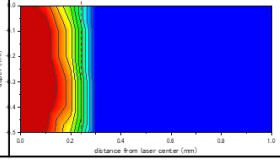

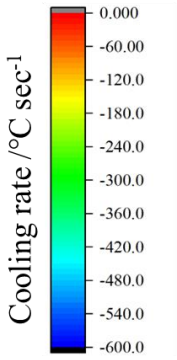

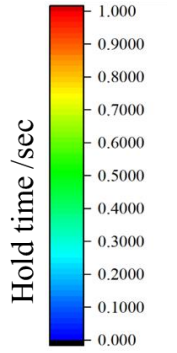

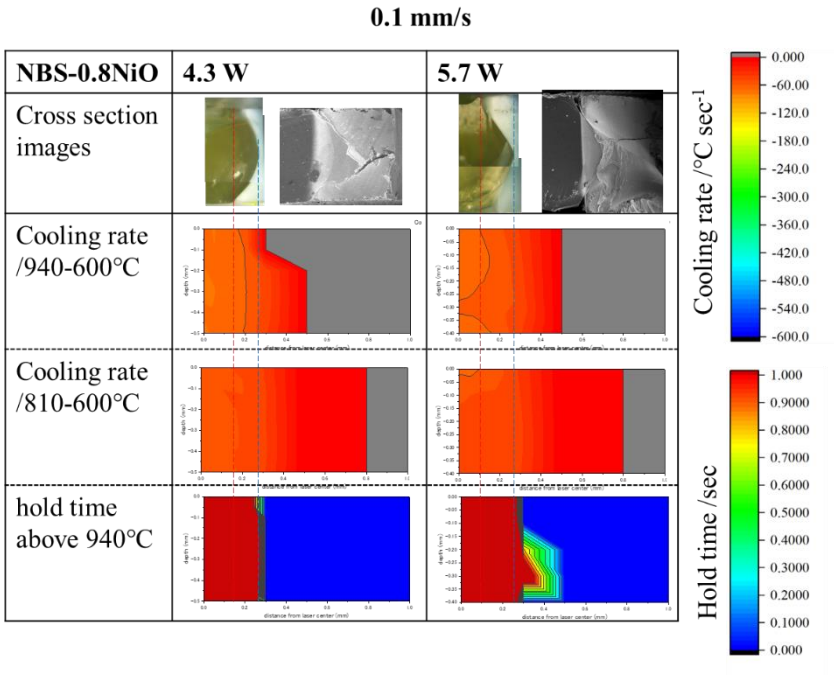

Figure 5.8 Spatial distribution of cooling rate and heating time inside the glass substrate.

Table 5.2 Simulated value of cooling rate and heating duration above homogenization temperature at porous/ non-porous boundary

NBS-0.8NiO	4.3W	Simulated values			5.7W	Simulated values			7.2W	Simulated values		
	Boundary position /mm from center	Cooling rate 940~810°C /°C/min	Cooling rate 810~600°C /°C/min	Hold time above 940°C /sec	Boundary position /mm from center	Cooling rate 940~810°C /°C/min	Cooling rate 810~600°C /°C/min	Hold time above 940°C /sec	Boundary position /mm from center	Cooling rate 940~810°C /°C/min	Cooling rate 810~600°C /°C/min	Hold time above 940°C /sec
1.0 mm/s	0.1	27000	21600	0.05	0.12	24000	16800	0.2	0.16	14400	14400	0.2
0.5mm/s	0.17	21600	18000	0.3	0.11*	21600	18000	0.7	0.28	9000	10800	0.2
0.1mm/s	0.15	4800	1800	>1	0.1	4200	1200	>1	-	-	-	-

*The crack between porous/ non-porous region was dominant

NBS-0.4CuO	4.3W	Simulated values			5.7W	Simulated values			7.2W	Simulated values		
	Boundary position /mm from center	Cooling rate 800~600°C /°C/min	Cooling rate 600~500°C /°C/min	Hold time above 800°C /sec	Boundary position /mm from center	Cooling rate 800~600°C /°C/min	Cooling rate 600~500°C /°C/min	Hold time above 800°C /sec	Boundary position /mm from center	Cooling rate 800~600°C /°C/min	Cooling rate 600~500°C /°C/min	Hold time above 800°C /sec
1.0 mm/s	0.1	32400	25200	0.25	0.36	4800	4800	0	0.78	0	0	0
0.5mm/s	0.18	14400	9000	0.7	0.24	10800	9000	0.5	-	-	-	-

5.5 Discussion

5.5.1 Validity consideration on material properties in calculation

In order to take into account unmeasured physical properties and their temperature dependence in the calculations, data on glasses with similar properties were cited from the literatures. This section will examine the validity of the approximations used in this study by considering the effect of each property value on the thermal history of the laser heating on glass.

Density was actually measured twice in NBS-0.8NiO glass using a pycnometer. The obtained value was 2219±58 kg/m^3. For NBS-0.4CuO was 2326±80 kg/m^3. When measuring NBS without additive TM ion with same method, the density was 2203±36 kg/m^3. and the reference 2147 kg/cm^3. The measurement might have overestimated the density by 2.6 %. In addition, the density decreases at high temperature due to thermal expansion. The NBS-0.8NiO glass has CTE=3.48×10^{-6} /K below Tg and the expansion rate further increase at higher temperature. The decrease of density below Tg is less significant: about 0.5 % decrease at 500°C. Though further difference is expected in the melt. From the reference, the density of the glass composition 7 Na_2O-25 B_2O_3-68 SiO_2 was 2054 kg/m^3 at 1500°C [147] decreasing 7.6 % from the room temperature density of 2203 kg/m^3. Considering measurement error and temperature dependence, the density would be varied within 10 %. When temperature is calculated with ρ=2147 kg/m^3, laser irradiation with P=4.2 W, v=1.0 mm/s resulted in about 600°C lower accumulation temperature and 50 μm narrower region of homogenization. The temperature dependence of density should be considered in the calculation appropriately for higher accuracy.

The temperature dependence of heat capacity has been measured in a variety of glass systems. Borosilicate glass the SiO_2/B_2O_3 ratio has a strong influence on the heat capacity, especially above the melt [152]. In the borosilicate glass containing 15 Na_2O-10 CaO, the heat capacity hardly changes with compositional change when the amount of B_2O_3 is more than SiO_2, but the heat capacity begins to decrease as the ratio of SiO_2 increases above K = SiO_2/B_2O_3 = 0.5 [153]. In this study, the temperature dependent-heat capacity data of Pyrex glass (R=0.5, K=7.6) measured by Richet et al. was sued in the calculation. In the report, there were few differences in heat capacity value of Pyrex and BB glass (R=0.1, K=3.9). The Tg of Pyrex glass was 598°C, which was about 120°C higher than the apparent Tg of target glasses (NBS-0.8NiO and NBS-0.4CuO) in this study. Since the heat capacity value significantly increase at Tg. Although phase separated glass has two compositions with distinctively different thermal properties (SiO_2: 1200°C, 20Na_2O-80B_2O_3: 450°C), and the DTA measurement in chapter 1

showed too ambiguous curve to find critical Tg point. The calculated thermal history at the temperatures before and after Tg should be considered with caution. The homogenization temperature, which was dominant temperature to decide the porous/ non-porous boundary, was enough higher

Thermal conductivity due to heat conduction due to phonon (Lattice vibration) and photon (Radiation) effect is difficult to distinguish in the measurement value. Hence, the appeared in equation (5.2) can be expressed as following :

$$k = D\rho C_p = \frac{1}{3} C u_s l \tag{6.12}$$

Where D is the thermal diffusivity, ρ is the density of the material, C_p is the specific heat, C is the volumetric specific heat, u_s is the velocity of sound in the solid, and l is the mean free path of the phonon. The mean free path for phonons is limited by geometrical effects associated with the disordered nature of the structure. Below Tg, heat capacity Cp is defined only by configuration of the glass structure, so mean free path is expected to change with temperature in the same proportion as the specific heat. Therefore, considering equation (6.12), temperature dependence of thermal conductivity only depends on u_s, which may decrease as temperature increase [154].

There are few measurement data on the temperature dependence of emissivity. The composition dependence is poorly reported. It is difficult to measure the emissivity accurately because the radiation generated inside the glass is absorbed by surrounding volume of the glass. Emissivity shows temperature and wavelength dependence, and even varied by sample thickness[146]. Different temperature dependence of heat conductivity due to radiation was calculated depending on the visible color of the glass [103]. Specifically, the green glass showed lowest radiative conductivity and the radiative conductivity was 10 times smaller than window glass at 1400°C. Such differences of temperature dependence in material properties might have affected laser absorption behavior.

Laser absorbance was highly dominant parameter on deciding accumulation temperature. The absorbance of 1064 nm light was similar for both NBS-0.8NiO and NBS-0.4CuO at room temperature. Although above laser irradiation with 5.7 W, NBS-0.4CuO showed much wider laser affected volume and this region could not be reproduced by FE calculation. There are two possible reasons for this mismatch: different laser absorbance or radiative heat transfer. From **Figure 5.4**, the absorption of wavelength of 1064 nm is located at shoulder of main absorption band ion. This band might show strong temperature dependence, especially when Cu^{2+} ion is in borate phase [102]. Ni^{2+} ion speciation also shows temperature dependence, though the absorption

band containing 1064 nm appeared to be dependent of coordination. Such a difference in temperature dependence of laser absorption behavior would significantly affect the temperature profile. Although, NBS-0.4CuO was difficult to evaluate how to obtain clear porous/ non-porous boundary. This may be due to inaccuracy of temperature calculation result. For further improvement, temperature dependence of laser absorbance should be considered to obtain the thermal history distribution in higher accuracy.

The spectral absorption coefficient κ to express radiative heat transfer was less significant to the highest accumulation temperature and thermal history, by varying from 2 to 500 cm^{-1}. It would show spectral dependence especially 0.8 to 4.0 μm where the wavelength region where radiation intensity develops in high temperature[151]. Further consideration is necessary to evaluate the dominance of this factor and its reliable value.

5.5.2 Mechanism of porous/ non-porous clear boundary by laser irradiation

The temperature at the boundary between phase separation and homogeneity is clearly defined as illustrated in **Figure 1.1**. It could be observed by time-resolved in-situ SAXS measurement, by showing exactly same temperature to start phase separation from homogeneous melt. Such distinctive boundary temperature to show different glass state might be one of the reasons why the clear boundary between porous/ non-porous volume could be observed. In addition, the cooling process after laser scanning enabled the glass to pass through the significant phase separation development range as quickly as possible. Since the NBS glass shows metastability with phase separated state under room temperature, it was difficult to obtain homogeneous bulk glass. Quenching of the melt to obtain homogeneous glass often crash the bulk glass due to different cooling rate at surface and inner side. Quenching by twin roller is also limits sample shape to thin flakes. Afterall, partial laser heating on glass plate was possible to maintain a stable phase at high temperatures at room temperature, on the glass plate without major collapse.

The transformation from phase-separated to homogeneous state during heating was dominated by the diffusion of chemical components, similarly to dissolution of quartz in the glass melt as discussed in chapter 4. CW laser irradiation with heat source of TM ion bearing in the glass was able to heat the glass substrate sufficiently higher than homogenization temperature in the phase-separated glass substrate from the top surface to the bottom. In addition, rapid heating by laser irradiation might have avoided further

phase separation development before the glass is homogenized and realized homogenization in short heating duration time.

The FE calculation revealed the two major questions on the structural change by laser irradiation. The first question is how the clear boundary between porous/non-porous region by laser irradiation. From the calculation results, the volume where temperature increased above homogenization temperature and actually homogenized regions were well matched. At this boundary, the cooling rate was faster than certain value. This cooling rate is equivalent to water quenching or steel plate quenching [129] on the glass melt. With laser processing, the shape of the glass. When the cooling rate is slower, gradually distributed phases with various morphology. Such requirement could be sufficiently fulfilled by either NBS-0.8NiO and NBS-0.4CuO, even though each composition had different temperature dependence on their material properties including phase separation behavior, light absorption spectra, density, and so on. The important factor to realize the porous/ non-porous boundary was the accumulation temperature by laser irradiation and the enough-fast cooling rate at the location of homogenization limit. In practical, thickness of the sample will change the temperature profile and its spatial distribution. The accurate validation will enable prediction when changing parameters in material processing.

The second question was the reason why the cross section of homogenized volume was barrel-like shape. Usually when the laser absorption is only due to Lambert-Beer law, the photon absorption decays as the depth become deeper. In order to maximize the absorption width in the center of glass plate, laser absorption behavior would have to be considered carefully. The effect of radiation was reflected in the absorption coefficient of the laser, taking into account that the radiation coefficient of the glass is high, and that the laser intensity propagated to the deep inside the glass plate due to the high transmittance of the glass for the laser wavelength of 1064 nm. In addition, low thermal conductivity by phonon propagation in the glass at low temperature might have hold back the heat in the limited volume, helped to show sharp temperature distribution at surrounding of the focal point.

5.5.3 The dominance of heat generated by respective source

The most significant factor on the calculated temperature was temperature dependence of laser absorbance. Laser absorbance determines the amount of energy to be used for temperature increment, and also temperature distribution along laser incident direction. In this study, temperature dependence of laser absorbance was given based on radiative emission at high temperature. The temperature dependence of laser

absorbance could reproduce the formation of barrel-like laser affected volume observed in cross section of laser irradiated samples, the widest laser affected volume in middle of the glass substrate. Temperature dependent model of laser absorbance given in this study is assumption was one of the ways to show barrel-like temperature distribution, but it shows less dependence on additive atomic species. And even more, emissivity used in the calculation was not accounted to show wavelength and temperature dependence as shown in equation. (5.4). For further improvement in the calculation, direct measurement on laser absorbance of the glass under high temperature is necessary. The difficulty in such a measurement is effect of radiative emission at high temperature and temperature change due to laser absorption. It is important to prepare the setup with appropriate light source for absorbance measurement.

The laser absorption behavior was significantly different depending on additive transition metal ion, even though Ni^{2+} and Cu^{2+} ion showed similar absorption coefficient for 1064 nm at room temperature. The results suggest two possible causes for much wider affected volume for Cu^{2+} ion. One is different temperature dependence of phase separation behavior as shown in chapter 4, and the another is different temperature dependence of respective transition metal ion. Temperature dependence of absorption coefficient would affect both laser absorption behavior and radiative heat transfer inside the glass. As shown in chapter 3, Ni^{2+} ion showed significant coordination change when the glass is transferred from phase separated to homogeneous glass. Although, it showed less significant change in absorbance for 1064 nm, which is located at absorption band of ^3F-$^3T_2$ transition. This transition is less significant against major band and the similar absorption band is available in 5-coordinated Ni^{2+} ion. Contrary, absorbance of 1064 nm in Cu^{2+} ion located in major absorption band and the temperature dependence of its peak position and intensity is reported [102]. Although it strongly depends on the composition of glass matrix, so measurement on specific composition focused in this study is necessary.

Another factor which was not accounted in the calculation was enthalpy change due to transformation from phase separated to homogenized glass. Considering phase-mixing enthalpy of borosilicate glass with similar composition, 8.7 Na_2O- 34.8 B_2O_3-56.5 SiO_2 has $\Delta_m H^{ex} = -6.25\ kJ/mol$ at 1050℃ [155]. Approximate heat generation through homogenization is -0.213 kJ/m^3, calculated with density: 2219 kg/m^3 and molar weight 65 g/mol. On the other hand, the heat given by laser irradiation with 1~0.5 mm/s is about 2~8 kJ/m^3. The heat due to miscibility change due to phase separation would have been negligible.

5.6 Summary

The thermal history distribution inside the glass substrate before and after laser irradiation was calculated based on heat transfer model including radiation by finite element method. In addition to temperature dependence of several material properties (heat capacity and emissivity), laser absorption due to radiative heat emission was also considered in the model.

In the glass with composition of NBS-0.8NiO, the thermal history distribution could reproduce the homogenized volume in the glass sample obtained in chapter 2. Considering the temperature of homogenization and phase separation development obtained from chapter 4, the cooling rate in the temperature range of significant phase separation development could be calculated. By comparing with the location of clear boundary between porous/ non-porous region, the cooling rate requirement for such boundary formation could be revealed. Although it was difficult to reproduce the results of glass composition of NBS-0.4CuO. Further improvement on simulation model is required, by considering temperature dependence of laser absorbance and emissivity.

Overall, the requirement for formation of clear boundary between porous/ non-porous structure in sodium borosilicate glass was fast enough cooling rate (18000 °C/min~) at the temperature range of active phase separation development at the location where highest temperature reaches above homogenization temperature. The location, or distance from laser focal point and laser penetration depth depends on the scanning speed and output power of the laser irradiation.

6 3D micro processing and microstructure control of silica glass by femtosecond laser irradiation

6.1 Introduction

Fused silica has outstanding physical characteristics, such as high transparency, low intrinsic loss and outstanding elastic properties for micromechanical devices. Thanks to the microfabrication technique based on femtosecond laser-induced selective etching [62], highly complex 3D micro-structures can be carved out of single glass substrate [95][63][93]. This manufacturing process brings great opportunities in the field of micro-devices such as MEMS, microfluidics system, and so on. One of the advantages of this fabrication process is its ability to combine, not only structural elements of various kinds, but also optical ones in a single monolith. This process circumvents the separating the bonded layers by mechanical damages such as repetitive vibration. Control of static and dynamic behavior of the entire MEMS structure takes an important role[156].

6.1.1 Vibrational damping function on silica glass cantilever by Acoustic Black Hole structure

Mechanical vibrations at the resonance may compromise the stability of a device, when it is undesired and uncontrolled as a result of extrinsic noise excitations. To broaden their usable frequency ranges, notably by reducing the vibration amplitude for a given set of frequencies, the concept of ‘acoustic black hole’ (ABH) was proposed [157][158]. There, it was shown that a plate with an acute angle wedge has less frequency dependence on vibrations [157][159]. In particular, it was theoretically proven that a wedge with a profile defined by a power law shows effective damping. V. V. Krylov demonstrated this effect experimentally with a ‘meter-sized’ steel plate [160]. This approach is particularly attractive in aeronautics and for automotive applications [161], as in both cases, excitations of resonant modes can have dramatic effects if undamped. Likewise, applying this method at the micro-scale will enable noise attenuation from resonant vibrations in various types of microsystems without the need for additional processing steps to add damping material.

Scaling ABH phenomenon down to the micro-scale is not just a matter of size, since slight inhomogeneity or defects of material as well as fabrication imperfections, most often negligible at meter-scale may have dramatic consequences at the micro-scale. Therefore, implementing ABH at the microscale requires a detailed analysis of the material properties after the fabrication process as well as high fabrication dimensional resolution and accuracy. While 3D microfabrication using femtosecond laser may

realize enough preciseness according to numerous optimization reports for irradiation conditions [92][162][91][163], the effects of the laser at the atomic-level are not fully understood as it is difficult to see the detailed gradation of material properties after writing complex patterns inside the material [164]. In addition, the effects on material properties, such as thermal expansion coefficient [84], Young's modulus [85][86] and density [87][88] *after* the etching process are not revealed.

6.1.2 Theory of Acoustic Black Hole effect

The followings are a brief review of the theoretical aspects behind the ABH phenomenon. Flexural waves in a beam are governed by the following equation:

$$\frac{\partial^2}{\partial x^2}\left(D(x)\frac{\partial^2 W}{\partial x^2}\right) - \omega^2 \rho h(x) W = 0 \tag{6.1}$$

where W stands for the displacement along the z-axis (see **Figure6.1**), ρ for the density of the material of the vibrating beam, ω for the angular frequency, and finally, $D(x)$ for the bending stiffness. The bending stiffness of the beam with a rectangular cross-section is further expressed as:

$$D(x) = \frac{Eh(x)}{12(1-\nu^2)} \tag{6.2}$$

$$h(x) = \begin{cases} \left(h_c - h_{Tip}\right)\left(\dfrac{x}{L_{Taper}}\right)^m + h_{Tip}, & 0 < x < L_{Taper} \\ h_c, & L_{Taper} < x < L_c \end{cases} \tag{6.3}$$

where E is Young's modulus, $h(x)$ is the thickness of cantilever at a position x along the beam, ν is the Poisson's ratio, and m is an exponent that defines the slenderness of the edge. In this experiment, cantilever with the tapering edge, which ABH effect can theoretically be obtained, was designed and fabricated. A solution of Eq. (6.1) can be expressed as follows:

$$W(x) = A(x)e^{i\Phi(x)} \tag{6.4}$$

where $A(x)$ is the displacement in each point of the beam and $\Phi(x)$ is the phase difference between the excitation wave and the propagating wave in the beam. In the case of a cantilever in vacuum, the local wavenumber k is further defined by:

$$k(x,\omega) = \left(\frac{12\rho(1-\nu^2)}{E}\right)^{\frac{1}{4}}\left(\frac{1}{\omega h(x)}\right)^{1/2} \tag{6.5}$$

In practice, it is difficult to achieve a zero thickness at the tip. To a certain extent, the beam edge is always truncated with a minimum tip thickness h_{Tip}. The phase increment $\phi(x)$ between 0 and x, writes:

$$\phi(x) = \int_0^x k(x)dx \tag{6.6}$$

For a coefficient $m \geq 2$ (see Eq. (6.3)), the phase difference increment diverges as x increases. This means that a flexural wave propagating in the beam never reaches the edge[159]. As the energy is dissipated through dynamic deformation, a phase difference between stress and strain is observed. In such a case, the Young's modulus is expressed in a complex form: $E^* = E_0(1 - i\eta_0)$. Consequently, the reflection coefficient R will decrease and result in an ABH effect.

$$R = \exp\left(-2\int_0^x Im\, k(x)dx\right) \tag{6.7}$$

where $Im\, k = \frac{1}{4\eta_0} Re\, k$ and η_0 is the intrinsic loss factor of the material.

The ABH theory assumes that the wave fully propagates towards the edge, without partial reflection. This assumption is valid for a slowly varying thickness profile at the tip of the cantilever. In practice, fabricating such slender profiles are difficult to achieve at the microscale with conventional manufacturing processes, such as lithographic ones, as this design is intrinsically three-dimensional. To overcome this challenge, we took advantage of the femtosecond laser micromachining of glass substrates. The design of the silica glass cantilever is shown in **Figure. 6.1**.

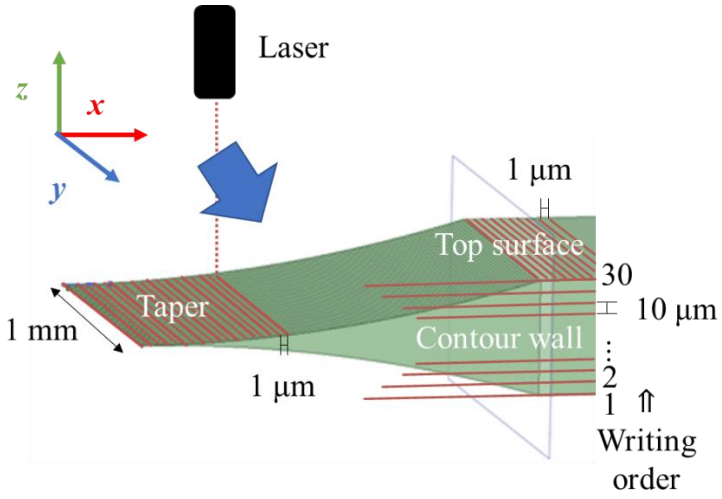

Figure 6.1 Dimension of cantilever and position inside silica glass substrate. Laser irradiated surface in red line and actual surface in green line.

Based on Eq. (6.3), (6.5), and (6.7), the increase of m seems to be the most efficient way to have a greater attenuation effect. A larger m in the profile function generates an abrupt change in the thickness at the start point of ABH design. In our design, m = 2 is

chosen and we assume that the obtained geometrical profile has enough smoothness to avoid counter-propagating waves at the boundary between the tapered and the flat part. In such conditions, the design is fulfilling the normalized wavenumber variation given in [165] :

$$\frac{dk}{dx}\frac{1}{k^2} \ll 1 \tag{8}$$

This criterion indicates that the change in wavenumber must be smaller over distances comparable to the wavelength. In this way, the incident wave fully propagates toward the tip of the cantilever without loss at the beginning of the tapered section of the profile.

6.2 Experimental

6.2.1 Cantilever fabrication

The principle is to sequentially use a non-ablative femtosecond exposure process and a chemical etching step [166] [50]. The cantilever were fabricated out of a 500 µm-thick silica substrate (Corning 7980-0F). The substrate contains 1000-ppm OH and traces of Cl in the order of 100 ppm (Class-III fused silica). For femtosecond laser irradiation, we used a Yb-fiber amplifier (λ=1030 nm) emitting at a rate of 800 kHz, 230 nJ pulses of duration 270 fs. Scanning velocity was 10 mm/s (corresponding to 80 pulses deposited in 1 µm distance along the writing direction). The polarization was always set perpendicular to the writing direction. To focus the laser beam, we used an objective with a numerical aperture of 0.4. The focal spot volume has an approximated ellipsoidal shape with a short axis width of 1.6 µm, and 10 µm for the long axis, oriented toward the beam optical propagation axis (i.e. the *z*-axis direction) [166]. The contour of the cantilever was defined with a set of adjacent straight lines, as shown in **Figure 6.2**. Spacing between lines was 1 µm in the *x*-axis direction and 10 µm along the *z*-axis direction. Those distances were optimized for efficient etching [162]. After exposure, the specimen is immersed in a low-concentration HF bath (2.5 %) until all the previously exposed volume dissolved, and the surrounding bulk falls off. Soak time was about 10 hours for cantilever without tapered profile and 40 hours for the one with a tapered end.

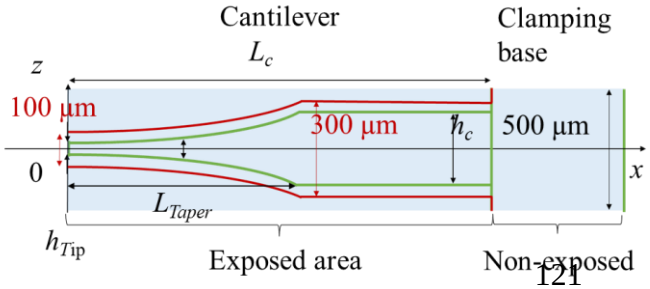

Figure 6.2 Schematic illustration of laser scanning process to picked out the tapered cantilever of the silica glass substrate.

6.2.2 Vibration tests

The resonant frequency can be expressed as function of material constants. In the case of a planar cantilever without tapered end, the resonant frequency f_n writes:

$$f_n = \frac{1}{2\pi}\beta_n{}^2 \frac{h}{L^2}\sqrt{\frac{E}{12\rho}} \tag{6.9}$$

where n is the vibration order for a given mode n, β_n is a constant depending on the mode, h and L are thickness and length of the cantilever, respectively, E is the Young's modulus, and ρ is the density of the cantilever material. In the case of the cantilever with a taper design, the resonant frequency cannot simply be obtained from the analytical formula of Eq. (6.9), but rather through simulation.

Here we focused on the first mode of vibration for each cantilevers. A triangulation laser sensor (Keyence LK-H022K) was used to measure the cantilever tip deflections at a sampling frequency of 50 kHz. The cantilevers were set on a plate itself mounted on a piezoelectric actuator (Noliac, NAC2003). An AC voltage of 100 mVpp was applied to the actuator, and its frequency was swept from 2000 to 3700 Hz for n = 1 (primary mode) in Eq. (9). The dynamic behavior of the cantilever with a tapered-end at the resonant frequency was simulated by the Finite Element Method using COMSOL® using the measured dimensional parameters of the actual, fabricated cantilevers, and compared with the experimental values. In our simulations and calculations, the relevant material constants were E = 72.5 GPa, ρ = 2201 kg/m^3, and ν = 0.17.

Ring down measurements consisting of exciting the cantilever to its resonant frequency and subsequently turning off the vibration source, followed by monitoring vibration amplitude decay were performed to further evaluate the vibration damping behaviors. The measurement of the decay time provides an estimate of the ABH-induced attenuation. The amplitude decay curves showed a single exponential decay in early stage.

6.2.3 Static properties observation of the cantilever after processing

Surface profile h(x) of the fabricated cantilever was measured by a stylus profiler (Dektak) to evaluate the precision of the micromachining. The stylus radius was set to 12.5 μm and scan speed was 0.133 μm/s. The center of the cantilever was scanned along the x-axis. The front and backside were measured separately. The measured profile of the tapered part was fit by a function of h(x)=ax m+b, where a is a proportional constant of the power function, m is the exponent of fit function. As a pre-programmed design, m

= 2 for all designs.

The surface roughness of the cantilever surface was observed and measured by a laser microscope (VK-8510, Keyence Corporation). Roughness was evaluated using the Arithmetical mean deviation Ra value of the horizontal and vertical direction of the cantilever.

Fourier transform infrared (FTIR) reflection spectra for the sample surface were measured at room temperature in the wavenumber range 600-4500 cm-1 by a micro-FTIR spectrometer (JASCO, FT/IR-6100, IRT-5000). The aperture size was 50 μm×50 μm and resolution was 4 cm^{-1}. Spectra were obtained from 3 different cantilevers.

6.3 Results

6.3.1 Glass cantilever fabrication

The thickness of tip at the end of cantilever hTip and flat part hc were measured by observing the cross section in an optical microscope. The thickness profile of the tapered cantilever was fit with the Least-square method to compare the profile function of the exposed pattern with the end-product, i.e. the fabricated cantilever. Results are shown in Table 1. Tapered part thickness was designed to decrease quadratic function (m = 2). All cantilevers had almost the same thickness at the tip and flat part, and m value after fitting was found in the range of 1.86~2.01. The change of thickness at the base (Non-exposed) before and after etching, was less than 10 μm. The profile result shows a good agreement of the surface profile between the design and the fabricated cantilever. The typical thickness h_{Tip} and h_c were always about 25 μm smaller than the laser-irradiated line for all samples, regardless of the etching time.

To check the quality of the surface smoothness, the roughness of the cantilever surface was observed. The bottom of **Figure 6.3** shows the optical microscope images of the sample surface. In the laser exposed area, the periodic texture is similar to a texture reported in [93]. In contrast, the non-exposed area showed a clear flat surface. **Table 6.2** shows the Ra of the flat part of the cantilever (laser-exposed), and the base part of the sample (unexposed) respectively. These values were in good agreement with microscopic image in Fig. 3, showing that the exposed surface has rough surface due to laser exposure even after etching.

Table 6.2 Typical values of the surface roughness R_a (in μm) measured on the cantilever.

	Non-exposed	Exposed

Along x-axis (50 µm)	0.02	0.097
Along y-axis (50 µm)		0.107

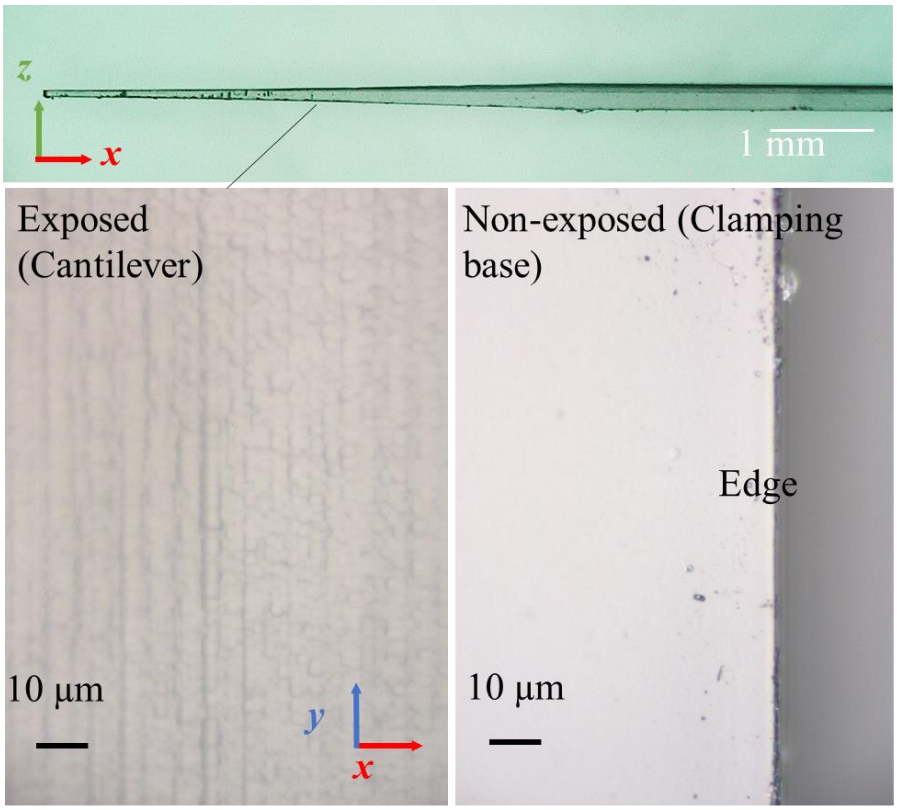

Figure 6.3 Appearance of the fabricated cantilever with tapering. Top: Side view of fabricated cantilever (L_{Taper}=5 mm), Bottom: Microscopic photographs of laser exposed surface (left) and non-exposed one (right) of cantilever.

6.3.2 Vibration test on cantilever

The resonant frequency was measured and compared with the simulation results. The results are shown in **Figure 6.4.** The calculated values are the frequencies of the primary vibration mode (n = 1 in Eq. (6.9)), which corresponds to a deflection aligned along the z-axis, with a static-node at the fixed end. The dependence of L_{Taper} on the resonant frequency showed the same trends in both experimentally measured and simulated values. The simulations with three different models were done in order to find out the most effective parameters affecting the values of the resonant frequency.

The first model, shown with a smooth line in **Figure 6.4**, had average dimensions among fabricated cantilever as follow: h_{Tip} = 55 µm, h_c = 250 µm and m = 2 (Model A1).

To account for the error due to the profile function change during the fabrication process, m = 1.8 with the same dimension (Model A2) was also simulated. The resonant frequency difference between these 2 models was within 4%, which is smaller compared to the difference between the simulated frequencies of two models (Model A1 and A2) and their experimental values. The experimental frequency was 3~10 % lower

L_{Taper} /mm	h_{Tip} /μm	h_c /μm	m
0	-	250	-
3.33	54.2±1.0	251±1	1.86
5.00	53.9±0.8	250±3	2.00
5.65	56.1±0.4	249±2	1.99
8.57	58.8±0.8	252±1	2.01

compared to simulation. Model B with the dimensions shown in **Table 6.1** were plotted with asterisk mark for L_{Taper} = 3.3, 5.0, 5.7, 8.6. Although, the fabricated Model B had more accurate dimensions compared to the desired profile, the resonant frequency was still estimated higher compared to its experimental value.

Table 6.1 Measured dimensions of the fabricated cantilevers with different L_{Taper}.

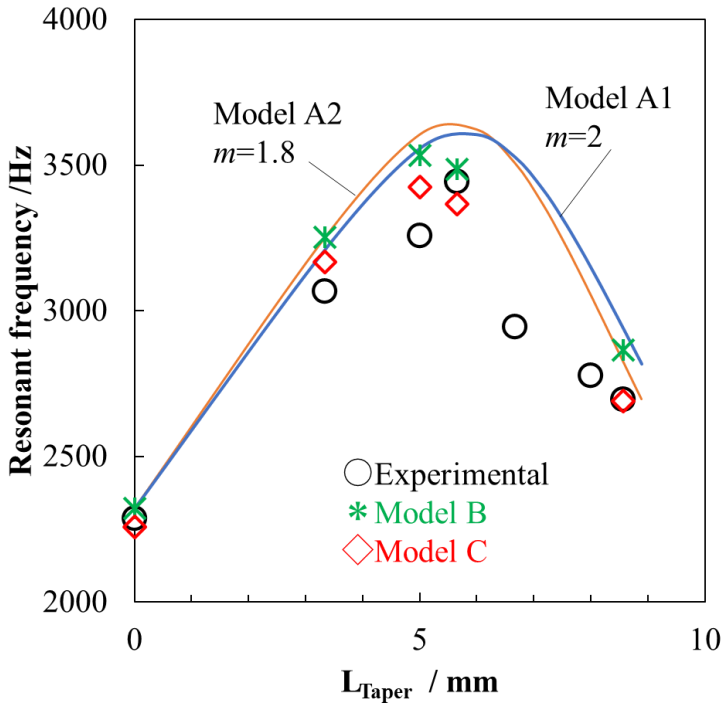

Figure 6.4 Experimental and simulated resonant frequency of each cantilever with various taper length. Model A1, A2 show simulation results using average cantilever dimensions with

different function parameter *m*. Model B is simulated with the measured dimensions for each cantilever with uniform Young's modulus. Model C shows the simulation results on the cantilever with lower Young's modulus surface layers of $E_{surface}$=60 GPa of 10 μm thickness.

Figure 6.5 shows the results of the vibration test for a tapered (L_{Taper}=5.0 mm) and a non-tapered cantilever, respectively. **(a)** is the Fourier transformed spectrum of the amplitude obtained by the frequency sweep test. The frequency is normalized with the resonant frequency f_0. The tapered cantilever shows a broader resonant peak; The FWHM of each resonant peak was 1.5 Hz ($\Delta f/f_0 = 4.6 \times 10^{-4}$) for tapered cantilever and 0.8 Hz ($\Delta f/f_0 = 3.5 \times 10^{-4}$) for cantilever without taper. This means the cantilever amplitude had a lower resonant frequency dependence.

Figure 6.5 (b) shows the typical result of ring down measurement. The deflection amplitude decay after the resonant vibration of the non-tapered cantilever and the tapered cantilever (L_{Taper}= 5 mm), respectively. The cantilever with an ABH effect attenuated over a shorter period compared to the non-tapered one. The tapered cantilever showed a damping effect without any additive absorbing material, demonstrating the concept of ABH. A fitting function $\mathrm{A} \cdot e^{-\pi \frac{f_1}{Q} t}$ was applied on the decay curves to extract the *Q* factor, which indicates the acuity of a resonant vibration peak. The *Q* factors obtained for each cantilever with different L_{Taper} (0~ 8.6 mm) are plotted in **Figure 6.6**. The *Q* factor decreases as the tapered length gets longer, which shows an increase of attenuation efficiency with a larger proportion of ABH design.

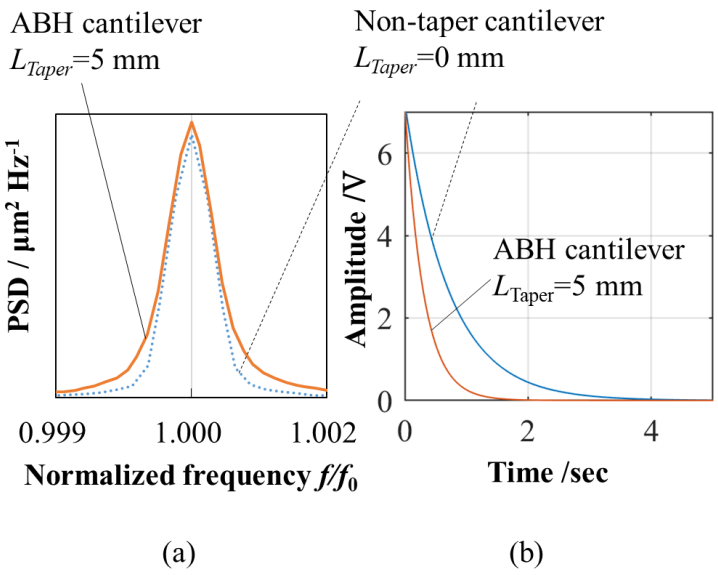

Figure 6.5 (a) Frequency spectra obtained by Fourier-transformation of vibration amplitude wave form in Sweep test. (b) Decay curves of vibration amplitude after resonant vibration in Ring down measurement.

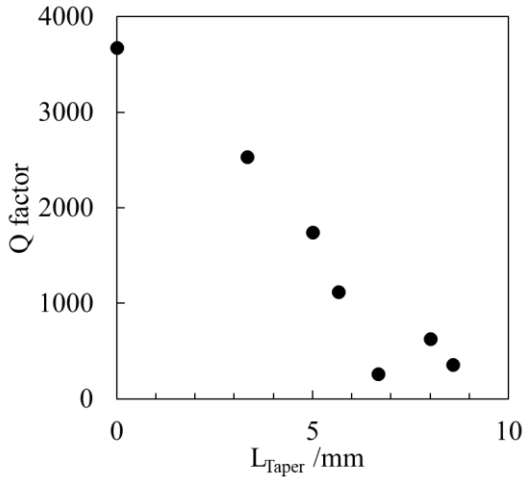

Figure 6.6 Experimental *Q* factor obtained by fitting decay curve from Ring down measurement into the function A · $e^{-\pi\frac{f_1}{Q}t}$.

6.3.3 Chemical properties of the surface after processing

The FTIR reflectance spectrum of the one cantilever surface out of three different samples is shown in **Figure 6.7.** The spectrums from the three different cantilevers showed the same trends.

The absorption spectra were obtained using the Kramers-Kronig transformation applied to the corresponding reflectance spectra. A significant peak around 1110 cm^{-1} shows the asymmetric stretch band of Si-O-Si bonding [2]. The average position of peak around 1100 cm^{-1} showed distinctive dependence on surface condition. Original silica substrate before etching had the peak at 1109.5±0.3 cm^{-1}. After etching, 1108.9 ±0.5 cm^{-1} for non-exposed and 1111.4±0.7 for exposed surface. Although average peak position were almost constant for non-exposed surface before and after etching, peak position of exposed surface shifted to higher wavenumber side.

The peak around 3600 cm^{-1} is related to the presence of OH groups. This peak gets emphasized on the exposed surface. Peak around area I (2000 cm^{-1}) and area II (2233 cm^{-1}) was also detected only on exposed surface, which is assigned to Si-H bond [167][168].

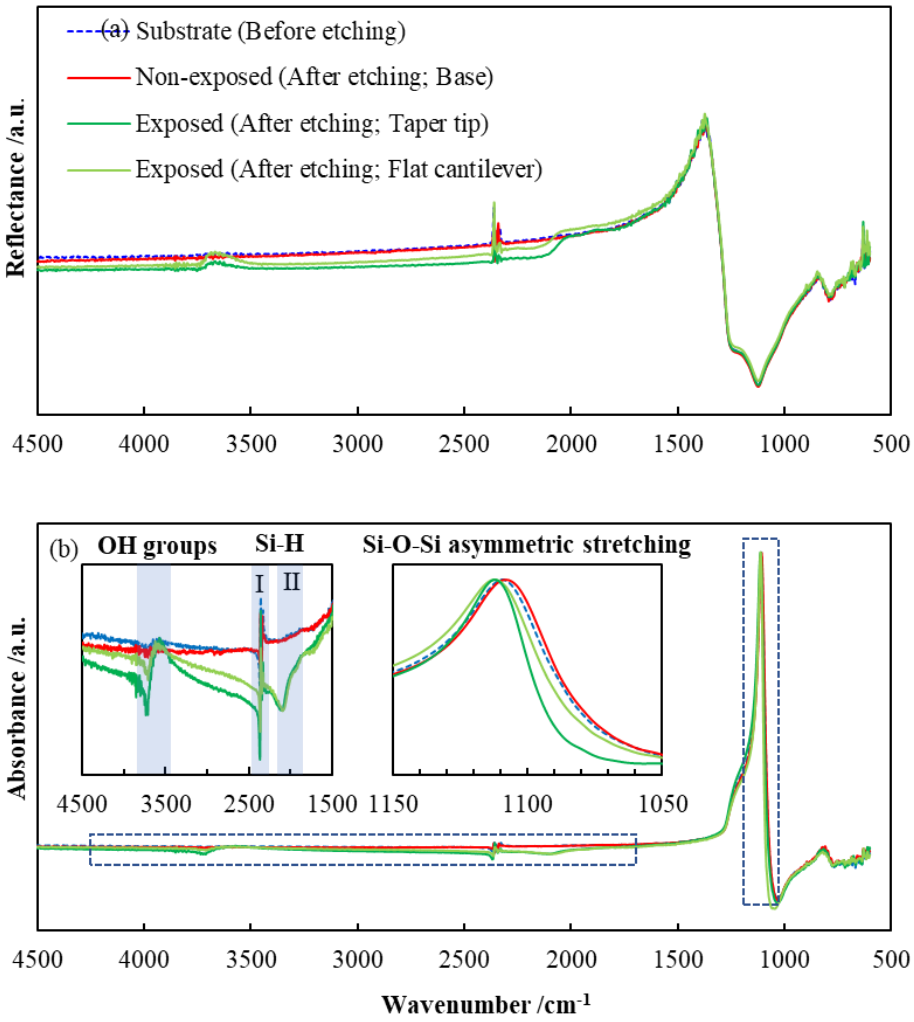

Figure 6.7 Micro IR spectra before and after etching. (a)Specular reflection spectra, (b)Absorption spectra obtained by Kramers-Kronig transformation. Green and red solid lines are the laser-exposed and non-exposed surface after etching, respectively. Blue broken line indicates the initial sample before treatment. Insets represent the expanded spectra of the respective vibration regions.

6.4 Discussion

6.4.1 Structural modification distribution in glass after fs laser exposure

Silica glass cantilever with various taper length showed vibrational attenuations in the frequency range around 2.5~3.5 kHz. The ABH design was successfully implemented by taking advantage of the precise control of the thickness profile at the microscale using femtosecond laser and wet etching micro-processing. To date, the experimental investigations of ABH had been limited for meter-scale structure in metal or in composite materials. The result shown in this report broadens the capability of the ABH effect.

To handle the vibrational behavior of microstructures, it is necessary to control both the preciseness of the structural profile and the materials properties. Therefore, a particular attention was paid on the effects of the fabrication process on fused silica for further understanding possible factors affecting vibrational behaviors. Here we analyze the vibration characteristics, such as resonant frequency and energy dissipation factors by comparing experimental and calculated results.

The actual surface of cantilever after etching was always below the programmed design, though the reduction rate was nearly constant among all samples. Typical dimension values, such as tip thickness h_{Tip} were 53.9 ~ 58.8 μm, cantilever thickness at flat part h_c was 249 ~ 252 μm, as shown in **Table 6.1**. There were always about 40 ~ 50 μm in total thickness reduction compared to the original design. The function of thickness profile was kept as a quadratic function within 93~100 % accuracy based on m value obtained from surface profile scanning. Vibrational behavior supports the accuracy of the 3D cantilever outline. The ABH effect was observed for the cantilever with the tapered thickness profile since this effect is only attainable with a smooth and accurate profile, as shown in Eq. (6).

Even though with an accurate outline profile of the fabricated cantilever, the measured resonant frequency could not be obtained from simulation. As shown in Fig. 4 with several models, a frequency difference degree of 100 Hz that cannot be related to the deviations from the designed profile was observed. Therefore, material properties used in the simulation, such as Young's modulus, Poisson's ratio, and density, can be the reasonable factor that may cause such difference.

6.4.2 Modification effect on dynamic behavior of glass cantilever

As shown in **Figure 6.4**, the experimental values for the resonant frequency were always lower compared to the simulated ones. As shown in the result comparing both,

the gap between design and actual profile would not make such a significant difference. Here we consider the origin of this disagreement as a residual material property change due to laser exposure, as the change was observed only at the exposed surface after processing.

First of all, the femtosecond laser irradiation condition in the fabrication process leads to the formation of nanograting that consists of self-organized texture parallel to one another as can be observed in SEM images [89] [166]. A significant change of refractive index (consisting on a periodic modulation of its value in the laser-affected zone) is generated in highly localized ellipsoidal volume, that are 10-μm high along the laser-induced direction, and about 2-μm wide along the waist [62]. The critical mechanism of high aspect ratio-etching of fused silica is not fully understood [91][164][82]. Intense irradiation of femtosecond laser induces defects in silica such as NBOHC and ODC (II) [169] that show broad fluorescence in the visible wavelength region. However, no fluorescence was found after the etching process by Raman spectrum measurement using an excitation laser with a wavelength of 532 nm. This observation suggests that the exposed volume containing these defects have been dissolved or chemically changed. The material property profile in higher resolution compared to laser focal point is not yet measured. Residual effect after etching is not yet figured out in detail.

In the case of the same micro-fabrication process reported in a previous study [162], the laser drawing spacing in z-axis direction is less than 18 μm results in a higher etching rate of over 90 μm/hour. The etching rate decreases by 99 % when the spacing is more than 21 μm. Similarly, in this report, etching always stopped at 20~25 μm below the laser irradiation line (About 50 μm reduction in thickness, 20~25 μm respectively for top and bottom side), and this reduction was independent of etching time. These results indicate that laser affected modification around 20 μm away from the focal point has essential effect on etching mechanism.

We now turn our attention to the results obtained in this study. The surface condition was different among laser exposed and non-exposed surface after processing. From the FTIR measurement shown in Fig. 7, spectrum differences between exposed and non-exposed surface after etching can be clearly observed. Reflectance spectra of exposed surface showed noticeable shoulder at 2000 cm-1 as shown in Fig. 7 (a). The same trend was found on both taper and flat part of 3 different cantilevers' surface, but never found on non-exposed surface.

As shown in absorbance spectrum from **Figure 6.7 (b)**, OH group and Si-H bond were detected only on the cantilever surface after laser exposure and etching. Si-H

bonding are reported to show different peak position depends on the connectivity of Si atom; the peak at area I shows Si-H with Si atom connected to 3 oxygen (O3SiH), and another slight peak around area II shows Si3SiH [170]. On the other hands, the defects such as NBOHC ($\equiv Si - O \cdot$), ODC (II) ($\equiv Si \cdot$) and ODC (I)($\equiv Si - Si \equiv$) structure were found at femtosecond laser irradiated spot [169]. Furthermore, silicon nano cluster could be generated with relatively low pulse energy with kilohertz repetition [171]. Considering these facts, these defects might be the precursor and combined with H+ during etching to generate OH groups and Si-H bonding. As a result, residual effect of laser exposure might remain after etching and formed distinctive surface compared to non-exposed. Higher roughness on exposed surface may also bring increment of OH groups, though extra modification was suggested by significant effect on reflection around 2000 cm^{-1}.

In addition to generation of functional groups, absorption peak around 1110 cm-1 shifted to higher wavenumber side at the cantilever surface. This peak can be correlated to the fused silica density. Generally, the upshift of this peak is due to an increase in the Si-O-Si bond angle. Moreover, this increment indicates a density decrease of silica glass [172]. The shift was 2.5 cm^{-1}, and this is enough to induce 500 ppm reduction of silica density [173], ending up in a decrease from 2201 to 2200 kg/m3. In the case of fused silica, a lower density has a correlation with lower etching rate [44].

In this experiment, FTIR measurements were observing the chemical bonding state down to 10 μm under the surface of the cantilever. These chemical properties change at the exposed surface indicates the generation of a silica layer with different material constants such as density and Young's modulus, consecutive to the micromachining process. As increment of OH contents in fused silica lowers the Young's modulus [174], we considered the same effect is occurring on the cantilever surface containing terminal bondings like Si-OH and Si-H.

These material properties change affect the vibration characteristics, as shown in Eq. (2~8). Experimental results for all cantilever showed a lower resonant frequency compared to the simulation, as shown in Figure 6.4. This difference can be explained by having a lower Young's modulus layer at the surface, as if an absorbing layer covers the cantilever. Model C in **Figure 6.4** was plotted with empty diamonds has lower material constants (Esurface= 60 GPa) in a region of 10 μm below the exposed surface, supposing a residual effect of laser exposure and etching. Partial decrease of material constants lowered the resonant frequency more than the dimensional error.

The surface of silica glass after femtosecond laser micro-machining was modified, and this effect was analyzed qualitatively. At this point, the measurement of density and

Young's modulus profile inside the glass sample was difficult. With further understanding of surface properties, quantitative analysis of damping effect based on ABH theory given in Krylov's report[158] will be possible.

However, it seems clear that a key factor for ABH damping of micro-scale structure is not only the design of the shape, but also the material properties change during the fabrication process. Lower Young's modulus provides a damping effect by lowering the reflection coefficient R as given in Eq. (5) and (7). In the case of ABH effect implementation, this femtosecond laser-induced modification effectively enhanced the damping effect.

6.4.3 Possibility of femtosecond laser processing on glass

An Acoustic Black Hole effect was observed in a fused silica micro-scale cantilever. It successfully showed the ABH effect with double-sided tapering taking advantage of micro-scale accurate machining using a femtosecond laser. In addition, the effect was realized in the lower frequency range compared to previous reports. It is now possible to attenuate desirable frequency depends on structural design with a wide variety of materials. Furthermore, additional damping layer of different material is unnecessary to enhance the ABH effect and to keep the optical transparency of the cantilever. In this way, the ABH effect can be applied in the field of micro-optical devices by combining factors such as micro-dimension and transparent material. This study is the first approach of ABH (vibration dynamics) toward micromechanical and optical systems.

It seemed all laser affected area was washed away after etching, though residual exposure effects were observed through vibration test with various tapered length cantilevers. This modified layer affects the dynamic behavior of the microfabricated structural object and gives an additional damping effect on micro 3D structural objects.

This highly accurate 3D micro processing by femtosecond laser irradiation is only applicable for fused silica. The cause is clear by considering the absorption band of respective glass and photon energy given by single and multi-photon absorption, as illustrated in **Figure 6.8** Femtosecond pulse laser often Ti: Sapphire laser with photon energy of 1.55 eV (λ=800 nm) in continuous emission. In multi photon absorption, about 7.5~9 eV (137~165 nm) photon energy is given at focal point[169]. Contrary to fused silica, most of the commercial glass including silicate (containing alkali content), borosilicate [175], and aluminosilicate [176] glasses have smaller optical window, which indicates absorption of photon energy at outside of focal point with lower deposited energy. Often femtosecond laser exposure on the glass except fused silica results in surface ablation. From this study, possibility of partial material properties

control on the glass surface. Irradiation of femtosecond laser on multicomponent glass can introduce various changes on the surface morphology by introducing ablation , nanograting, phase separation, and so on. By further investigation on material properties distribution of the surroundings of laser focal point, function implementation on glass substrate can be expected.

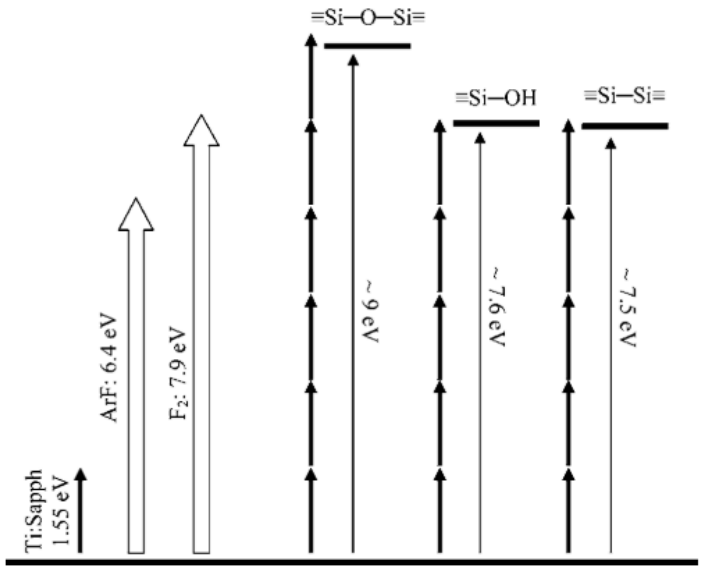

Figure 6.8 Schematic representation of the computed electronic transitions of defect precursors, from reference [169]

6.5 Summary

3D micro processing on fused silica glass by combination of Femtosecond laser enabled micro-scale thickness profile control of silica glass cantilever. By tapering the cantilever tip following quadratic function, damping effect was observed in resonant vibration frequency, which is so called Acoustic Blackhole effect.

The residual effects of the laser exposure were observed at the surface of the specimen that have noticeable influence on the dynamic behavior of the device. Besides fused silica mostly consisting of Si-O bonding, there were higher Si-OH and Si-H observed at laser exposed surface after leaching. In addition, the difference in experimental and calculated dynamic behavior indicated the change in Young's modulus inside the silica glass cantilever. Such material properties change at surrounding of the laser focal point would give possibility of giving additional function in fabricated glass sample.

7 Nano-micrometer size structural control by laser irradiation on glass

7.1 Possibility of functional designing in monolithic glass substrate

By designing material properties contrast deliberately by laser irradiation, various functionalities can be implemented on glass substrate. The monolithic combination of different nanostructure was easily realized by single CW-laser scanning, without complicated process. The porous/ non-porous glass substrate would have function as 2D-designed filter, space-selective wettability control, and so on. With further precise thermal history control by local laser heating, the phase size and morphology would be possible including consideration of the glass composition. Femtosecond laser irradiation enabled highly accurate thickness control in microscale. The acid leaching washes away most of the laser exposed area, though some residual chemical and physical changes were observed in the silica glass sample after fabrication process. This residual change had not been focused, though it had given certain effect on dynamic behavior of the glass substrate, vibration behavior in specific. Including such material property change will give additional dimension in designing and implementing function inside monolithic glass substrate.

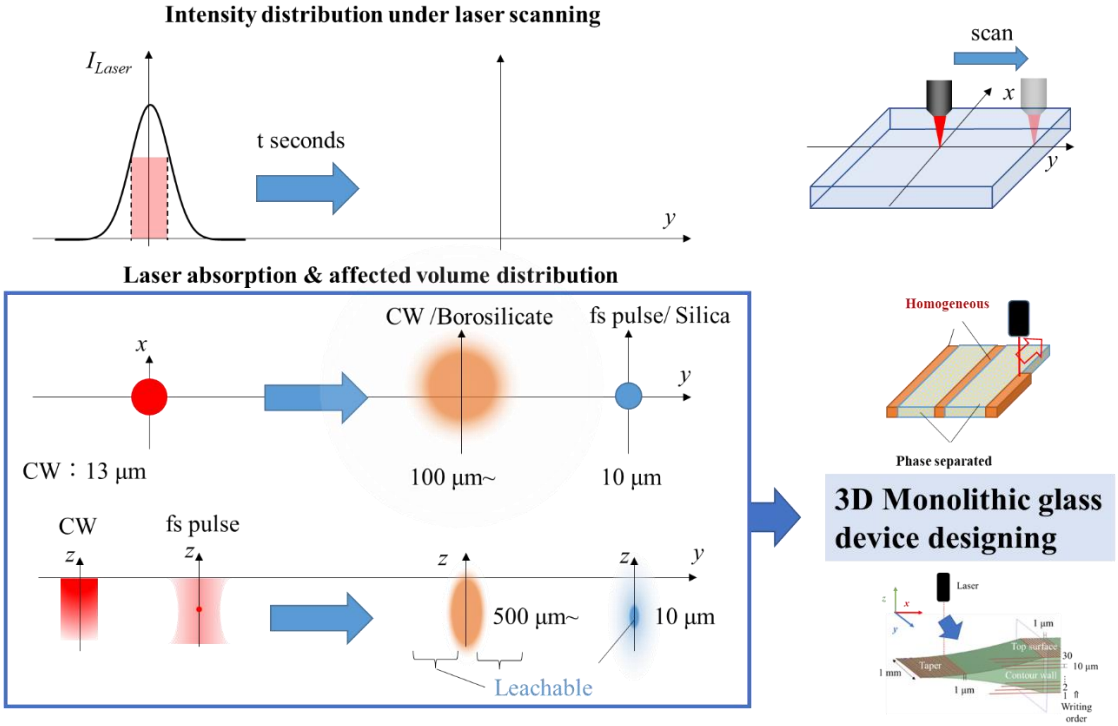

Figure 7.1 Schematic illustration of laser irradiation and its affect in the glass substrate in this study.

Usually, combining two different materials requires bonding process. The bonding process on material surface involves surface treatment (cleaning, surface activation, adhesive coating) and temperature control. The local property change by laser irradiation would yield two different ‘materials’ in continuous volume. For example, optical fiber consists of core fiber surrounded by another material with different refractive index. Similarly, femtosecond laser irradiation can introduce refractive index gap inside the glass substrate, which is so called optical waveguide for light propagation. Material processing by laser irradiation can reproduce and give further development to the function designed by bonding of different materials.

High intensity exposure by laser will cause ablation in the material. The cutting or drilling of plate by material ablation is one of the most popular processes using laser. Most of the laser processing to date has been investigated for the cross section of the workpiece. In order to utilize the laser not only as a material cutter, but also as a painter that can freely create structures, it is necessary to understand the physical properties and reactions at the irradiated area. In recent year, adaptive optics have been developed to modify the beam profile in higher variation, including shape and focal depth. This has begun to progress contribute to improve the processing accuracy of pulsed lasers.[177]

There are numerous combinations of materials, laser oscillation method, and irradiation conditions. In order to realize desirable processing, it is essential to understand the phenomena and to predict the response of the material to the laser exposure. The simulation model developed in this study will enable prediction of the homogenized volume by giving material properties, laser wavelength, power, scanning speed, and specimen dimensions. The thermal history is spatially distributed by heat transfer due to laser absorption. In case the laser absorber is the material with phase immiscibility, the development and homogenization of phase separation can be predicted based on the results of time-resolved high temperature in-situ measurement. The accuracy of calculation model would be achieved by considering the temperature dependence of the material properties with a heat conduction model that includes glass-specific transmission and radiative heat transfer.

The absorption behavior of lasers varies greatly depending on the combination of reflectivity + absorptivity + transmittance = 1, which varies with the material, light wavelength, and incident direction. For example, metals, which have been the subject of much research on laser local melting, have high reflection and most of the absorption takes place at the surface, with little transmission. Glass materials often show little reflection on its surface and allows a wide range of light to pass through. In this study, we took advantage of this property and succeeded in heating the glass by weak

absorption of transition metal ion doped in the glass. By this heating, the two separated phases were miscible at high temperatures and remained at room temperature by rapid cooling. The precise temperature control by laser, combined with the understanding of material properties at high temperatures, enables the material processing would introduce phase transformation which may involves more variation in properties and nano-microstructures.

7.2 Spatial distribution of laser effect in surroundings of focal spot

The analysis on laser affected material is mainly focused on focal point. It is difficult to evaluate the slight contrast in limited volume of the surroundings of focal point. It requires local material properties evaluation in high resolution, although not every material property is yet adopted to be measured locally. For example, the measurement of Young's modulus requires specimen size larger than 40 mm 5 mm with thickness of 1.0 mm at least defined for metallic materials in JIS Z 2280-1993. The measurement gives average value of whole specimen, usually considered to be homogeneous. In order to evaluate local Young's modulus change introduced by laser irradiation, it is necessary to interpret the measurement results from a mechanical model approximated as a composite material with regions of different physical properties[86]. Although, the accurate spatial distribution of the physical properties are difficult to evaluate from such approximation. It is essential to establish a high-resolution local property evaluation method in order to understand the effect of laser exposure in the material. In this study, temperature change in the material by laser irradiation could be visualized through calculation by FE method. Consideration of the temperature dependence of the physical properties enabled the prediction of the distribution of properties after laser irradiation.

In this study, fluidity due to viscosity decrease above the melting point, heat of vaporization was not taken account in the simulation. By incorporating these factors, the morphology of the laser irradiation traces will also be more accurately determined [145].

7.3 The effect of thermal history on glass structure

The glass structure is frozen in the atomic configuration apparently same as in high temperature [178]. In this study, sodium borosilicate glass was quenched from melt to room temperature, with remaining stable structure at melt by CW laser scanning. This is the first try in this study to control thermal history after the laser exposure, as illustrated in **Figure 7.2**. The most frequent use of the laser processing is for cutting using ablation. In the ablation process, the glass volume under laser exposure is evaporated and beside temperature distribution, thermal history does not affect the processing quality (pulsed

laser is preferable). Crystallization introduced by laser irradiation on the glass is reported previously with same heating method using additive TM ions as heat source, though crystal phase is stable under room temperature and the obtained structure was not modified during the cooling process[67]. In case of phase separation, homogeneous (miscible) state is unstable at room temperature and difficult to be obtained in the bulk glass. Although, the sufficient heating for homogenization of phase separated glass and quenching for remaining melt structure was compatible by fast scanning of CW-laser. Further development on glass processing would be possible by considering entire thermal history given by laser irradiation, e.g., pore size modification by phase separation control, precipitation of bearing metal ion, and expansion of glass forming region by homogenization on the glass which was insoluble by former melt-quenching method.

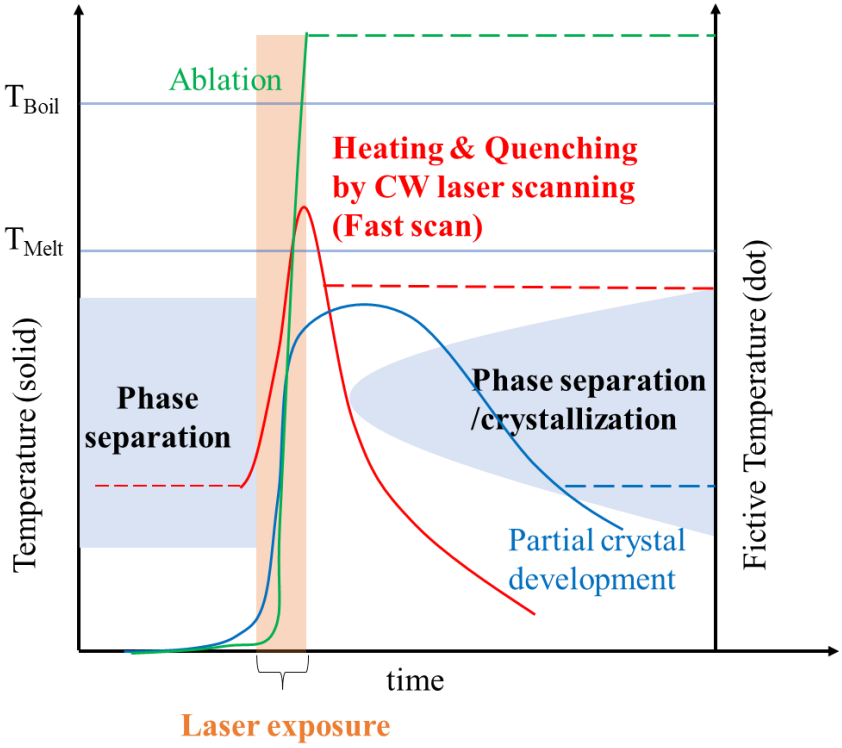

Figure 7.2 Schematic illustration of T-T-T (Time-Temperature-Transformation) diagram with thermal history given by CW laser exposure for respective purpose. The red line indicates heating and quenching effect of laser scanning developed in this study. The other two lines are previously established laser processing for comparison; the green line for ablation for glass cutting and blue line for partial crystallization in glass substrate.

In addition, some of the material properties remain similar as the properties in melt, for example density and heat capacity[179]. The material properties under high temperature are necessary to understand the possible material change during laser exposure. The in-situ measurements of material properties at high temperatures provide very important information for understanding and predicting reactions and structural changes induced by laser irradiation. However, the difficulty with laser irradiation is that the glass structure is non-equilibrium, and the structure may always show non-equilibrium state during the reaction after a short period of irradiation. Therefore, the measurement of time-resolved changes in material properties may give further development in the field of laser light and matter interaction. In particular, it is necessary to clarify the physical properties that have a large influence on the structure (light absorbance, emissivity, and so on) and the regions with a noticeable temperature dependence, such as the glass transition and melting temperature.

8 Conclusion

Laser absorption in the glass locally introduced in nano-microscale structural change. Taking advantage of spatial gap in material property, monolithic glass devices were designed to add further function on glass substrate. The mechanism of Laser introduced structural change could be understood through temperature dependence of the glass and melt structure. This thesis focused on two different combinations of laser and glass.

The first combination was continuous wave (CW) laser and borosilicate glass. In chapter 2, non-porous borosilicate region could be designed on the nano porous silica glass substrate, with clear boundary between two different nanostructures after acid leaching on . By taking advantage of liquid and gas flow capacity inside porous region, fluidics or gas channel with high transparency and durability would be able to be fabricated using such substrates. In the fabrication process, CW-laser with NIR wavelength was successfully absorbed by bearing transition metal ion (Ni^{2+} or Cu^{2+}) in sodium borosilicate glass. Those transition metal ion transferred absorbed energy into heat. The heat enabled phase separated borosilicate glass to turn into homogeneous condition.

After laser irradiation on Ni^{2+} doped glass, the coloration change was observed from green to brown, with higher acid leaching durability selectively at laser irradiated area. In chapter 3, the speciation change of Ni^{2+} ion doped in sodium borosilicate glass was observed during heating up to 1200°C. Ni^{2+} ion was originally doped as laser absorber to generate heat inside the glass. The coordination number of Ni^{2+} ion changed from 6- to 4-coordinated when the glass turned from phase separated to homogeneous at 1000°C. Such transformation of Ni^{2+} ion probed the immiscibility change in laser irradiated glass plate.

The phase separation behavior in the glass kept changing during heating and cooling process. In chapter4, time resolved change of nanoscale immiscibility in sodium borosilicate glass was observed by high temperature in-situ SAXS measurement to clarify the phase separation . Addition of transition metal ion changed the temperature dependence of phase separation development. While heating the phase separated glass, further phase separation development affected the homogenization temperature. The critical temperature where phase separation starts to develop could be observed during cooling process from homogeneous melt.

The homogenization of phase separated borosilicate glass was achieved within short heating time under laser irradiation. In chapter 5, the time-dependent temperature profile during laser irradiation could be calculated by finite element method based on heat transfer and radiation inside the glass plate. The critical cooling rate required to

obtain clear boundary between porous/ nonporous structure observed in chapter 2 was observed, considering the temperature dependence of phase separation obtained in chapter 4.

The effect of femtosecond laser absorption in silica glass was focused in chapter 6. 3D micro processing technique of silica glass by combination of femtosecond laser irradiation and wet etching could realize precise control of silica glass cantilever thickness profile in microscale. By comparing vibration test and calculation, the residual effect of the laser exposure was suggested. Such structural modification might have caused by change of the amount of Si-OH and Si-H.

Prospects on laser absorption in glass material was summarized in chapter 7. From this thesis, the new precise thermal history control could be achieved by CW laser irradiation on borosilicate glass to realize sub-nano to micro scale structural modification. The importance of structural understanding under high temperature exposure and its in-situ observation was confirmed through clarification of laser-induced modification mechanism. Further control and designing ability of glass property will be possible by revealing laser absorption mechanism and clarifying the distribution of structural modification around laser focal point.

9 Reference

[1] P. Richet and B. O. Mysen, *Silicate Glasses and Melts*, 1st ed. Elsevier B.V, 2005.

[2] M. Tomozawa, J. W. Hong, and S. R. Ryu, "Infrared (IR) investigation of the structural changes of silica glasses with fictive temperature," *J. Non. Cryst. Solids*, vol. 351, no. 12–13, pp. 1054–1060, 2005, doi: 10.1016/j.jnoncrysol.2005.01.017.

[3] B. E. Warren, "Summary of Work on Atomic Arrangement in Glass," *J. Am. Ceram. Soc.*, vol. 24, no. 8, pp. 256–261, 1941, doi: 10.1111/j.1151-2916.1941.tb14858.x.

[4] A. A. Ahmed, A. F. Abbas, and S. M. Salman, "Thermal Expansion of Mixed Alkali Borate Glasses.," *Phys. Chem. Glas.*, vol. 26, no. 1, pp. 17–23, 1985.

[5] Y. Hiroshima, Y. Hamamoto, S. Yoshida, and J. Matsuoka, "Thermal conductivity of mixed alkali silicate glasses at low temperature," *J. Non. Cryst. Solids*, vol. 354, no. 2–9, pp. 341–344, 2008, doi: 10.1016/j.jnoncrysol.2007.08.082.

[6] M. Neyret, M. Lenoir, A. Grandjean, N. Massoni, B. Penelon, and M. Malki, "Ionic transport of alkali in borosilicate glass. Role of alkali nature on glass structure and on ionic conductivity at the glassy state," *J. Non. Cryst. Solids*, vol. 410, pp. 74–81, 2015, doi: 10.1016/j.jnoncrysol.2014.12.002.

[7] K. Yamahara, K. Okazaki, and K. Kawamura, "Molecular dynamics study of the thermal behaviour of silica glass/melt and cristobalite," *J. Non. Cryst. Solids*, vol. 291, no. 1–2, pp. 32–42, 2001, doi: 10.1016/S0022-3093(01)00795-5.

[8] J. F. Stebbins, "Effects of temperature and composition on silicate glass structure and dynamics: SI-29 NMR results," *J. Non. Cryst. Solids*, vol. 106, no. 1–3, pp. 359–369, 1988, doi: 10.1016/0022-3093(88)90289-X.

[9] T. Maehara, T. Yano, S. Shibata, and M. Yamane, "Structure and phase transformation of alkali silicate melts analysed by Raman spectroscopy," *Philos. Mag.*, vol. 84, no. 29, pp. 3085–3099, 2004, doi: 10.1080/14786430410001725890.

[10] B. O. Mysen and J. D. Frantz, "Silicate melts at magmatic temperatures: in-situ structure determination to 1651°C and effect of temperature and bulk composition on the mixing behavior of structural units," *Contrib. to Mineral. Petrol.*, vol. 117, no. 1, pp. 1–14, 1994, doi: 10.1007/BF00307725.

[11] D. Möncke *et al.*, "Transition and post-transition metal ions in borate glasses: Borate ligand speciation, cluster formation, and their effect on glass transition and mechanical properties," *J. Chem. Phys.*, vol. 145, no. 12, pp. 1–16, 2016, doi:

10.1063/1.4962323.

[12] J. Wu, J. F. Stebbins, and T. Rouxel, “Cation Field Strength Effects on Boron Coordination in Binary Borate Glasses,” *J. Am. Ceram. Soc.*, vol. 97, no. 9, pp. 2794–2801, 2014, doi: 10.1111/jace.13100.

[13] J. Luo, Y. Zhou, C. G. Pantano, and S. H. Kim, “Correlation between IR peak position and bond parameter of silica glass: Molecular dynamics study on fictive temperature (cooling rate) effect,” *J. Am. Ceram. Soc.*, vol. 101, no. 12, pp. 5419–5427, 2018, doi: 10.1111/jace.15858.

[14] T. V. Antropova, I. N. Anfimova, and G. F. Golovina, “Influence of the composition and temperature of heat treatment of porous glasses on their structure and light transmission in the visible spectral range,” *Glas. Phys. Chem.*, vol. 35, no. 6, pp. 572–579, 2009, doi: 10.1134/S1087659609060042.

[15] J. H. SIMMONS, S. A. MILLS, and A. NAPOLITANO, “Viscous Flow in Glass During Phase Separation,” *J. Am. Ceram. Soc.*, vol. 57, no. 3, pp. 109–117, 1974, doi: 10.1111/j.1151-2916.1974.tb10830.x.

[16] J. H. Simmons, “Refractive index and density changes in a phase-separated borosilicate glass,” *J. Non. Cryst. Solids*, vol. 24, no. 1, pp. 77–88, 1977, doi: 10.1016/0022-3093(77)90063-1.

[17] A. Yasumori, “Phase Separation and High Performance realization of Sodium Borosilicate Glasses,” *New Glas.*, vol. 28, pp. 5–12, 2013.

[18] O. V. Mazurin and E. A. Porai-Koshits, *Phase Separation in Glass*. North-Holland Physics Publishing, 1984.

[19] T. H. Elmer, M. E. Nordberg, G. B. Carrier, and E. J. Korda, “Phase Separation in Borosilicate Glasses as Seen by Electron Microscopy and Scanning Electron Microscopy,” *J. Am. Ceram. Soc.*, vol. 53, no. 4, pp. 171–175, Apr. 1970, doi: 10.1111/j.1151-2916.1970.tb12064.x.

[20] H. Tanaka, T. Yazawa, K. Eguchi, H. Nagasawa, N. Matsuda, and T. Einishi, “Precipitation of colloidal silica and pore size distribution in high silica porous glass,” *J. Non. Cryst. Solids*, vol. 65, no. 2–3, pp. 301–309, 1984, doi: 10.1016/0022-3093(84)90054-1.

[21] E. P. Favvas and A. C. Mitropoulos, “What is spinodal decomposition?,” *J. Eng. Sci. Technol. Rev.*, vol. 1, no. 1, pp. 25–27, 2008, doi: 10.25103/jestr.011.05.

[22] G. R. Srinivasan, I. Tweer, P. B. Macedo, A. Sarkar, and W. Haller, “Phase separation in SiO2B2O3Na2O system,” *J. Non. Cryst. Solids*, vol. 6, no. 3, pp. 221–239, 1971, doi: 10.1016/0022-3093(71)90005-6.

[23] J. W. Cahn, “Phase separation by spinodal decomposition in isotropic systems,” *J.*

Chem. Phys., vol. 42, no. 1, pp. 93–99, 1965, doi: 10.1063/1.1695731.

[24] T. Yazawa, K. Kuraoka, T. Akai, N. Umesaki, and W. F. Du, "Clarification of Phase Separation Mechanism of Sodium Borosilicate Glasses in Early Stage by Nuclear Magnetic Resonance," *J. Phys. Chem. B*, vol. 104, no. 9, pp. 2109–2116, 2000, doi: 10.1021/jp993416b.

[25] B. R. Wheaton and A. G. Clare, "Evaluation of phase separation in glasses with the use of atomic force microscopy," *J. Non. Cryst. Solids*, vol. 353, no. 52–54, pp. 4767–4778, 2007, doi: 10.1016/j.jnoncrysol.2007.06.073.

[26] S. S. Kim and T. H. Sanders, "Phase-field simulation of spinodal phase separation in the Na2O-SiO2 glasses," *J. Non. Cryst. Solids*, vol. 528, no. September 2019, 2020, doi: 10.1016/j.jnoncrysol.2019.119591.

[27] W. Haller, "Rearrangement kinetics of the liquid-liquid immiscible microphases in alkali borosilicate melts," *J. Chem. Phys.*, vol. 42, no. 2, pp. 686–693, 1965, doi: 10.1063/1.1695991.

[28] T. N. Vasilevskaya and N. S. Andreev, "Experimental small-angle X-ray scattering investigation of initial stages of the spinodal decomposition in model sodium silicate glasses," *Phys. Solid State*, vol. 53, no. 11, pp. 2250–2262, 2011, doi: 10.1134/S106378341111031X.

[29] T. TAKAMORI and M. TOMOZAWA, "Viscosity and Microstructure of Phase-Separated Borosilicate Glasses," *J. Am. Ceram. Soc.*, vol. 62, no. 7–8, pp. 373–377, 1979, doi: 10.1111/j.1151-2916.1979.tb19082.x.

[30] M. Tomozawa, S. Sridharan, and T. Takamori, "Origin of Viscosity Increase of Phase-Separated Borosilicate Glasses," *J. Am. Ceram. Soc.*, vol. 75, no. 11, pp. 3103–3110, 1992, doi: 10.1111/j.1151-2916.1992.tb04394.x.

[31] T. P. S. III, D. R. UHLMANN, and D. TURNBULL, "Development of Two-Phase Structure in Glasses, with Special Reference to the System BaO-SiO2," *J. Am. Ceram. Soc.*, vol. 51, no. 11, pp. 634–642, 1968, doi: 10.1111/j.1151-2916.1968.tb12635.x.

[32] H. Takeno, M. Iwata, M. Takenaka, and T. Hashimoto, "Combined light scattering and laser scanning confocal microscopy studies of a polymer mixture involving a percolation-to-cluster transition," *Macromolecules*, vol. 33, no. 26, pp. 9657–9665, 2000, doi: 10.1021/ma001316u.

[33] S. Schuller, "Phase separation in glass," 2019.

[34] C. Y. Yap *et al.*, "Review of selective laser melting : Materials and applications Review of selective laser melting : Materials and applications," vol. 041101, no. December 2015, 2018, doi: 10.1063/1.4935926.

[35] M. Chini, K. Zhao, and Z. Chang, “The generation, characterization and applications of broadband isolated attosecond pulses,” *Nat. Photonics*, vol. 8, no. 3, pp. 178–186, 2014, doi: 10.1038/nphoton.2013.362.

[36] N. J. Tostanoski, “Glasses in a Fraction of a Second,” *Opt. Photonics News*, 2022.

[37] A. Schiffrin *et al.*, “Optical-field-induced current in dielectrics,” *Nature*, vol. 493, no. 7430, pp. 70–74, Jan. 2013, doi: 10.1038/nature11567.

[38] レーザー学会, “レーザープロセシング（レーザー加工）応用便覧,” 2006. https://optipedia.info/laser/process_handbook/pro_handbook_1st_section/1st_1_1/.

[39] H. B. Sun, S. Juodkazis, M. Watanabe, S. Matsuo, H. Misawa, and J. Nishii, “Generation and recombination of defects in vitreous silica induced by irradiation with a near-infrared femtosecond laser,” *J. Phys. Chem. B*, vol. 104, no. 15, pp. 3450–3455, 2000, doi: 10.1021/jp992828h.

[40] D. L. Griscom, “Optical properties and structure of defects in silica glass,” *Nippon Seramikkusu Kyokai Gakujutsu Ronbunshi/Journal Ceram. Soc. Japan*, vol. 99, no. 1154, pp. 923–942, 1991, doi: 10.2109/jcersj.99.923.

[41] L. Skuja, H. Hosono, and M. Hirano, “Laser-induced color centers in silica,” *Laser-Induced Damage Opt. Mater. 2000*, vol. 4347, no. April 2001, p. 155, 2001, doi: 10.1117/12.425020.

[42] R. Boffy, S. Peuget, R. Schweins, J. Beaucour, and F. J. Bermejo, “High thermal neutron flux effects on structural and macroscopic properties of alkali-borosilicate glasses used as neutron guide substrate,” *Nucl. Instruments Methods Phys. Res. Sect. B Beam Interact. with Mater. Atoms*, vol. 374, pp. 14–19, 2016, doi: 10.1016/j.nimb.2015.10.011.

[43] M. Shimbo and K. Sato, “Change in uv transmittance in silica photomask glass under krf excimer laser irradiation,” *Jpn. J. Appl. Phys.*, vol. 34, no. 10, pp. 5640–5643, 1995, doi: 10.1143/JJAP.34.5640.

[44] A. Agarwal and M. Tomozawa, “Correlation of silica glass properties with the infrared spectra,” *J. Non. Cryst. Solids*, vol. 209, no. 1–2, pp. 166–174, 1997, doi: 10.1016/S0022-3093(96)00542-X.

[45] M. Guerette *et al.*, “Structure and Properties of Silica Glass Densified in Cold Compression and Hot Compression,” *Sci. Rep.*, vol. 5, pp. 1–10, Oct. 2015, doi: 10.1038/srep15343.

[46] A. M. Efimov and V. G. Pogareva, “IR absorption spectra of vitreous silica and silicate glasses: The nature of bands in the 1300 to 5000 cm−1 region,” *Chem. Geol.*, vol. 229, no. 1–3, pp. 198–217, May 2006, doi:

10.1016/j.chemgeo.2006.01.022.

[47] E. Stolper, “Water in silicate glasses: An infrared spectroscopic study,” *Contrib. to Mineral. Petrol.*, vol. 81, no. 1, pp. 1–17, 1982, doi: 10.1007/BF00371154.

[48] R. Kitamura, L. Pilon, and M. Jonasz, “Optical constants of silica glass from extreme ultraviolet to far infrared at near room temperature,” *Appl. Opt.*, vol. 46, no. 33, pp. 8118–8133, 2007, doi: 10.1364/AO.46.008118.

[49] A. D. McLachlan and F. P. Meyer, “Temperature dependence of the extinction coefficient of fused silica for CO_2 laser wavelengths,” *Appl. Opt.*, vol. 26, no. 9, p. 1728, 1987, doi: 10.1364/ao.26.001728.

[50] M. Serhatlioglu, B. Ortaç, C. Elbuken, N. Biyikli, and M. E. Solmaz, “CO2 laser polishing of microfluidic channels fabricated by femtosecond laser assisted carving,” *J. Micromechanics Microengineering*, vol. 26, no. 115011, Oct. 2016, doi: 10.1088/0960-1317/26/11/115011.

[51] C. Buerhop, B. Blumenthal, R. Weissmann, N. Lutz, and S. Biermann, “Glass surface treatment with excimer and CO2 lasers,” *Appl. Surf. Sci.*, vol. 46, no. 1–4, pp. 430–434, Dec. 1990, doi: 10.1016/0169-4332(90)90184-2.

[52] C. Lin, L. G. Cohen, R. H. Stolen, G. W. Tasker, and W. G. French, “Near-infrared sources in the 1-1.3 μm region by efficient stimulated Raman emission in glass fibers,” *Opt. Commun.*, vol. 20, no. 3, pp. 426–428, 1977, doi: 10.1016/0030-4018(77)90221-8.

[53] R. Juza, H. Seidel, and J. Tiedemann, “Color Centers in Alkali Borate Glasses Containing Cobalt, Nickel, or Copper,” *Angew. Chemie Int. Ed. English*, vol. 5, no. 1, pp. 85–94, 1966, doi: 10.1002/anie.196600851.

[54] T. Honma, Y. Benino, T. Fujiwara, and T. Komatsu, “Transition metal atom heat processing for writing of crystal lines in glass,” *Appl. Phys. Lett.*, vol. 88, no. 23, pp. 3–6, 2006, doi: 10.1063/1.2212272.

[55] T. Honma, † Phan, T. Nguyen, and T. Komatsu, “Crystal growth behavior in CuO-doped lithium disilicate glasses by continuous-wave fiber laser irradiation,” 2008.

[56] R. Menzel, *Photonics: Linear and Nonlinear Interactions of Laser Lights and Matter*. Springer, 2001.

[57] K. M. Davis, K. Miura, N. Sugimoto, and K. Hirao, “Writing waveguides in glass with a femtosecond laser,” *Opt. Lett.*, vol. 21, no. 21, p. 1729, 1996, doi: 10.1364/ol.21.001729.

[58] E. N. Glezer *et al.*, “Three-dimensional optical storage inside transparent materials: errata,” *Opt. Lett.*, vol. 22, no. 6, p. 422, Mar. 1997, doi:

10.1364/OL.22.000422.

[59] C. Hnatovsky *et al.*, “Pulse duration dependence of femtosecond-laser-fabricated nanogratings in fused silica,” *Appl. Phys. Lett.*, vol. 87, no. 1, Jul. 2005, doi: 10.1063/1.1991991.

[60] R. Taylor, C. Hnatovsky, and E. Simova, “Applications of femtosecond laser induced self-organized planar nanocracks inside fused silica glass,” *Laser Photonics Rev.*, vol. 2, no. 1–2, pp. 26–46, 2008, doi: 10.1002/lpor.200710031.

[61] K. Sugioka, Y. Hanada, and K. Midorikawa, “Three-dimensional femtosecond laser micromachining of photosensitive glass for biomicrochips,” *Laser Photonics Rev.*, vol. 4, no. 3, pp. 386–400, 2010, doi: 10.1002/lpor.200810074.

[62] Y. Bellouard, A. Said, M. Dugan, and P. Bado, “Fabrication of high-aspect ratio, micro-fluidic channels and tunnels using femtosecond laser pulses and chemical etching,” *Opt. Express*, vol. 12, no. 10, pp. 2120–2129, May 2004, doi: 10.1364/opex.12.002120.

[63] P. Wang *et al.*, “Three-dimensional laser printing of macro-scale glass objects at a micro-scale resolution,” *Micromachines*, vol. 10, no. 9, Sep. 2019, doi: 10.3390/mi10090565.

[64] K. Tomita, T. Kishi, T. Yano, P. Vlugter, and Y. Bellouard, “ABH damping of monolithic silica glass cantilever by structural and material modification using fs laser micromachining,” *Int. J. Appl. Glas. Sci.*, vol. 12, no. 1, pp. 36–45, 2021, doi: 10.1111/ijag.15857.

[65] J. Drs, T. Kishi, and Y. Bellouard, “Laser-assisted morphing of complex three dimensional objects,” *Opt. Express*, vol. 23, no. 13, p. 17355, 2015, doi: 10.1364/oe.23.017355.

[66] F. Laguarta, N. Lupon, and J. Armengol, “Optical glass polishing by controlled laser surface-heat treatment,” *Appl. Opt.*, vol. 33, no. 27, p. 6508, 1994, doi: 10.1364/ao.33.006508.

[67] M. Shimada, T. Honma, and T. Komatsu, “Laser patterning of oriented LiNbO3 crystal particle arrays in NiO-doped lithium niobium silicate glasses,” *Int. J. Appl. Glas. Sci.*, vol. 9, no. 4, pp. 518–529, 2018, doi: 10.1111/ijag.12390.

[68] H. Sugita, T. Honma, Y. Benino, and T. Komatsu, “Formation of LiNbO3 crystals at the surface of TeO2 -based glass by YAG laser-induced crystallization,” *Solid State Commun.*, vol. 143, no. 6–7, pp. 280–284, 2007, doi: 10.1016/j.ssc.2007.06.002.

[69] G. M. Whitesides, “The origins and the future of microfluidics,” *Nature*, vol. 442, no. 7101, pp. 368–373, 2006, doi: 10.1038/nature05058.

[70] L. Jiang, A. D. Wang, B. Li, T. H. Cui, and Y. F. Lu, “Electrons dynamics control by shaping femtosecond laser pulses in micro/nanofabrication: Modeling, method, measurement and application,” *Light Sci. Appl.*, vol. 7, no. 2, pp. 1–27, 2018, doi: 10.1038/lsa.2017.134.

[71] G. Steinmeyer, D. H. Sutter, L. Gallmann, N. Matuschek, and U. Keller, “Frontiers in ultrashort pulse generation: Pushing the limits in linear and nonlinear optics,” *Science (80-.).*, vol. 286, no. 5444, pp. 1507–1512, 1999, doi: 10.1126/science.286.5444.1507.

[72] S. S. Mao *et al.*, “Dynamics of femtosecond laser interactions with dielectrics,” *Appl. Phys. A Mater. Sci. Process.*, vol. 79, no. 7, pp. 1695–1709, 2004, doi: 10.1007/s00339-004-2684-0.

[73] T. Brabec and F. Krausz, “Intense few-cycle laser fields: Frontiers of nonlinear optics,” *Rev. Mod. Phys.*, vol. 72, no. 2, pp. 545–591, 2000, doi: 10.1103/RevModPhys.72.545.

[74] R. R. Gattass and E. Mazur, “Femtosecond laser micromachining in transparent materials,” *Nat. Photonics*, vol. 2, no. 4, pp. 219–225, Apr. 2008, doi: 10.1038/nphoton.2008.47.

[75] S. M. Eaton *et al.*, “Heat accumulation effects in femtosecond laser-written waveguides with variable repetition rate,” *Opt. Express*, vol. 13, no. 12, p. 4708, 2005, doi: 10.1364/opex.13.004708.

[76] T. Bauer *et al.*, “Development of an industrial femtosecondlaser micro-machining System.”

[77] V. R. Bhardwaj *et al.*, “Optically produced arrays of planar nanostructures inside fused silica,” *Phys. Rev. Lett.*, vol. 96, no. 5, pp. 1–4, 2006, doi: 10.1103/PhysRevLett.96.057404.

[78] Y. Bellouard and M.-O. Hongler, “Femtosecond-laser generation of self-organized bubble patterns in fused silica,” *Opt. Express*, vol. 19, no. 7, p. 6807, 2011, doi: 10.1364/oe.19.006807.

[79] S. Richter, S. Döring, A. Tünnermann, and S. Nolte, “Bonding of glass with femtosecond laser pulses at high repetition rates,” *Appl. Phys. A Mater. Sci. Process.*, vol. 103, no. 2, pp. 257–261, 2011, doi: 10.1007/s00339-011-6369-1.

[80] E. Toratani, M. Kamata, and M. Obara, “Self-fabrication of void array in fused silica by femtosecond laser processing,” *Appl. Phys. Lett.*, vol. 87, no. 17, pp. 1–3, 2005, doi: 10.1063/1.2115097.

[81] S. zhen Xu *et al.*, “Scan speed and fluence effects in femtosecond laser induced micro/nano-structures on the surface of fused silica,” *J. Non. Cryst. Solids*, vol.

492, pp. 56–62, Jul. 2018, doi: 10.1016/j.jnoncrysol.2018.04.018.

[82] A. M. Streltsov and N. F. Borrelli, “Study of femtosecond-laser-written waveguides in glasses,” *J. Opt. Soc. Am. B*, vol. 19, no. 10, p. 2496, 2002, doi: 10.1364/josab.19.002496.

[83] B. Poumellec, L. Sudrie, M. Franco, B. Prade, and A. Mysyrowicz, “Femtosecond laser irradiation stress induced in pure silica,” *Opt. Express*, vol. 11, no. 9, p. 1070, 2003, doi: 10.1364/oe.11.001070.

[84] P. Vlugter, E. Block, and Y. Bellouard, “Local tuning of fused silica thermal expansion coefficient using femtosecond laser,” *Phys. Rev. Mater.*, vol. 3, no. 5, pp. 1–8, 2019, doi: 10.1103/PhysRevMaterials.3.053802.

[85] Y. Bellouard, T. Colomb, C. Depeursinge, M. Dugan, A. A. Said, and P. Bado, “Nanoindentation and birefringence measurements on fused silica specimen exposed to low-energy femtosecond pulses,” *Opt. Express*, vol. 14, no. 18, pp. 8360–8366, 2006, doi: 10.1364/oe.14.008360.

[86] P. Vlugter and Y. Bellouard, “Elastic properties of self-organized nanogratings produced by femtosecond laser exposure of fused silica,” *Phys. Rev. Mater.*, vol. 4, no. 2, p. 023607, 2020, doi: 10.1103/PhysRevMaterials.4.023607.

[87] C. E. Athanasiou and Y. Bellouard, “A monolithic micro-tensile tester for investigating silicon dioxide polymorph micromechanics, fabricated and operated using a femtosecond laser,” *Micromachines*, vol. 6, no. 9, pp. 1365–1386, 2015, doi: 10.3390/mi6091365.

[88] J. W. Chan, T. Huser, S. Risbud, and D. M. Krol, “Structural changes in fused silica after exposure to focused femtosecond laser pulses,” *Opt. Lett.*, vol. 26, no. 21, pp. 1726–1728, 2001, doi: 10.1364/ol.26.001726.

[89] Y. Bellouard *et al.*, “Stress-state manipulation in fused silica via femtosecond laser irradiation,” *Optica*, vol. 3, no. 12, p. 1285, 2016, doi: 10.1364/optica.3.001285.

[90] M. Malinauskas *et al.*, “Ultrafast laser processing of materials: From science to industry,” *Light Sci. Appl.*, vol. 5, no. 8, pp. 3–5, 2016, doi: 10.1038/lsa.2016.133.

[91] J. Qi *et al.*, “Femtosecond laser induced selective etching in fused silica: optimization of the inscription conditions with a high-repetition-rate laser source,” *Opt. Express*, vol. 26, no. 23, pp. 29669–29678, 2018, doi: 10.1364/oe.26.029669.

[92] C. Hnatovsky, R. S. Taylor, E. Simova, V. R. Bhardwaj, D. M. Rayner, and P. B. Corkum, “Polarization-selective etching in femtosecond laser-assisted microfluidic channel fabrication in fused silica,” *Opt. Lett.*, vol. 30, no. 14, p. 1867, 2005, doi: 10.1364/ol.30.001867.

[93] A. Marcinkevičius *et al.*, “Femtosecond laser-assisted three-dimensional microfabrication in silica,” *Opt. Lett.*, vol. 26, no. 5, p. 277, Aug. 2001, doi: 10.1364/ol.26.000277.

[94] C. G. K. Malek, “Laser processing for bio-microfluidics applications (part II),” *Anal. Bioanal. Chem.*, vol. 385, no. 8, pp. 1362–1369, 2006, doi: 10.1007/s00216-006-0517-z.

[95] V. Tielen and Y. Bellouard, “Three-dimensional glass monolithic micro-flexure fabricated by femtosecond laser exposure and chemical etching,” *Micromachines*, vol. 5, no. 3, pp. 697–710, 2014, doi: 10.3390/mi5030697.

[96] T. Yang and Y. Bellouard, “Monolithic transparent 3D dielectrophoretic micro-actuator fabricated by femtosecond laser,” *J. Micromechanics Microengineering*, vol. 25, no. 10, 2015, doi: 10.1088/0960-1317/25/10/105009.

[97] J. Song *et al.*, “Formation mechanism of self-organized voids in dielectrics induced by tightly focused femtosecond laser pulses,” *Appl. Phys. Lett.*, vol. 92, no. 9, pp. 1–4, 2008, doi: 10.1063/1.2841066.

[98] “Prime Faraday Technology Watch An Introduction to MEMS (Micro-electromechanical Systems),” 2002. [Online]. Available: http://www.amazon.co.uk/exec/obidos/ASIN/1844020207.

[99] D. Enke, F. Janowski, and W. Schwieger, “Porous glasses in the 21st century-a short review,” *Microporous Mesoporous Mater.*, vol. 60, no. 1–3, pp. 19–30, Jun. 2003, doi: 10.1016/S1387-1811(03)00329-9.

[100] H. P. Hood and M. E. Nordberg, “TREATED BOROSILICATE GLASS,” 2106744, 1938.

[101] V. P. Veiko *et al.*, “Direct laser writing of barriers with controllable permeability in porous glass,” *Opt. Express*, vol. 26, no. 21, p. 28150, 2018, doi: 10.1364/oe.26.028150.

[102] J. Matsuoka, M. Toyoda, and S. Yoshida, “Composition dependence of the optical absorption spectra of cupric ion in sodium borosilicate glass melts,” *J. Non. Cryst. Solids*, vol. 354, no. 2–9, pp. 255–258, 2008, doi: 10.1016/j.jnoncrysol.2007.08.081.

[103] R. GARDON, “A Review of Radiant Heat Transfer in Glass,” *J. Am. Ceram. Soc.*, vol. 44, no. 7, pp. 305–312, Jul. 1961, doi: 10.1111/j.1151-2916.1961.tb15914.x.

[104] W. HALLER, D. H. BLACKBURN, F. E. WAGSTAFF, and R. J. CHARLES, “Metastable Immiscibility Surface in the System Na2O-B2O3-SiO2,” *J. Am. Ceram. Soc.*, vol. 53, no. 1, pp. 34–39, Jun. 1970, doi: 10.1111/j.1151-

2916.1970.tb11995.x.
[105] M. Suzuki and T. Tanaka, “Materials design for the fabrication of porous glass using phase separation in multi-component borosilicate glass,” *ISIJ Int.*, vol. 48, no. 11, pp. 1524–1532, 2008, doi: 10.2355/isijinternational.48.1524.
[106] R. Kado *et al.*, “Structural significance of nickel sites in aluminosilicate glasses,” *J. Non. Cryst. Solids*, vol. 539, no. December 2019, p. 120070, 2020, doi: 10.1016/j.jnoncrysol.2020.120070.
[107] F. Farges, G. E. Brown, P. E. Petit, and M. Munoz, “Transition elements in water-bearing silicate glasses/melts. Part I. A high-resolution and ancharmonic analysis of Ni coordination environments in crystals,glasses,and melts,” *Geochim. Cosmochim. Acta*, vol. 65, no. 10, pp. 1665–1678, 2001, doi: 10.1016/S0016-7037(00)00625-6.
[108] L. Cormier, L. Galoisy, and G. Calas, “Evidence of Ni-containing ordered domains in low-alkali borate glasses,” *Europhys. Lett.*, vol. 45, no. 5, pp. 572–578, 1999, doi: 10.1209/epl/i1999-00205-7.
[109] Q. Xu, T. Maekawa, K. Kawamura, and T. Yokokawa, “Local structure around Ni2+ ions in sodium borate glasses,” *Phys. Chem. Glas.*, vol. 31, no. 4, pp. 151–155, 1990.
[110] K. Tomita, T. Kishi, D. Matsumura, and T. Yano, “Laser heating induced spatial homogenization of phase separated Na2O-B2O3-SiO2 glass plate with bearing NiO for heat center and structural probe,” *J. Non. Cryst. Solids*, vol. 597, no. December, p. 121891, 2022, doi: 10.1016/j.jnoncrysol.2022.121891.
[111] H. Shigemura, M. Shojiya, R. Kanno, Y. Kawamoto, K. Kadono, and M. Takahashi, “Optical property and local environment of Ni2+ in fluoride glasses,” *J. Phys. Chem. B*, vol. 102, no. 11, pp. 1920–1925, 1998, doi: 10.1021/jp973311d.
[112] A. Terczyńska-Madej, K. Cholewa-Kowalska, and M. Łączka, “Coordination and valence state of transition metal ions in alkali-borate glasses,” *Opt. Mater. (Amst).*, vol. 33, no. 12, pp. 1984–1988, 2011, doi: 10.1016/j.optmat.2011.03.046.
[113] J. A. Duffy, “Optical basicity: A practical acid-base theory for oxides and oxyanions,” *J. Chem. Educ.*, vol. 73, no. 12, pp. 1138–1142, 1996, doi: 10.1021/ed073p1138.
[114] L. Galoisy and G. Calas, “XANES and crystal field spectroscopy of five-coordinated Nickel(II) in potassium-nickel phosphate,” *Mater. Res. Bull.*, vol. 28, no. 3, pp. 221–228, 1993, doi: 10.1016/0025-5408(93)90155-7.
[115] M. Ciampolini, “A Crystal Field Model for High-Spin Five-Coordinated Nickel(II) Complexes,” *Inorg. Chem.*, vol. 5, no. 1, pp. 35–40, 1966, doi:

10.1021/ic50035a009.

[116] L. Galoisy, G. Calas, L. Cormier, B. Marcq, and M. H. Thibault, “Overview of the environment of Ni in oxide glasses in relation to the glass colouration,” *Phys. Chem. Glas.*, vol. 46, no. 4, pp. 394–399, 2005.

[117] A. A. Abul-Magd, H. Y. Morshidy, and A. M. Abdel-Ghany, “The role of NiO on the structural and optical properties of sodium zinc borate glasses,” *Opt. Mater. (Amst).*, vol. 109, no. August, p. 110301, 2020, doi: 10.1016/j.optmat.2020.110301.

[118] A. B. P. Lever, “Electronic spectra of some transition metal complexes: Derivation of Dq and B,” *J. Chem. Educ.*, vol. 45, no. 11, pp. 711–712, 1968, doi: 10.1021/ed045p711.

[119] F. Farges and G. E. Brown, “An empirical model for the anharmonic analysis of high-temperature XAFS spectra of oxide compounds with applications to the coordination environment of Ni in NiO, γ-Ni2SiO4 and Ni-bearing Na-disilicate glass and melt,” *Chem. Geol.*, vol. 128, no. 1–4, pp. 93–106, 1996, doi: 10.1016/0009-2541(95)00165-4.

[120] L. Galoisy and G. Calas, “Structural environment of nickel in silicate glass/melt systems: Part 1. Spectroscopic determination of coordination states,” *Geochim. Cosmochim. Acta*, vol. 57, no. 15, pp. 3613–3626, 1993, doi: 10.1016/0016-7037(93)90143-K.

[121] V. A. Kreisberg and T. V. Antropova, “Changing the relation between micro- and mesoporosity in porous glasses: The effect of different factors,” *Microporous Mesoporous Mater.*, vol. 190, pp. 128–138, 2014, doi: 10.1016/j.micromeso.2014.02.002.

[122] W. Vogel, “Phase separation in glass,” *J. Non. Cryst. Solids*, vol. 25, no. 1–3, pp. 170–214, Sep. 1977, doi: 10.1016/0022-3093(77)90093-X.

[123] A. Yasumori, F. Tada, S. Yanagida, and T. Kishi, “Yellow Photoluminescence Properties of Copper Ion Doped Phase–Separated Glasses in Alkali Borosilicate System,” *J. Electrochem. Soc.*, vol. 159, no. 5, pp. J143–J147, 2012, doi: 10.1149/2.001205jes.

[124] D. Möncke and D. Ehrt, “Influence of melting and annealing conditions on the optical spectra of a borosilicate glass doped with CoO and NiO,” *Glas. Sci. Technol. Glas. Berichte*, vol. 75, no. 4, pp. 163–173, 2002.

[125] H. Keppler and N. Bagdassarov, “The speciation of Ni and Co in silicate melts from optical absorption spectra to 1500°C,” *Chem. Geol.*, vol. 158, no. 1–2, pp. 105–115, 1999, doi: 10.1016/S0009-2541(99)00021-2.

[126] W. H. TURNER and J. A. TURNER, “Ligand-Field Spectra and Structure of Nickel in Silicate Glasses,” *J. Am. Ceram. Soc.*, vol. 55, no. 4, pp. 201–207, 1972, doi: 10.1111/j.1151-2916.1972.tb11259.x.

[127] D. Möncke, D. Ehrt, H. Eckert, and V. Mertens, “Erratum: Influence of melting and annealing conditions on the structure of borosilicate glasses (Physics and Chemistry of Glasses (2003) 44, 2 (113-116)),” *Phys. Chem. Glas.*, vol. 44, no. 6, p. 454, 2003.

[128] O. V. Mazurin and M. V. Streltsina, “Determination of tie-line directions in the metastable phase-separation regions of ternary systems,” *J. Non. Cryst. Solids*, vol. 11, no. 3, pp. 199–218, 1972, doi: 10.1016/0022-3093(72)90003-8.

[129] Rikuo OTA and S. Naohiro, “Variation of the System Regions Rate in the B2O3-Li2O with Cooling,” *Yogyo-Kyokai Shi*, vol. 92, no. 1, pp. 10–14, 1984.

[130] J. A. Duffy, “A review of optical basicity and its applications to oxidic systems,” *Geochim. Cosmochim. Acta*, vol. 57, no. 16, pp. 3961–3970, 1993, doi: 10.1016/0016-7037(93)90346-X.

[131] J. A. Duffy and M. D. Ingram, “An interpretation of glass chemistry in terms of the optical basicity concept,” *J. Non. Cryst. Solids*, vol. 21, no. 3, pp. 373–410, 1976, doi: 10.1016/0022-3093(76)90027-2.

[132] J. A. Duffy, M. D. Ingram, and S. Fong, “Effect of basicity on chemical bonding of metal ions in glass and its relevance to their stability,” *Phys. Chem. Chem. Phys.*, vol. 2, no. 8, pp. 1829–1833, 2000, doi: 10.1039/b000489h.

[133] P. S. Fiske and J. F. Stebbins, “The structural role of Mg in silicate liquids: a high-temperature 25Mg, 23Na, and 29Si NMR study,” *Am. Mineral.*, vol. 79, no. 9–10, pp. 848–861, 1994.

[134] M. C. Wilding, C. J. Benmore, J. A. Tangeman, and S. Sampath, “Coordination changes in magnesium silicate glasses,” *Europhys. Lett.*, vol. 67, no. 2, pp. 212–218, Jul. 2004, doi: 10.1209/epl/i2003-10286-8.

[135] M. Muñoz *et al.*, “In situ speciation of nickel in hydrous melts exposed to extreme conditions,” *Phys. Scr. T*, vol. T115, pp. 921–922, 2005, doi: 10.1238/Physica.Topical.115a00921.

[136] F. Farges, G. E. Brown, G. Calas, L. Galoisy, and G. A. Waychunas, “Coordination change around 2 wt% Ni in Na2Si2O5 glass/melt systems,” *Phys. B Phys. Condens. Matter*, vol. 208–209, no. C, pp. 381–382, 1995, doi: 10.1016/0921-4526(94)00704-Y.

[137] N. Van Hung, R. Frahm, and H. Kamitsubo, “Anharmonic Contributions to High-Temperature EXAFS Spectra: Theory and Comparison with Experiment,” *J.*

Phys. Soc. Japan, vol. 65, no. 11, pp. 3571–3575, 1996, doi: 10.1143/jpsj.65.3571.

[138] L. Galoisy and G. Calas, “Role of alkali field strength on the speciation of Ni2+ in alkali borate glasses: comparison with crystalline Ni-borates,” *J. Non. Cryst. Solids*, vol. 577, no. December 2021, p. 121320, 2022, doi: 10.1016/j.jnoncrysol.2021.121320.

[139] L. Galoisy and G. Calas, “Structural environment of nickel in silicate glass/melt systems: Part 2. Geochemical implications,” *Geochim. Cosmochim. Acta*, vol. 57, no. 15, pp. 3627–3633, 1993.

[140] Y. Tian *et al.*, “Speciation of nickel (II) chloride complexes in hydrothermal fluids: In situ XAS study,” *Chem. Geol.*, vol. 334, pp. 345–363, 2012, doi: 10.1016/j.chemgeo.2012.10.010.

[141] P. TAYLOR, S. ASHMORE, and A. CAMPBELL, “Liquid immiscibility in the systems X20-MO-B203-Si02 (X=Na, K; M=Mg, Ca, Ba) and Na20-MgO-BaO-B203-Si02,” *J. Am. Ceram. Soc.*, vol. 67, no. 9, pp. 347–351, 1984.

[142] P. TAYLOR, A. B. CAMPBELL, and D. G. OWEN, “Liquid Immiscibility in the Systems X2O-MO-B2O3-SiO2 (X=Na, K; M=Mg, Ca, Ba) and Na2O-MgO-BaO-B2O3-SiO2,” *J. Am. Ceram. Soc.*, vol. 66, no. 5, pp. 347–351, May 1983, doi: 10.1111/j.1151-2916.1983.tb10046.x.

[143] P. Hrma and J. Marcial, “Dissolution retardation of solid silica during glass-batch melting,” *J. Non. Cryst. Solids*, vol. 357, no. 15, pp. 2954–2959, 2011, doi: 10.1016/j.jnoncrysol.2011.03.041.

[144] “Heat Transfer Module,” 2015. [Online]. Available: https://doc.comsol.com/5.4/doc/com.comsol.help.heat/HeatTransferModuleUsersGuide.pdf.

[145] L. Guo, S. Geng, X. Gao, and W. Wang, “Numerical simulation of heat transfer and fluid flow during nanosecond pulsed laser processing of Fe78Si9B13 amorphous alloys,” *Int. J. Heat Mass Transf.*, vol. 170, p. 121003, 2021, doi: 10.1016/j.ijheatmasstransfer.2021.121003.

[146] Y. B. Safdari, “Radiation Heating Through Transparent and Opaque Walls,” pp. 53–58, 1966.

[147] D. L. Pye, A. Monternrto, and I. Joseph, *Properties of Glass-Forming Melts*. CRC Press, 2005.

[148] P. Crnjac, L. Škerget, J. Ravnik, and M. Hriberšek, “Implementation of the Rosseland and the P1 radiation models in the system of Navier-Stokes equations with the boundary element method,” *Int. J. Comput. Methods Exp. Meas.*, vol. 5,

no. 3, pp. 348–358, 2017, doi: 10.2495/CMEM-V5-N3-348-358.

[149] P. Richet, M. Ali Bouhifd, P. Courtial, and C. Téqui, “Configurational heat capacity and entropy of borosilicate melts,” *Journal of Non-Crystalline Solids*, vol. 211, no. 3. Journal of non-crystalline solids, pp. 271–280, 1997, doi: 10.1016/S0022-3093(96)00646-1.

[150] O. V. Mazurin, M. V. Streltsina, and T. P. Shvaiko-Shvaikovskaya, *Handbook of Glass Data: Ternary Silicate Glasses Pt. C (Physical Sciences Data)*. Elsevier Science Ltd, 1987.

[151] A. Faber, M. Rongen, A. Lankhorst, and D. D. S. Meneses, “Characterization of high temperature optical spectra of glass melts and modeling of thermal radiation conductivity,” *Int. J. Appl. Glas. Sci.*, vol. 11, no. 3, pp. 442–462, Jul. 2020, doi: 10.1111/ijag.15111.

[152] M. Lenoir, A. Grandjean, Y. Linard, B. Cochain, and D. R. Neuville, “The influence of Si,B substitution and of the nature of network-modifying cations on the properties and structure of borosilicate glasses and melts,” *Chem. Geol.*, vol. 256, no. 3–4, pp. 316–325, 2008, doi: 10.1016/j.chemgeo.2008.07.002.

[153] M. M. Smedskjaer, J. C. Mauro, R. E. Youngman, C. L. Hogue, M. Potuzak, and Y. Yue, “Topological Principles of Borosilicate Glass Chemistry,” *J. Phys. Chem. B*, vol. 115, no. 44, pp. 12930–12946, Nov. 2011, doi: 10.1021/jp208796b.

[154] S. P. Jaccani and L. Huang, “Understanding Sodium Borate Glasses and Melts from Their Elastic Response to Temperature,” *Int. J. Appl. Glas. Sci.*, vol. 7, no. 4, pp. 452–463, 2016, doi: 10.1111/ijag.12250.

[155] R. L. HERVIG and A. NAVROTSKY, “Thermochemistry of Sodium Borosilicate Glasses,” *J. Am. Ceram. Soc.*, vol. 68, no. 6, pp. 314–319, 1985, doi: 10.1111/j.1151-2916.1985.tb15232.x.

[156] H. Toshiyoshi, S. Ju, H. Honma, C. H. Ji, and H. Fujita, “MEMS vibrational energy harvesters,” *Sci. Technol. Adv. Mater.*, vol. 20, no. 1, pp. 124–143, 2019, doi: 10.1080/14686996.2019.1569828.

[157] M. A. Mironov, “Propagation of a flexural wave in a plate whose thickness decreases smoothly to zero in a finite interval,” *Sov. Phys. Acoust.*, vol. 34, no. 3, pp. 318–319, 1988, doi: 10.1007/978-1-4419-0217-7_1.

[158] V. V. Krylov and F. J. B. S. Tilman, “Acoustic ‘black holes’ for flexural waves as effective vibration dampers,” *J. Sound Vib.*, vol. 274, no. 3–5, pp. 605–619, Jul. 2004, doi: 10.1016/j.jsv.2003.05.010.

[159] V. Krylov, “Conditions for validity of the geometrical-acoustics approximation in application to waves in an acute-angle solid wedge,” *Sov. Phys. - Acoust.*, vol. 35,

no. 2, pp. 176–180, 1989, [Online]. Available: http://journals.aip.org/.

[160] V. V. Krylov and R. E. T. B. Winward, “Experimental investigation of the acoustic black hole effect for flexural waves in tapered plates,” *J. Sound Vib.*, vol. 300, no. 1–2, pp. 43–49, Feb. 2007, doi: 10.1016/j.jsv.2006.07.035.

[161] V. Krylov, “Acoustic black holes: Recent developments in the theory and applications,” *IEEE Trans. Ultrason. Ferroelectr. Freq. Control*, vol. 61, no. 8, pp. 1296–1306, 2014, doi: 10.1109/TUFFC.2014.3036.

[162] T. Yang and Y. Bellouard, “3D electrostatic actuator fabricated by non-ablative femtosecond laser exposure and chemical etching,” *MATEC Web Conf.*, vol. 32, no. 0, pp. 1–6, 2015, doi: 10.1051/matecconf/20153202004.

[163] K. Hirao and K. Miura, “Section 2. Photo-induced and non-linear optical effects in glasses: Writing waveguides and gratings in silica and related materials by a femtosecond laser,” *J. Non. Cryst. Solids*, vol. 239, no. 1–3, pp. 91–95, 1998.

[164] R. S. Taylor, C. Hnatovsky, E. Simova, D. M. Rayner, V. R. Bhardwaj, and P. B. Corkum, “Ultra-high resolution index of refraction profiles of femtosecond laser modified silica structures,” in *OSA Trends in Optics and Photonics Series*, 2003, vol. 88, no. 7, pp. 775–781, doi: 10.1364/oe.11.000775.

[165] P. A. Feurtado, S. C. Conlon, and F. Semperlotti, “A normalized wave number variation parameter for acoustic black hole design,” *J. Acoust. Soc. Am.*, vol. 136, no. 2, pp. EL148–EL152, Jul. 2014, doi: 10.1121/1.4890205.

[166] S. Rajesh and Y. Bellouard, “Towards fast femtosecond laser micromachining of glass, effect of deposited energy,” *Opt. InfoBase Conf. Pap.*, vol. 18, no. 20, pp. 11560–11566, 2010, doi: 10.1364/cleo.2010.jtud18.

[167] K. M. Davis and M. Tomozawa, “Water diffusion into silica glass: Structural changes in silica glass and their effect on water solubility and diffusivity,” *J. Non. Cryst. Solids*, vol. 185, no. 3, pp. 203–220, 1995, doi: 10.1016/0022-3093(95)00015-1.

[168] A. Sarikov *et al.*, “Characteristics of hydrogen effusion from the Si-H bonds in Si rich silicon oxynitride films for nanocrystalline silicon based photovoltaic applications,” *Adv. Mater. Res.*, vol. 854, no. January, pp. 69–74, 2014, doi: 10.4028/www.scientific.net/AMR.854.69.

[169] A. Zoubir *et al.*, “Laser-induced defects in fused silica by femtosecond IR irradiation,” *Phys. Rev. B - Condens. Matter Mater. Phys.*, vol. 73, no. 22, pp. 1–5, 2006, doi: 10.1103/PhysRevB.73.224117.

[170] V. Dřínek, K. Vacek, G. Yuzhakov, Z. Bastl, and S. Naumov, “Hydrogen related point defects in silicon based layers: Si(•)H and SiOOH,” *Surf. Sci.*, vol. 600, no.

7, pp. 1462–1467, 2006, doi: 10.1016/j.susc.2006.01.039.

[171] W. J. Reichman *et al.*, “A spectroscopic comparison of femtosecond-laser-modified fused silica using kilohertz and megahertz laser systems,” *J. Appl. Phys.*, vol. 99, no. 12, 2006, doi: 10.1063/1.2207556.

[172] R. A. B. Devine, “Ion implantation- and radiation-induced structural modifications in amorphous SiO2,” *J. Non. Cryst. Solids*, vol. 152, no. 1, pp. 50–58, 1993, doi: 10.1016/0022-3093(93)90443-2.

[173] J. E. Shelby, “Density of vitreous silica,” *J. Non. Cryst. Solids*, vol. 349, no. 1–3, pp. 331–336, 2004, doi: 10.1016/j.jnoncrysol.2004.08.206.

[174] R. Le Parc, C. Levelut, J. Pelous, V. Martinez, and B. Champagnon, “Influence of fictive temperature and composition of silica glass on anomalous elastic behaviour,” *J. Phys. Condens. Matter*, vol. 18, pp. 7507–7527, 2006, doi: 10.1088/0953-8984/21/7/079802.

[175] C. Hnatovsky *et al.*, “Fabrication of microchannels in glass using focused femtosecond laser radiation and selective chemical etching,” *Appl. Phys. A Mater. Sci. Process.*, vol. 84, no. 1–2, pp. 47–61, 2006, doi: 10.1007/s00339-006-3590-4.

[176] D. Tan, K. N. Sharafudeen, Y. Yue, and J. Qiu, “Femtosecond laser induced phenomena in transparent solid materials: Fundamentals and applications,” *Prog. Mater. Sci.*, vol. 76, no. September 2015, pp. 154–228, 2016, doi: 10.1016/j.pmatsci.2015.09.002.

[177] P. S. Salter and M. J. Booth, “Adaptive optics in laser processing,” *Light Sci. Appl.*, vol. 8, no. 1, pp. 1–16, 2019, doi: 10.1038/s41377-019-0215-1.

[178] S. Sen, Z. Xu, and J. F. Stebbins, “Temperature dependent structural changes in borate, borosilicate and boroaluminate liquids: High-resolution 11B, 29Si and 27Al NMR studies,” *J. Non. Cryst. Solids*, vol. 226, no. 1–2, pp. 29–40, 1998, doi: 10.1016/S0022-3093(97)00491-2.

[179] C. T. MOYNIHAN, A. J. EASTEAL, M. A. De BOLT, and J. TUCKER, “Dependence of the Fictive Temperature of Glass on Cooling Rate,” *J. Am. Ceram. Soc.*, vol. 59, no. 1–2, pp. 12–16, 1976, doi: 10.1111/j.1151-2916.1976.tb09376.x.

Acknowledgements

I would like to express my sincere gratitude to my supervisor Dr. T. Yano, Professor and Dr. T. Kishi, Professor. Under their supervision including kind support and grateful education, I could further enhance my insight into glass science and enjoy every opportunity of various experiments.

My appreciation goes to many supports from SPring-8 organized by JASRI. Dr. D. Matsumura had given me essential help on XAFS measurement and analysis from basis. Dr. K. Osaka helped me a lot in preparation for in-situ SAXS measurement which required a lot of care for successful measurement.

I would also like to thank Professor N. Matsushita, Dr. Y. Kubota, and Dr. R. Nitta from Tokyo Institute of Technology for their kind help in my study and research. I would also give great appreciation to Dr. M Susa, Professor, Dr. M. Hayashi, Professor, and H. Hidai, Professor for giving critical and essential advice on this thesis, which was necessary to have more perspectives from various point of view.

I express my heartful thanks to Professor Y. Bellouard and Dr. P. Vlugter for providing me great chance to study in EPFL, broadening my horizons in different research field and offered further consideration on my research career.

I would like to thank the laboratory members for the help in experiments and daily life. I am lucky to meet these nice members who helped me a lot in carrying out my research. Great appreciation goes to Mr. E. Mouri for constructing experimental set up used in high temperature in-situ measurement. And I would like to also show my appreciation to my families and friends for their great helps and supports in study and life. I would like to thank Mr. Y. Fujiwara for a lot of support both on my life and data analysis.

The XAFS measurements in this work was performed under the Shared Use Program of JAEA Facilities (Proposal No. 2019B-E03) with the approval of Nanotechnology Platform project supported by the Ministry of Education, Culture, Sports, Science and Technology (Proposal No. A-19-AE-0023). The synchrotron radiation experiments were performed at JAEA beamline BL14B1 in SPring-8 (Proposal No.2019B3645) and BL14B2 (Proposal No.2021B1903) for XAFS and BL19B2 (Proposal No.2021B1963, 2022A1788) for SAXS measurement.